Asia Pacific Research Initiative for Sustainable Energy Systems 2015 (APRISES15)

Office of Naval Research
Grant Award Number N00014-16-1-2116

Ocean Thermal Energy Conversion (OTEC) Heat Exchanger Development

(August 2018 - January 2020)

Task 6.1

Prepared for
Hawaiʻi Natural Energy Institute

Prepared by
Makai Ocean Engineering

May 2020

HNEI
Hawaiʻi Natural Energy Institute
University of Hawaiʻi at Mānoa

MAKAI OCEAN ENGINEERING

ANNUAL REPORT

Prepared For

HAWAII NATURAL ENERGY INSTITUTE

RICK ROCHELEAU

1680 East West Road, POST 109

Honolulu, HI, 96822

USA

Prepared By

MAKAI OCEAN ENGINEERING

PO Box 1206, Kailua, Hawaii 96734

May 2020

TABLE OF CONTENTS

LIST OF FIGURES

LIST OF TABLES

1. INTRODUCTION

Makai Ocean Engineering has been developing Thin Foil Heat Exchangers (TFHX) for use in seawater-refrigerant, air-water, and water-water applications. This report summarizes work performed between August 2018 – January 2020.

In this period, Makai made two iterations to the TFHX design, from TFHX-3B to TFHX-3C to TFHX-3E. With each iteration, the materials cost was reduced by half (from $1450/m^2 to $660/m^2 to $330/m^2) whereas the labor and overhead cost has remained roughly constant. In terms of commercialization of the TFHX, Makai's next step is to reduce the labor and overhead costs. Makai is developing a design for a High Speed Welding Station (HSWS) which is projected to enable a 5X reduction in labor and overhead cost (by speeding up the fabrication process).

Makai has continued to conduct performance testing of the TFHXs. Makai expanded testing fluids to include air in the external channels and installed air-water testing apparatuses. Seawater-ammonia and seawater-seawater performance testing was also conducted at the 100 kW Test Station.

Makai also installed the first commercial TFHX unit at Cyanotech. The TFHX was able to maintain the Cyanotech pond temperature below the maximum threshold temperature and use less cold seawater to do so (compared to Cyanotech's existing system). At the same flow rate, the TFHX had a 3.75°C approach temperature compared to 10°C for the existing Cyanotech system. After a 3-month test period, Makai discontinued monitoring and data collection but the TFHX unit remains installed and functional at Cyanotech.

In addition to producing plates for performance testing, Makai has also fabricated over 300 plates for characterization studies. For a specified plate design, characterization studies have focused on 1) determining the effective internal channel spacing, 2) determining the pressure rating (supported and unsupported burst pressures), 3) establishing a fatigue life (cycles to failure), and 4) determining the hydraulic performance for different fluids. Each test requires multiple samples of the same plate for statistical analysis and demonstration of repeatability. Particularly for the fatigue tests, the variation in results has been large; Makai has been re-examining the fabrication process and test methods to ensure no unintentional biases are introduced. The variation in effective internal channel spacing within a plate is ~ 5% and based on our characterization, the internal effective spacing can be predicted within 0.1 mm for a specified design. The supported burst and unsupported burst pressures are more variable and our testing has indicated the overall shape of the plate, not just the plate design, affects the pressure rating.

Finally, Makai concluded the aluminum corrosion testing program. Box coupons were tested for over 10 years in warm and cold seawater. The 10-year samples reinforced Makai's previous conclusion; aluminum alloy performance in seawater is unpredictable.

2. TFHX DEVELOPMENT

Makai has continued to make design changes to improve TFHX performance, reduce fabrication time and complexity, and reduce material cost. In the period covered by this report, Makai focused on manifold design, weld design, and design of fabrication equipment.

TFHX manifold design affects performance, fabrication, and cost. Manifolds serve two purposes: 1) direct fluid to the internal passages of each TFHX plate, and 2) comprise part of the sealing components used to separate the internal fluid from the external fluid. In the current (and previous) design iteration, o-rings are used to separate the internal from the external fluid; the manifold provides support for o-ring compression. The combined thickness of the foil and manifold components dictate TFHX plate spacing, which determines how tightly the plates can be spaced (volumetric density) and performance (the size of the internal and external channels affects pressure drop and convective coefficients). Manifold components also contribute to the overall fabrication time and cost of the TFHX plate.

The TFHX was designed with the intent for each step of the fabrication process to be readily transferrable to a high-speed, high-volume manufacturing environment. Makai is one step closer to the high-volume goal with the design of the High Speed Welding Station, which is expected to reduce the current fabrication time by at least 5X.

In conjunction with design changes, Makai has been compiling a comprehensive database of empirical measurements to characterize the TFHX's geometric, mechanical, and thermal-hydraulic properties; these data are intended to be incorporated in a design tool used to drive TFHX design decisions for future applications and provide foundational data for expected operational limits and service life.

Finally, the TFHX is intended to provide a heat exchanger solution for a wide range of applications. After demonstrating the ability to reliably fabricate individual TFHX plates, the next step is to complete design work for the rest of the heat exchanger. This includes designs for pass-through versus fully enclosed heat exchangers, attention to ducting of internal/external fluids, methods to achieve and maintain precise plate spacing, and methods to reliably stack hundreds (or thousands) of plates.

2.1. TFHX MANIFOLD DEVELOPMENT

In this time period, Makai went through two manifold design iterations, from TFHX-3B to TFHX-3C to TFHX-3E. Cost, fabrication time, and compactness (reducing the plate spacing) were the driving factors for manifold development. In 3B and 3C designs, the manifolds were separate machined titanium pieces that had to be welded to the foil. Details about the 3E manifold are proprietary. The manifold pieces were designed with sufficient thicknesses to contain the o-ring grooves and support the required o-ring compression. Plate spacing was reduced from 3.9 mm in 3B and 3C to 2 mm in 3E.

In 3B and 3C, spacers were used to direct fluid into the plate. 3B used titanium “comb spacers” and 3C used 36 individual tear-drop shaped “pill spacers”. Both had to be welded to the foil.

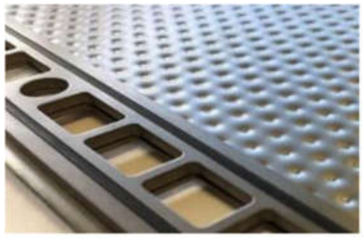

3B, 3.9 mm plate spacing. Long titanium manifolds span the length of the plate (1.2 m) and have machined o-ring grooves.

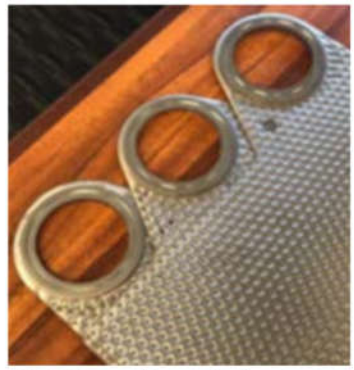

3C, 3.89 mm plate spacing down to 1.39 mm with 3 interlocking plates. Titanium manifold pieces have machined o-ring grooves. “Pill spacers” also welded between foil to provide internal fluid passage.

Figure 1. Comparison of TFHX manifold development.

3B was a 1.2 m long plate with manifolds that spanned the entire length. In 3C, circular manifolds with diameters ~ 1/3 of the plate width were used in order to accommodate up to three interlocking plates. As seen in Figure 1, the manifold can be positioned in three locations, which reduces the plate spacing by one-third, from 3.9 mm to 1.3 mm. However, the position of the manifolds introduced variability in internal flow path between then center manifold plate type and the left/right manifold plate types. In 3E, the plate spacing was reduced to 2 mm and based on lessons learned from 3C, 3E was designed to accommodate two interlocking plates, thereby reducing the plate spacing to 1 mm. The interlocking plates are mirror images and have comparable internal flow paths. For applications in the 1-2 mm plate-spacing range, the 3E platform is a proven platform.

Makai has also been developing designs to eliminate the use of o-rings to separate the internal/external fluids. Eliminating the o-rings enables tighter plate spacings and reduces the risk of leaks due to misalignment when stacking thousands of plates in one heat exchanger. In TFHX-3F, Makai designed features that form a metal seal when stacked and compressed. Although Makai was able to produce a few plate samples, the metal seal was inadequate. The features require re-analysis and re-design.

Makai has also started conceptual designs and research on the requirements and methods needed to create an all-welded heat exchanger, which requires welding along the thickness of two pieces of foil (0.002”-0.005”). An all-welded option minimizes the risk of leaks and misalignments during operation and installation but increases the difficulty of fabrication and maintenance/repair. For example, if a modular approach is used, a defect during fabrication on one plate may require the entire module to be discarded. Similarly, if an installed TFHX is damaged, the entire module would have to be replaced. With a gasketed version, it is likely that only a single plate would require replacement.

2.2. TFHX DESIGN

Three types of welds are used in a TFHX plate, the seal weld, transition weld, and pattern weld. The seal weld sets the perimeter of the internal fluid channel and the overall plate shape. Transition welds are used to transition from non-uniform features, such as the manifold, to the uniform main heat transfer region. Transition welds are not considered part of the heat transfer area, but are important in ensuring evenly distributed flow within the plate and between plates. The pattern weld is used in the main heat transfer area and the design of the pattern weld is driven by the performance requirements. All three weld designs must also meet the heat exchanger operating conditions and specifications (e.g., pressure rating, service life, etc.).

A key advantage of the TFHX is that each individual plate meets the pressure rating without external support. This is accomplished by designing each of the three types of welds to withstand the required pressure; the TFHX will fail at the weakest weld. However, the mechanical strength must also be balanced by thermal and hydraulic performance.

For example, in the TFHX-3C plates, the larger transition welds resulted in smaller passages compared to the main pattern weld and introduced high pressure drops which likely affected heat exchanger performance.

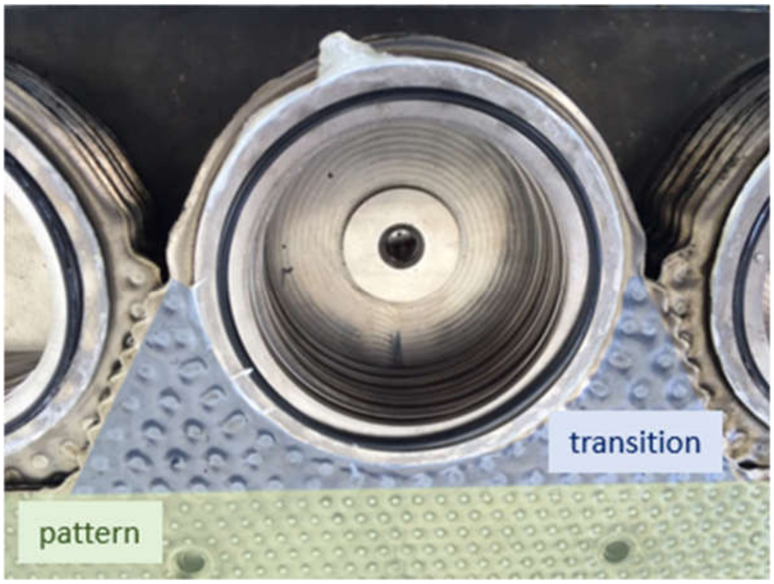

Figure 2. TFHX-3C plate with transition and pattern regions highlighted. The transition weld design unintentionally resulted in smaller passages in the transition region compared to the pattern region, which may have introduced uneven flow distribution in the pattern region.

After 3C testing, an additional requirement was placed on transition weld designs. In addition to meeting the required pressure rating, the transition zone passages had to have a hydraulic diameter larger than the pattern zone region.

2.3. TFHX HEAT EXCHANGER DESIGN

2.3.1. Housing Design

To date, the seawater-ammonia testing has been conducted in the crossflow configuration; i.e., the ammonia flow path is vertical (upwards in the evaporator and downwards in the condenser) and the seawater flow path is horizontal. The plates are installed in a housing and the internal and external fluids are ducted into the housing. For the crossflow configuration, the housing is shaped like a cross.

Seawater-seawater testing has been conducted in a counterflow configuration, in which the internal and external path lengths are vertical, but the inlets are on opposite sides. A four-port design is used to duct the internal and external fluid.

A pass-through design can be used in applications in which the TFHX can be immersed in the external fluid. The pass-through design can be crossflow, counterflow, or parallel flow in configuration and the housing consists mainly of end plates designed to duct the internal fluid and provide compression for the manifold o-rings to seal the internal passages from the external fluid. Makai utilized a pass-thru design for the Cyanotech cooling application described in Section 6.

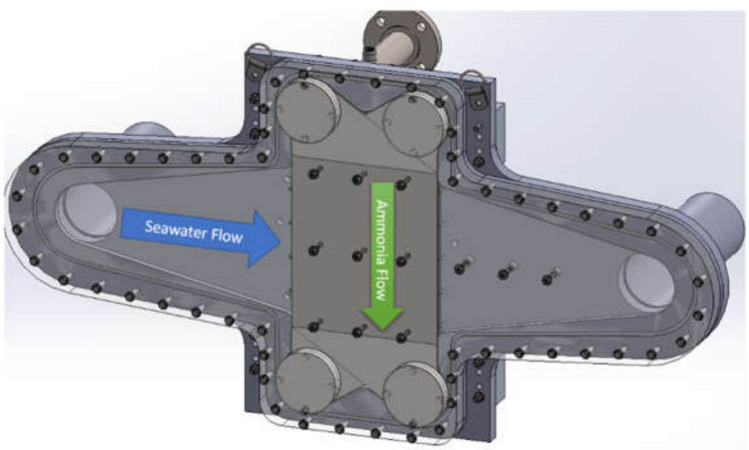

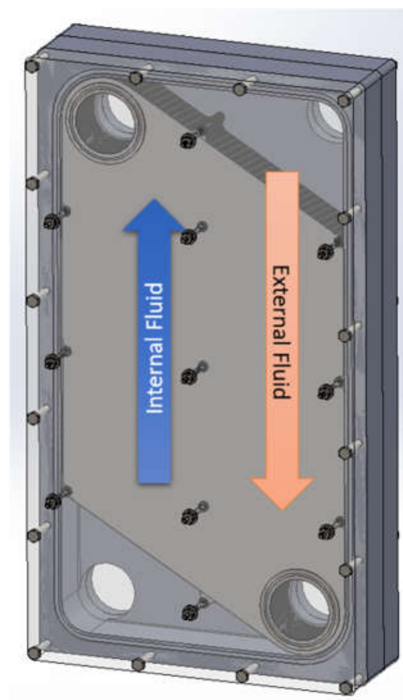

Figure 3. Top: fully enclosed heat exchangers in the crossflow (left) and counterflow (right) configuration. Bottom: Model of pass-through design and pass-through module installed in Cyanotech pond.

2.3.2. External Channel Spacing

Maintaining uniform external channel spacing is another important consideration in maximizing performance. Uneven channel spacing can induce uneven flow distribution and uneven heat transfer between plates.

For seawater-ammonia and seawater-seawater testing, plate spacing was maintained using comb spacers at the inlet and outlet edges of the plates and stacking washers between each plate in a grid of 9-25 locations. The washers were kept in position using threaded rods that went through the plates and housing.

For air-water testing, custom, comb spacers were used to set the plate spacing at the inlet and outlet edges. Plate spacing in air-water testing was unique because it was determined by the number of plates and the width of the air flow duct. This was the most efficient method to test a range of air channel spacings but introduced some curvature in the plates because the test section plate spacing was often smaller than the actual plate spacing; i.e., plates were being "squeezed" into the air duct to test smaller plate spacings than dictated by the foil and manifold thickness.

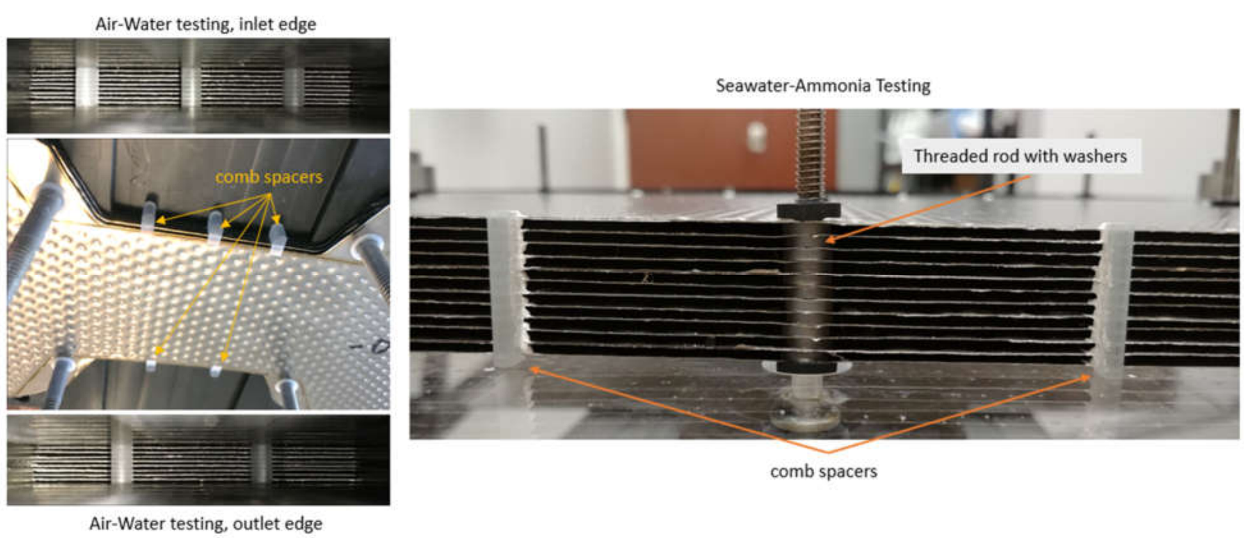

Figure 4. Current methods to maintain plate spacing.

Both solutions for testing were adequate for testing relatively few plates and relatively large external channel sizes (~ 0.5 mm). However, comb spacers become impractical when stacking over 30 plates and are limited to the inlet/outlet edges. For larger plates, the ability to ensure even plate spacing in the middle of the plate is also desirable. The threaded rods and washers introduce additional penetrations into the housing which increases the risk of leaks and have been difficult to align. Some broken washers as well as deformation of the plate near the washers have been observed after testing. Neither solution is ideal for large-scale production and assembly.

Makai has developed a proprietary scalable solution using no additional components to assemble and no components that can become loose or lost during operation (and no longer provide the function of maintaining spacing). Makai will be testing the functionality in the next iteration of air-water testing.

2.3.3. Modular Stacking

The Cyanotech application demonstrated one version of modular TFHX units, connected in series to provide required thermal management. For applications with thousands of plates a modular solution also enables easier handling in terms of weight and size and the ability to inspect individual modules for quality control. Makai has started preliminary design work on modules. Although the stacked unit is similar in appearance to plate-frame heat exchangers, the module components and endplates are significantly lighter since each TFHX plate is individually rated for design pressure, the modules need only to support o-ring compression and the external fluid pressure. Similarly, endplates on the assembled unit need to support o-ring compression to seal between modules.

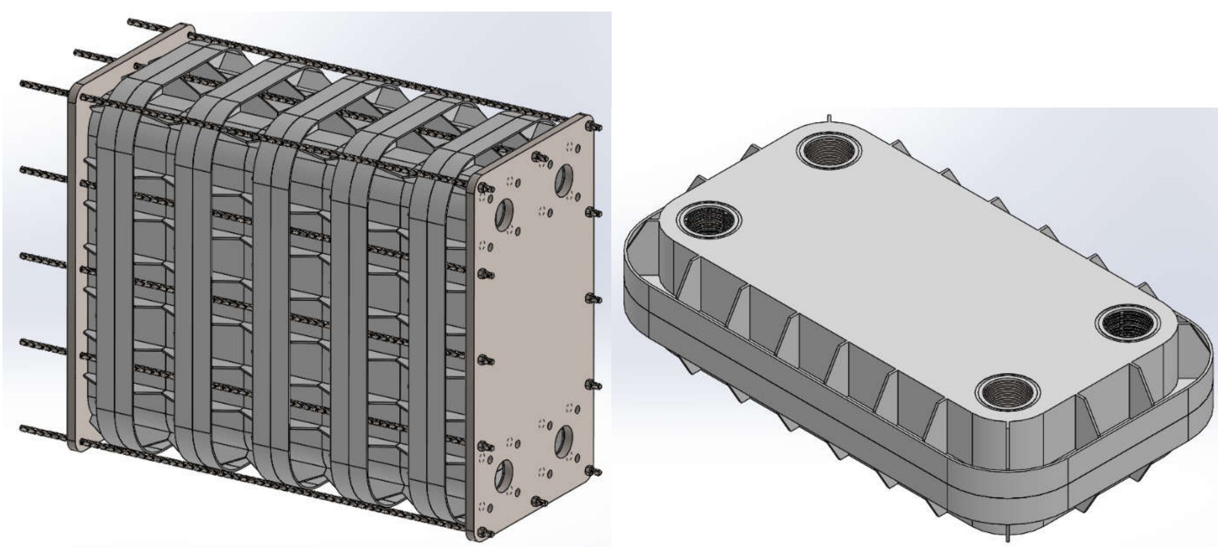

Figure 5. Potential (preliminary) design for modular concept. Each module contains ~ 100 plates and modules are stacked together to form complete TFHX units.

2.4. TFHX HIGH-SPEED WELDING

Makai has been developing a method to fabricate TFHX plates on a production rather than a prototype scale. A production scale process reduces not only the time required to make TFHX plates but also the overall cost of each plate. As discussed in Section 3.7.4, Makai has made substantial improvements in reducing the materials cost of the TFHX from $1,447/m^2 in TFHX-3B to $327/m^2 in TFHX-3E. Materials costs have been reduced from over 50% to about 25% of the overall TFHX cost/m^2. In TFHX-3E, Labor and Overhead contribute to 75% of the overall TFHX cost. With the High-Speed Weld Station (HSWS), Makai aims to reduce the Labor + Overhead portion of the total cost, which will significantly reduce TFHX fabrication time and cost.

The current fabrication process can be broken down into 3 general steps:

1) Foil preparation: This step is currently outsourced.

2) Welding and forming: this step includes placing two pieces of foil in a fixture for welding and then placing the welded plate into the forming apparatus to form the required passages.

3) Plate stacking: this step includes trimming the excess foil and stacking the individual plates. This step involves removing the formed plate, tearing off the excess foil, and setting the plates aside for designated use (characterization tests, performance tests). Plates are manually stacked into housings for performance testing or installed in characterization test fixtures.

The most significant improvement to the current process can be attained by automating Step 2. With the HSWS, Step 2 becomes automated except for the initial setup and final manual removal of the plate. Full automation of the fabrication process can be achieved when Steps 1 and 3 are integrated, but bulk of the time and cost savings is realized by designing the HSWS for Step 2. The systems and techniques utilized in the HSWS are directly adaptable to fabrication of future yet-to-be-designed TFHX plates, with modifications required to the fixtures only to accommodate a different size/shape of plate.

The key difference that enables the reduced fabrication time (and cost) in the HSWS compared to the current process is a change in optics of the welding process. For a single position, the new optics have a larger working area and require only one axis of motion to bond a full-size TFHX plate. This reduces the time required for welding because: 1) the new optics can weld the same area faster than the previous optics and 2) the entire workable area is covered with shield gas so there is no delay to maintain shield gas coverage after each individual weld.

One technical challenge is to maintain positional accuracy between the optics and the stage. The optics-to-stage mounting mechanism must be rigid enough and damp vibrations such that we can repeatably weld a spot within 50 microns.

The welding-forming fixture holds the TFHX plate and is mounted on a carriage that sits on the stage. The carriage moves in one direction (along the length of a TFHX plate) using a

NEMA 34 stepper motor. Wiring for the encoder and end of travel limit switches are run through the energy chain.

Currently, after the plate is welded, the plate is removed from the stage and placed in a separate forming fixture. In the HSWS, after welding is complete, the carriage seamlessly moves the plate into the forming apparatus. The forming apparatus is similar in design to the one currently used, only larger to accommodate more plate geometries. Once forming is complete, the carriage returns to its initial position where the completed TFHX plate is manually removed from the fixture and a new set of foil is installed.

The precise time it takes to produce a plate depends on the size of the plate and the plate design. With the HSWS, Makai estimates it would take less than 2 minutes to weld a 285 mm X 500 mm plate. The forming process is estimated to take about 2 minutes, and the time to place and remove the foil/plates from the fixtures should be less than 2 minutes. A TFHX plate can be constructed in less than 6 minutes in the HSWS compared to 1 hour at the current prototype scale.

The subsystems for the HSWS are similar to the existing subsystems. These include: laser and optics, shield gas delivery, cooling, hydraulics, and safety systems to protect both the operator and the equipment. Additional sensors, control valves, and control software are required to automate the process.

The HSWS is in the final design review and procurement stage. Assembly and commissioning are expected by the end of Spring 2020.

2.5. TFHX CHARACTERIZATION

Makai started a comprehensive testing program to determine the TFHX's geometric, mechanical, and thermo-hydraulic characteristics with empirical data. Geometric characterization includes the internal effective channel spacing and cross-sectional flow area. Mechanical characterization includes burst pressure and fatigue life. Thermo-hydraulic characterization includes pressure loss and heat transfer coefficients in single-phase and two-phase operating conditions.

TFHX passages have varying widths and cross-sectional areas and the weld itself is an obstruction in the internal fluid flow path. Makai believes these features contribute to the TFHX's strong heat transfer performance by reducing the film thickness under condensing conditions and by accelerating and decelerating flows in single-phase conditions. The ability to produce the designed channel size and shape is an important component of TFHX development.

2.5.1. Geometric Characterization

With geometric characterization, the goal is to establish the parameters – material (e.g., titanium or stainless steel), foil thickness, weld diameter, weld spacing, and forming parameters – required to create a specific channel size and shape. The internal channel shape is ellipsoid in one direction and saddle shaped in another direction. Makai has defined the following terminology used to characterize the internal channel (Figure 6):

- Weld diameter – the diameter of the weld
- Weld spacing – the distance from weld center to weld center
- A-A height – the height of the saddle
- B-B height – the maximum height of the internal passage

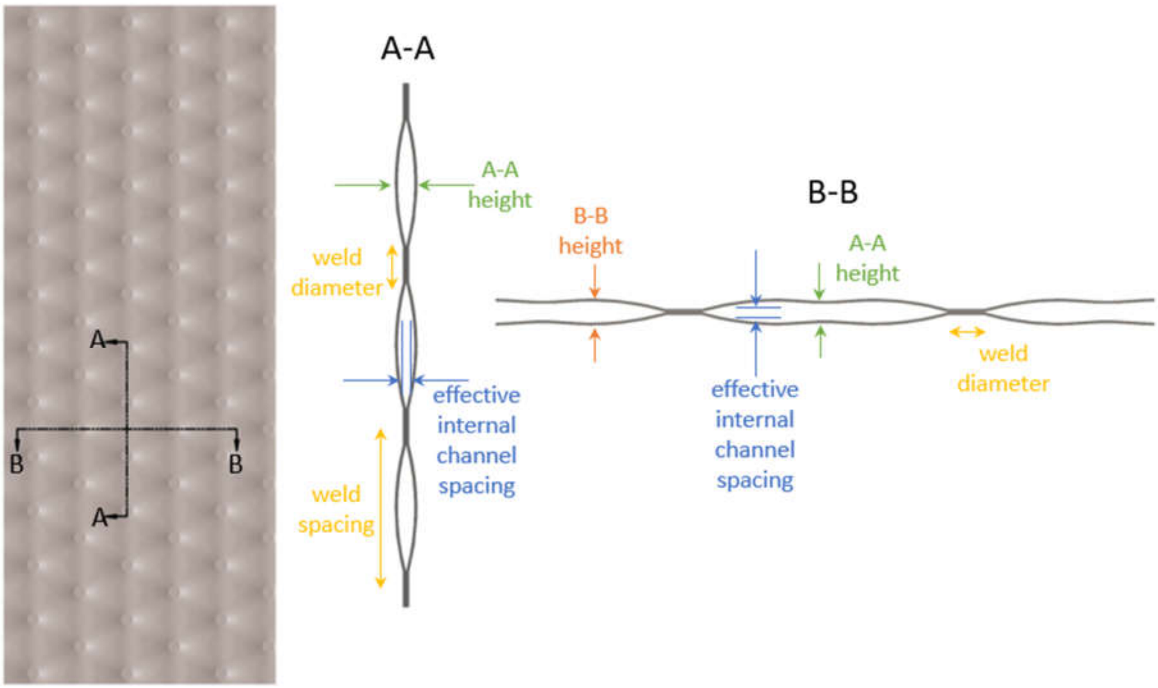

Figure 6. Schematic of geometric definitions.

- Effective internal channel spacing – the effective channel spacing is calculated by finding the internal volume of a hexagonal area outlined by the centers of the six nearest welds surrounding a single weld (in the main heat transfer region) and dividing it by the surface area. Volume is calculated from height measurements taken by scanning the surface with a profilometer. Surface area is the two-dimensional hexagonal area minus the weld area, it does not account for any increase in surface area due to curvature.

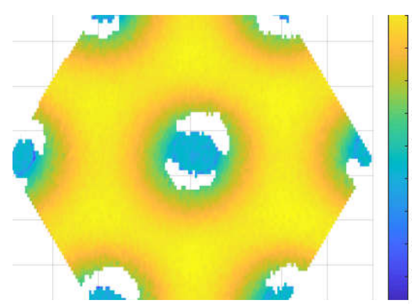

Figure 7. Hexagonal area used to calculate effective internal channel spacing.

To date, geometric characterization has focused on how parameters affect the effective internal channel spacing. The welds used in the main pattern area have been limited to dot welds of 0.88 mm diameter; circle welds with larger diameters, such as those used for transition welds, have not been characterized for the main pattern. Dot welds have been studied first because the small weld size maximizes the effective heat transfer area. By varying the parameters, it is likely possible to achieve the same effective channel spacing but have different A-A and B-B heights, and therefore, different mechanical and thermo-hydraulic properties.

The effective internal channel spacing variation with forming parameter for weld spacings between 3 mm to 6 mm and titanium foil thicknesses of 0.003” and 0.004” is shown in Figure 8. Smaller weld spacings, lower forming parameters, and thicker foil produced smaller effective spacings. The effective spacing is measured at several different locations for each plate and averaged. The effective spacing of plates constructed using the same parameters are also averaged together. For some combinations of plate type and forming parameter there is significant variability in the effective channel spacing within a single plate. This variability is attributed to the way the effective spacing is measured; if the plate is not flat (parallel) to the plane of measurement, the profilometer measurements will be biased.

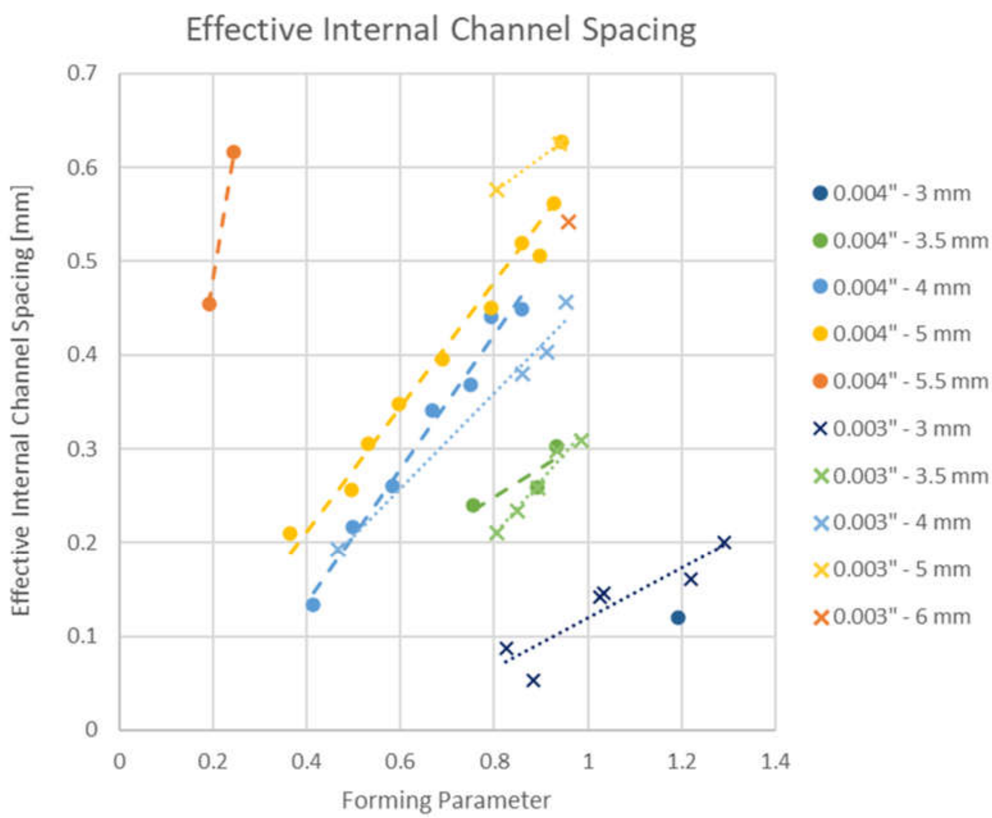

Figure 8. Average effective internal channel spacing for titanium foil using dot welds depends on foil thickness, weld spacing, and forming parameter. Smaller spacings, lower forming parameters, and thicker foils lead to smaller channel spacings.

Makai has been able to use this data to reasonably estimate the required weld spacing to produce a specified effective channel spacing. With only minor adjustments to forming parameter and transition patterns, the desired channel spacing is produced within a few iterations.

2.5.2. Mechanical Characterization

The mechanical properties are used to establish the operating pressures and predicted lifetime of a heat exchanger. Supported and unsupported burst pressures are used to determine the pressure rating while fatigue testing is used to predict the lifetime of the heat exchanger. The factors that affect supported and unsupported burst pressures are foil material, foil thickness, weld spacing, and weld diameter. Fatigue life is affected by the same factors and also the forming parameter and the loading conditions. Initial testing also revealed the overall plate shape affects burst pressures and fatigue.

(1) Burst Pressure

Burst pressure testing includes supported and unsupported tests. Ideally, a minimum of three samples for each configuration are tested to determine the average and standard deviation in burst pressure. Configurations with high standard deviations require additional examination to determine the cause of the variability. For some configurations, there were less than 3 samples tested, additional samples will be fabricated to complete the data sets.

In the supported burst pressure test, a plate is expanded until failure and the pressure at failure is recorded as the supported burst pressure.

In general, smaller weld spacings resulted in higher supported burst pressures (Figure 9). For the same weld spacing, thicker foil and a symmetric plate shape increased the supported burst pressure. At the weld spacings of 4 mm and less, the burst locations were in the transition zone whereas at larger weld spacings, the burst locations were in the pattern. This suggests at the tighter weld spacings, the burst pressure could be increased by improving the transition welds. The two data points for 0.003" Ti foil at 4 mm weld spacing are the result of the same pattern weld spacing but different transition weld diameters.

The standard test plate has a uniform width of 100 mm; however, one of the key advantages is the ability to customize the TFHX shape. Supported burst pressure testing was performed on plates with the same pattern weld design, but different overall plate shape (and therefore, different area/length occupied by the pattern weld, Figure 10). The transition weld design also remained the same, but the area occupied by transition welds was different between plate shapes. Changing the overall plate shape lowered the supported burst pressure and, in one case, changed the point of failure from the transition to the pattern (Figure 11).

The supported burst pressure testing has revealed that determining the burst pressure of the pattern is not straightforward; the stress concentrations change with the overall shape of the plate and for the tightly spaced welds tested, the burst pressures should be associated with the parameters of the transition weld, not the pattern weld. In order to determine the pattern weld burst pressures, the transition welds need to be stronger. Ultimately, burst pressure tests will be performed on each final plate design to account for the overall plate shape and associated stress concentrations.

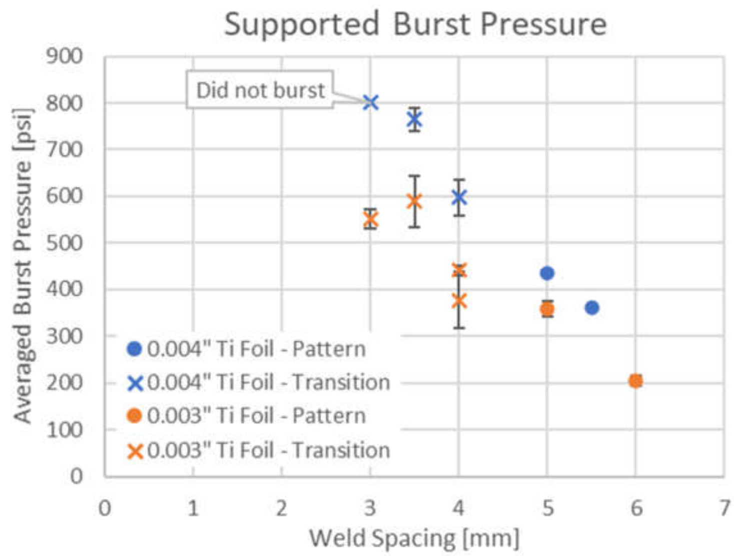

Figure 9. Supported burst pressure dependence on weld spacing and foil thickness. Vertical bars show one standard deviation.

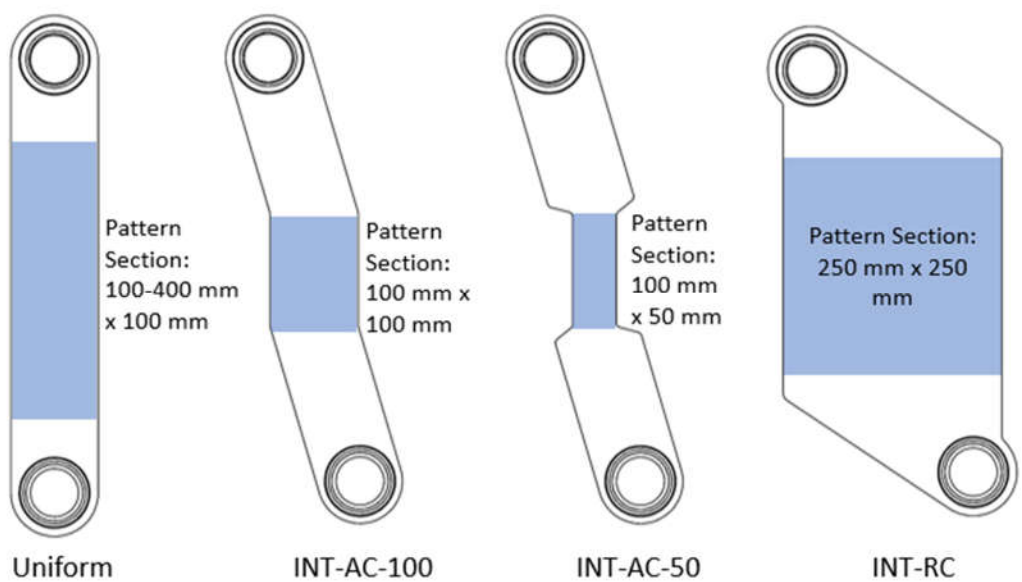

Figure 10. Variation overall plate shapes. The shaded area represents the pattern weld area, transition welds occupy unshaded areas. In the uniform plate shape, depending on the design, the pattern section length is variable; the pattern section can occupy a small section in the middle of the plate to nearly the entire length of the plate.

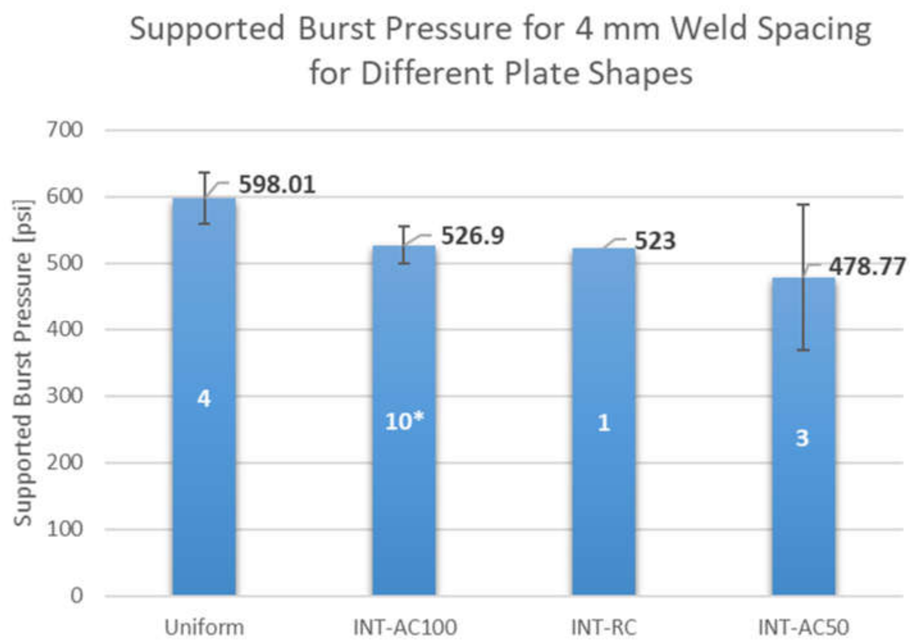

Figure 11. Effect of plate shape on supported burst pressure. The numbers in the middle of the columns indicate the number of samples tested, vertical lines show one standard deviation. The failure location was transition welds except in INT-AC100 where the failure location was the pattern welds.

In the unsupported test, the plate is put into a pressurization fixture in which only the manifolds are clamped (to provide the seal). The plate is then expanded until failure. The unsupported burst pressure test is used to establish the pressure rating of a TFHX plate. Pressurization in the unsupported burst test is representative of loading in an operational TFHX heat exchanger where each individual TFHX plate meets the pressure rating and external support is provided only to compress the o-rings used to seal the internal from the external passages.

In order to identify preliminary trends, initial unsupported burst pressure tests were performed on samples with the same pattern and transition weld designs but with variations in foil thickness, forming parameter, and plate shape (Figure 12). For the same foil thickness and plate shape (uniform), plates with a lower forming parameter had a higher averaged unsupported burst pressure and less variation in the individual unsupported burst pressures, but the difference is not statistically significant (*p-value* = .28). The 0.003” uniform plate samples had statistically significant lower unsupported burst pressure compared to the 0.004” uniform plate samples. The non-uniform, INTRC plate, introduced two variables, plate shape (INTRC) and forming parameter. Compared to 0.004” uniform plate samples, there was no statistically significant difference (*p-value* = .05 and .06) in unsupported burst pressure, but the result is on the borderline of statistical significance (*p-value* = .05) and likely due to the variability in the burst pressures within a single configuration.

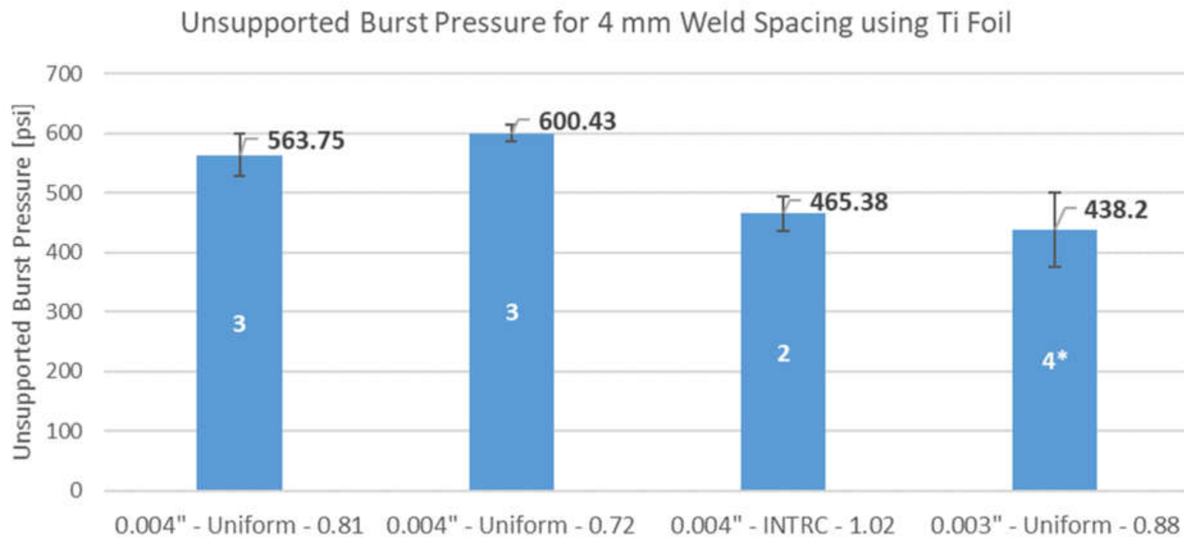

Figure 12. Unsupported burst pressure testing on samples with 4 mm pattern weld spacing and variations in foil thickness, forming parameter, and plate shape. The 0.004" samples failed at pattern welds whereas the 0.003" samples failed at transition welds.

Unsupported burst pressure testing has only been conducted on a few samples and the results are so far inconclusive. As expected, thinner foil (0.003" vs 0.004" Ti foil) has a lower overall burst pressure. The overall plate shape and the forming parameter (which directly correlates to the effective internal channel spacing) were also expected to affect the unsupported burst pressure, but the limited data set indicates no statistically significant difference. Additional testing is recommended before drawing conclusions on the relationship between the forming parameter and the overall plate shape on unsupported burst pressure. The effect of weld spacing will also be included in future unsupported burst pressure tests.

(2) <u>Fatigue Testing</u>

Initially, fatigue testing used high pressure compressed air from a cylinder to pressurize a water-filled TFHX plate. A regulator controlled the pressure amplitude and a solenoid valve controlled the cycling time. This initial test setup was inefficient because the compressed air cylinders would have to be replaced daily. A revised design uses linear motors to provide the pressure cycling. The amplitude of cycling can be set by changing the stroke length. Twelve plates can be simultaneously tested in the revised fatigue testing apparatus (Figure 13).

Figure 13. Revised fatigue testing apparatus. Twelve plates can be (independently) tested simultaneously.

The standard fatigue testing plate utilizes 3E-style manifolds and is 100 mm wide by 596 mm long. The pattern region is in the middle of the plate with a transition region between the pattern and each manifold.

In addition to testing variations in the plate type and plate fabrication parameters, fatigue testing includes additional parameters such as mean pressure, alternating pressure, and r-value (ratio of minimum/maximum pressure). Typically, developing an exhaustive set of S-N curves provides information about the expected material performance. Makai's initial approach was to fabricate many samples (3-5 per test condition) of each plate type and develop an S-N curve for each plate type.

In preliminary testing, we observed that for the same plate type tested under the same cyclic pressure range (0-120 psig), samples with lower forming parameters failed earlier than samples with higher forming parameters (Figure 14). Our fabrication guidelines now specify a forming parameter of 0.75-0.95.

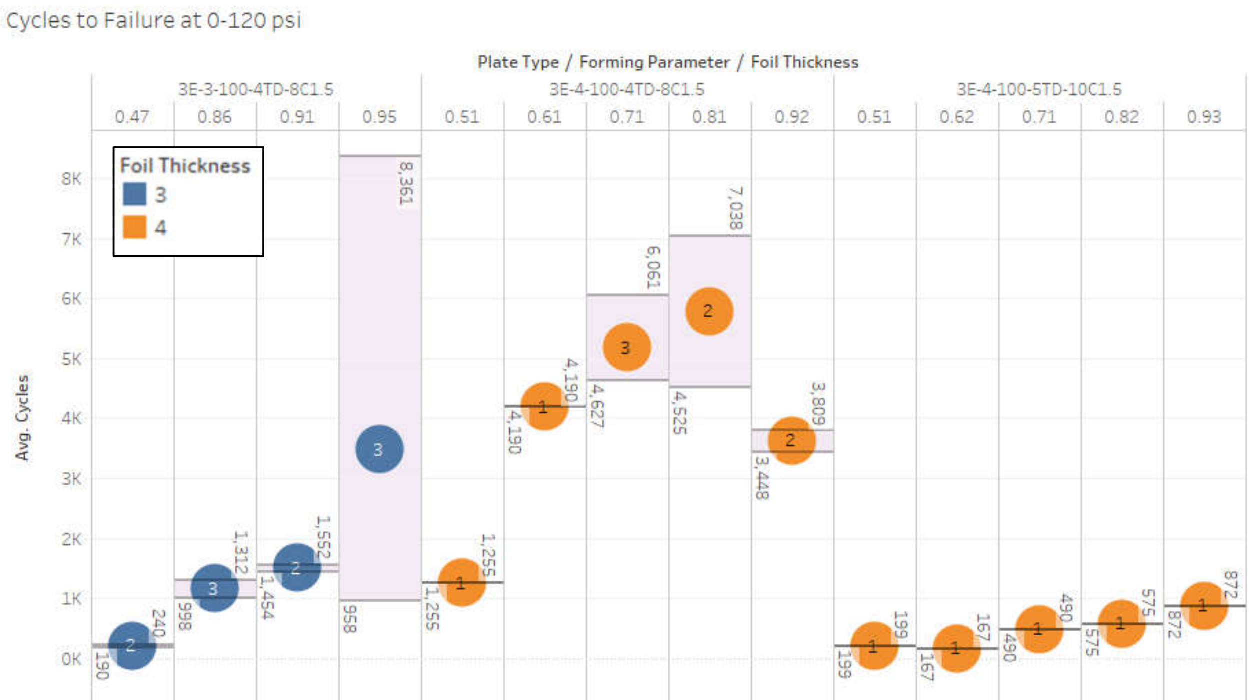

Figure 14. Fatigue cycle dependency on forming parameter. This data shows only samples that were cycled from 0-120 psi. The averaged # of cycles to failure is plotted with shaded band indicating the maximum and minimum # of cycles to failure. For some forming parameters, there was only one data point. In general, lower forming parameters led to fewer cycles to failure for both 0.003" and 0.004" foil thicknesses. Either the seal or transition welds failed at the seal (perimeter) or near the manifold. Fatigue failures did not occur in the pattern welds.

When the data is grouped together by cyclic loading conditions, data suggests high alternating pressures lead to shorter fatigue life (Figure 15). The mean pressure does not appear to have as much of an effect on fatigue life as the alternating pressure. For 3E-3-100-5TD-10C1.5, samples tested at 60-120 psi (90 psi mean pressure ± 30 psi alternating pressure) reached more cycles before failure compared to samples tested at 0-120 psi.

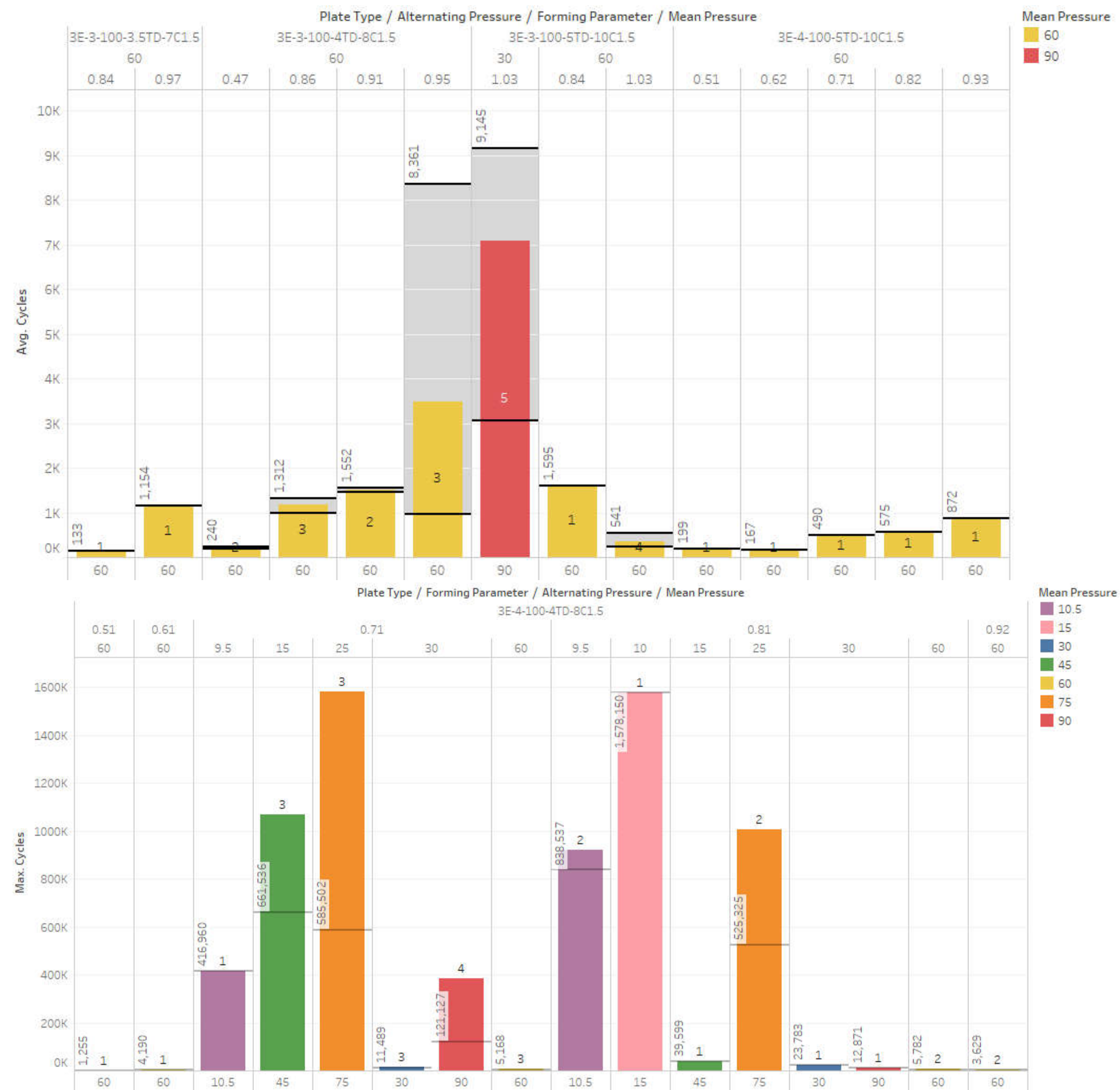

Figure 15. Averaged cycles to failure for each plate type, broken down by forming parameter and loading condition. Loading condition is specified by the mean pressure (average of min and max pressure) and alternating pressure (max pressure – average pressure). The solid bars show the maximum cycles to failure with the color of the bar represent the mean pressure. The line shows the average cycles to failure. The number of samples for each loading condition is shown above the solid bar.

Eight tests were stopped before a failure occurred (Figure 16). These samples were tested in loading conditions with alternating pressures ≤ 25 psi. Six tests had reached over 900,000 cycles.

Mean Pressure	Alternating Pressure	Forming Parameter 0.71	0.81
10.5	9.5	416,960	838,537
15	10		1,578,150
45	15	984,216	
75	25	1,579,492	1,007,204

Figure 16. Loading conditions and number of cycles completed before fatigue testing was stopped on 3E-4-100-4TD-8C1.5 type samples with forming parameters 0.71 and 0.81. Blue numbers indicate single sample, orange indicates the average of two samples. Six sample reached over 900,000 cycles.

For the 52 fatigue samples that were tested to failure, the pattern weld was the point of failure in only four samples and the failure locations were either at the seal weld or adjacent to a transition weld (Figure 17). There were no failures in the middle of the pattern weld region. All other failures were transition welds or seal welds and the location was at the perimeter of the plate, near the manifold, or in the transition zone.

Failure Weld	Failure Location: manifold	multiple	seal	transition	no failure
pattern			1	3	
seal	21	1		1	
transition	12		11		
no failure					8

Figure 17. Fatigue failure welds and locations.

The results suggest either the seal weld and transition welds are weaker in fatigue or there may be a bias introduced by the plate types chosen for testing. In the unsupported burst pressure tests, the transition welds were the point of failure for plates with pattern weld spacings ≤ 4 mm. The four pattern weld failures in the fatigue testing occurred on the plates with 5 mm pattern weld spacing. However, in 10 out of the 15 plates tested that had 5 mm pattern weld spacing, the transition weld was the weld that failed (Figure 18).

For the samples tested, transition weld failures have occurred either at the manifold or seal weld. These areas are on the outer limits of the uniform transition weld zone and also most likely to have uneven stresses or non-uniform channel shapes that are likely to be more susceptible in fatigue. Additional work may be necessary to strengthen the transition welds, but, as observed in the supported burst testing results, the overall plate shape, which can be customized for a specific application, is likely to affect the stress distribution. The most accurate and representative fatigue results will require testing on the final plate design and it is possible that the design process may be iterative pending test results.

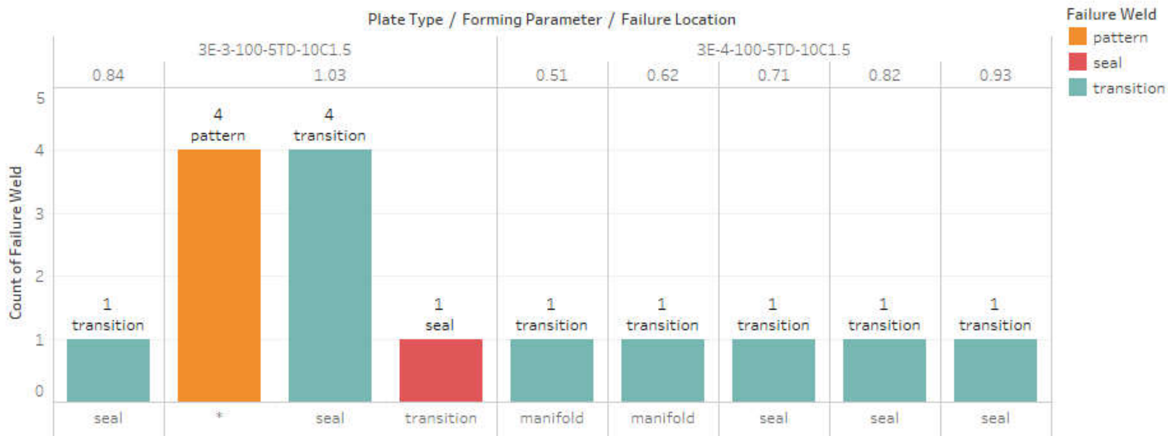

Figure 18. Breakdown of failure weld and failure location for samples with 5 mm pattern weld spacing.

Makai is testing two modifications to determine if the seal weld requires re-design or if the prototype fabrication process has introduced residual stresses on the seal weld that cause early failure under fatigue conditions. Currently, after a fatigue plate is fabricated, the excess foil is removed manually by tearing along the seal weld. First, samples will be fabricated with a second seal weld outside the required seal weld and the excess foil will be torn along the edge of the second seal weld. The area between the seal welds is not pressurized and will not be exposed to the cyclic loading. This test will demonstrate whether the tearing process puts residual stress on the seal weld and contributes to fatigue failure. Second, in a high-volume fabrication process, a cutting operation will be used to remove the excess foil. This process will be simulated using a paper cutter or scissors, leaving a wider margin (more excess foil) around the seal weld. This method should also prevent introducing additional stresses on the seal weld. Fatigue testing on these samples will provide information on whether the process for removing excess foil affects the seal weld.

An additional factor to consider is the effect of the forming parameter on the seal weld. Plates have been burst tested up to 800 psi with failure locations in the transition or pattern weld. If the seal weld design requires a different forming parameter, it is possible the seal weld also undergoes cyclic strain that leads to fatigue failure.

TFHX plates can be asymmetrical, non-rectilinear, with customized manifold and overall plate shapes and variations in weld designs within the main heat transfer area to optimize thermo-hydraulic performance. It is unlikely that the stress conditions will be the same as in the uniform testing plates. Makai has concluded that an exhaustive set of fatigue data on uniform plates is impractical, unlikely to be representative of a custom plate design, and may inadvertently bias design decisions. Additional fatigue testing will be performed on uniform plates to learn about the seal weld and general expectations for the pattern and transition welds, but the most reliable and representative data will require fatigue testing of the final plate design under applicable loading conditions. Instead of developing an S-N curve for each pattern weld design, it is more useful to test the final plate design under the specified conditions of the application to ensure the design meets both startup and operational lifetime/life cycle requirements.

2.5.3. Hydraulic Performance

The hydraulic performance of the internal channels is used to determine the minimum internal effective spacing and maximum length of the TFHX plate. Makai developed a test fixture to measure the pressure drop of the internal fluid for different internal channel sizes. Fluid pressure drops can be measured at different flow rates and temperatures (up to 105°C). During pressure drop testing, fluid is pumped through the internal channel of a single TFHX plate and the mass flow rate is measured by a Coriolis meter. The flow rate is adjusted by increasing/decreasing pump motor speed. Pressure sensors record the fluid pressure at the inlet and outlet of the TFHX plate.

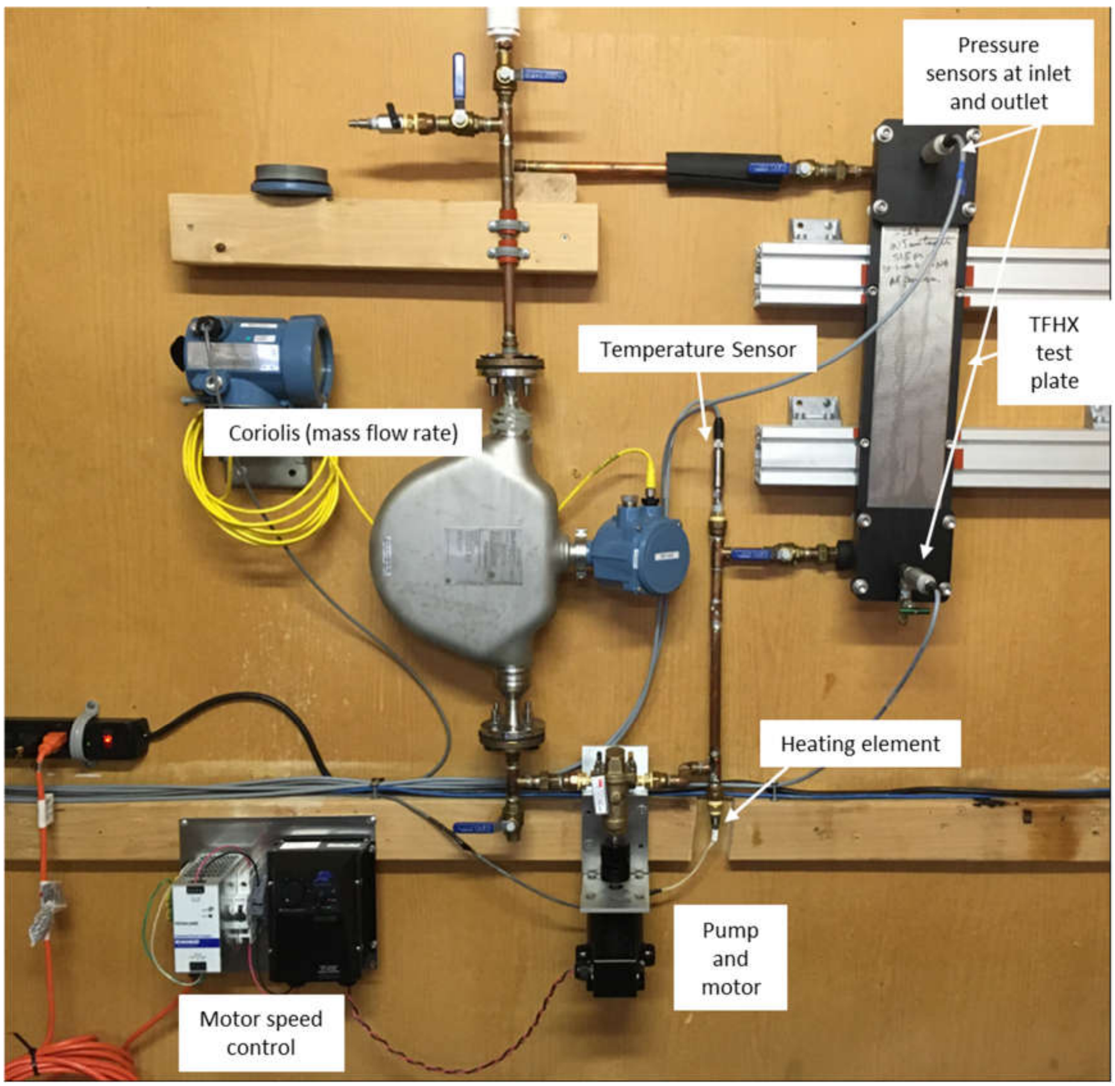

Figure 19. Pressure testing apparatus.

(1) Instrumentation

Instrument	Model	Range	Accuracy
Mass Flow Rate	Coriolis CMFS025M	0-0.31 kg/s	±0.1%
Temperature	Coriolis CMFS025M	0-204°C	±1 ± 0.5%
Density	Coriolis CMFS025M	0-5000 kg/m^3	±0.5 kg/m^3
Inlet Temperature	Endress Hauser TMR31	0-150°C	±0.25 ±0.2%
Inlet/Outlet Pressure	GE Druck UNIK5000	0-100 psia	±0.1% FS

(2) Calculations

Velocity. The fluid velocity is calculated by dividing the recorded mass flow rate by the density and the cross-sectional flow area.

Pressure Drop. The pressure drop is calculated by subtracting the outlet pressure measurement and static head from the inlet pressure measurement. Static head is the difference in inlet and outlet pressure at no flow.

(3) Data Collection and Data Processing

A custom developed Labview-based program and commercially available Pro-Link software (interface for the Coriolis flow meter) were used to collect data. The pressure, temperature, and mass flow rate measurements are output as a 4-20 mA signal, proportional to the measurement, which was read using National Instruments' NI 9208 Analog Input modules. Measurements were sampled 10X a second, averaged, and recorded every second. Density and temperature measurements from Coriolis were recorded every second via a serial to USB connection using the Pro-Link software.

The measured pressure-drop includes the effects of the manifold and a "transition zone" in addition the main heat transfer area pattern. The manifold and transition design are unique for each application, but in a well-designed heat exchanger, should only comprise a small portion of the overall pressure drop (target < 5%). In order to isolate the pressure-drop specific to the heat transfer area, for each internal channel size, four plates, with varying heat transfer area lengths were tested.

For each plate, the measured pressure drop was plotted versus the mass flow rate and fitted with a second order polynomial. For each internal channel spacing, the pressure drop for each plate was then re-calculated using the fitted equation at specified mass flow rates. This is important to ensure the pressure drops are compared for the same mass flow rate. Using the lengths of the transition and pattern regions and counting the manifold pair as 1, the pressure drop per manifold pair, transition length, and pattern length was solved using the least squares method. The fourth all-pattern plate was used to verify the solution.

For example, if M = loss through the manifold pair [kPa], T = pressure drop per mm of transition zone length [kPa/mm], and P = pressure drop per mm of heat transfer pattern length [kPa/mm], then for the same mass flow rate, $\begin{bmatrix} 1 & 332.6 & 27.7 \\ 1 & 166.3 & 194.0 \\ 1 & 304.8 & 55.4 \end{bmatrix} \times \begin{bmatrix} M \\ T \\ P \end{bmatrix} = \begin{bmatrix} dP\ short \\ dP\ mid \\ dP\ long \end{bmatrix}$. The coefficient matrix represents the manifold pair, transition length [mm], and pattern length [mm] for the short, medium, and long plates. By solving for M, T, and P at different mass flow rates, a curve can be developed for pressure loss per mm pattern vs mass flow rate in a 99 mm wide plate. By using the pattern cross-sectional area, the pressure loss can also be plotted vs fluid velocity, which is then used in the TFHX model to determine the hot fluid pressure drop in plates of different lengths and widths.

(4) Results

Five different internal channel spacings were tested (Table 1). As described in (3), four plates with varying transition zone and heat transfer area lengths were tested per internal channel size. Makai used water, Prestone Command 50/50 ethylene glycol/water mixture (EGW), and Shell Rotella T4 15W40 for testing.

Table 1. Pressure drop testing plates internal channel size and test fluids.

Internal Channel Spacing [mm]	0.142	0.2325	0.25	0.407	0.5455
Fluid(s) and Temperature	EGW at 50C and 100C	Water at 25C	EGW at 50C and 100C	EGW at 50C and 100C, 15W40 at 100C	Water at 25C

The pattern pressure drop per mm vs velocity is show in Figure 20 with the fitted equations used in the TFHX model to calculate the hot fluid pressure drop.

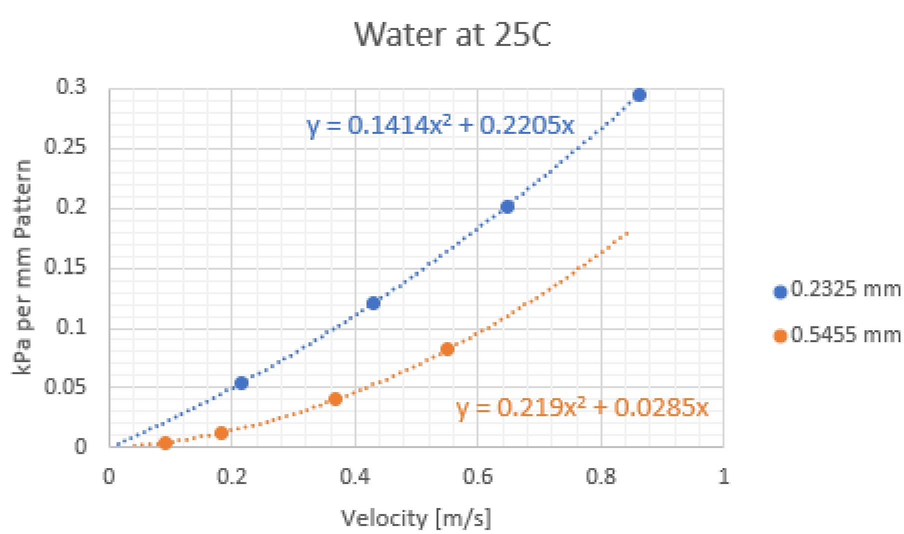

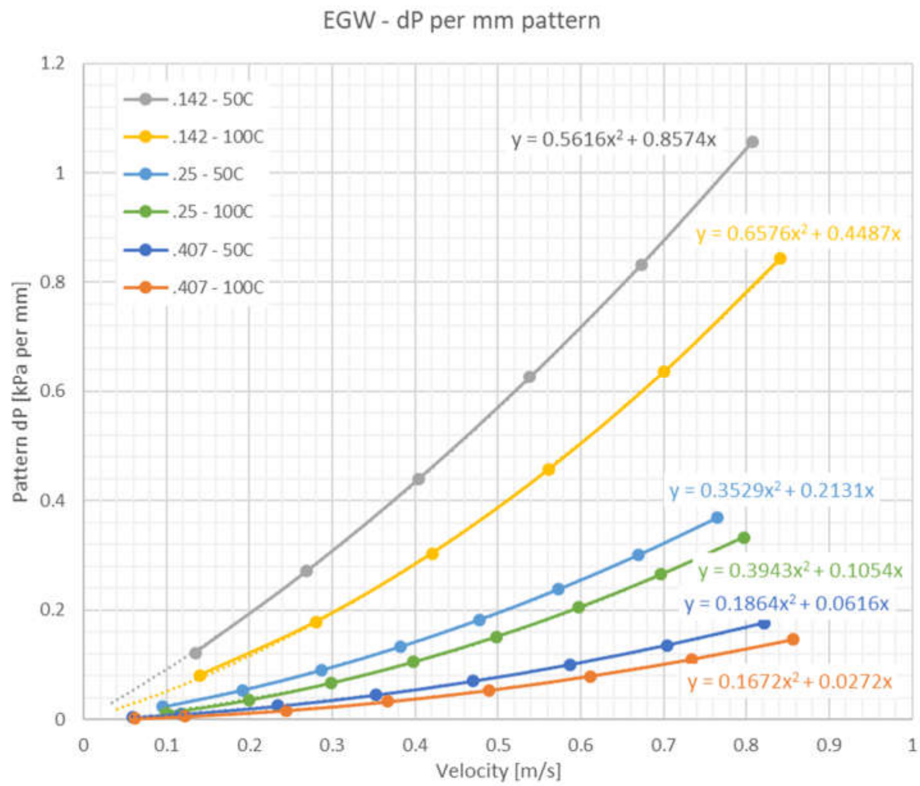

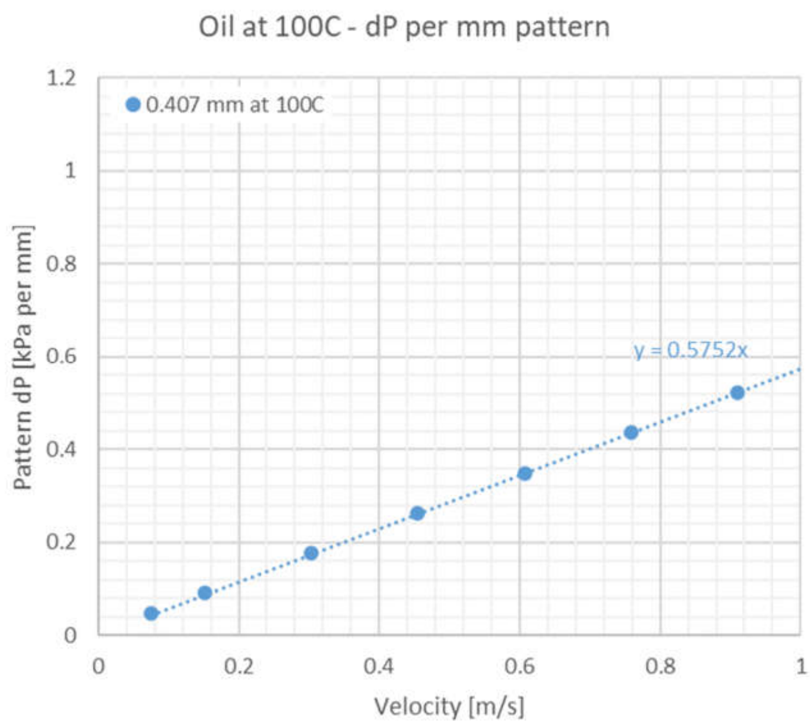

Figure 20. Calculated pressure loss per mm of pattern length for different fluids and internal effective spacings.

2.6. SUMMARY

In this period, Makai has made significant improvements to individual TFHX plate design, developed methods to assemble TFHX plates to form a complete heat exchanger unit, completed the design for the High-Speed Welding Station, and started to characterize the effect of weld design on the geometric, mechanical, and hydraulic performance of TFHX plates.

Individual TFHX plates have undergone two manifold design iterations. The design of the current 3E style manifolds is proprietary. In addition to reducing the overall component cost and fabrication time, the 3E manifolds reduced the non-interlocking plate spacing from 3.9 mm to 2 mm; with interlocking plates, the plate spacing in 3E is down to 1 mm (from 1.3 mm in 3C). The 3E style manifold provides a 1.3-2X increase in heat transfer area density compared to 3B and 3C style manifolds.

Individual TFHX plates are stacked together to form a heat exchanger unit, which requires some external structure to provide o-ring compression and duct the internal and external fluids. Makai has created two broad categories for the housing design: fully-enclosed or pass-through. The performance testing units constructed to date have been fully-enclosed units whereas Makai constructed and installed a pass-through unit for Cyanotech.

While assembling performance testing units, particularly units with small external channel spacings, Makai identified the need to incorporate a fixed feature in the plates to maintain plate spacing. Spacers and washers have been used with limited success on small (<30) stacks of plates. Installing spacers during assembly is time consuming and impractical when stacking hundreds of plates; some spacers also dislodged during testing, making spacers unreliable when maintaining plate spacing is critical. Makai is testing a proprietary feature to maintain plate spacing.

Makai has completed the design of the High-Speed Welding Station and is in the process of constructing the station. The HSWS is expected to increase the plate production rate by a factor of 5. Along with the developments in housing design and ability to maintain plate spacing, the HSWS will enable production of full-scale TFHX units.

Finally, in the process of TFHX characterization, Makai learned that the effective internal channel spacing can be reasonably predicted by setting the pattern weld spacing and forming parameter. The hydraulic performance of tested fluids can also be predicted per unit length of pattern. However, the pattern weld parameters alone do not define the supported and unsupported burst pressures and cycles until fatigue failure. A comprehensive plate design, which includes the overall plate shape, the manifold opening shapes, transition weld design, foil removal method, and the pattern weld design, is required to establish the mechanical properties of the TFHX plate, particularly for asymmetrical/non-uniform overall plate shapes.

3. CROSSFLOW TFHX: AMMONIA – SEAWATER HEAT EXCHANGER TESTING

Four ammonia-seawater heat exchangers – TFHX-3C-1 through TFHX-3C-3 and TFHX-3E-INT1 – were tested at the 100 kW testing station. Each heat exchanger was tested as a condenser and an evaporator. Each of the TFHXs had comparable ammonia side effective spacing but the seawater side effective spacing ranged from 0.41 mm to 3.34 mm.

TFHXs were compared to previously tested heat exchangers by scaling up the TFHXs to match the duty (2MW) at the same energy density and comparing performance versus seawater pumping power or energy density. Performance metrics include: ammonia and seawater side convective coefficients, overall heat transfer coefficient, and approach temperature. For each previously tested heat exchanger, at least one TFHX configuration had better performance; for some heat exchangers, multiple TFHXs had better performance.

Since the TFHX was originally developed with OTEC in mind, a comparison between the most compact TFHX (3E-INT1) and the previously selected heat exchangers was performed using the conditions outlined in the 2.5 MW Mini Spar OTEC report. The TFHX-3E-INT1 matched the performance of the previously selected heat exchangers (brazed fin evaporator and twisted tube, shell-and-tube condenser) for about half the cost (after implementation of the High Speed Welding Station). For the same cost as the previously selected heat exchangers, the TFHX-3E-INT1 heat transfer area can be doubled and net power production is predicted to increase by almost 30%. Due to its compactness, doubling the TFHX-3E-INT1 heat transfer area still only occupies ~1/3 the volume of the previously selected heat exchangers.

3.1. OVERVIEW OF TESTED TFHX CONFIGURATIONS

The TFHX-3C style plates have a 0.285 m x 0.370 m heat transfer area, transition zones to connect the heat transfer area to the manifold, and two manifolds (inlet and outlet) (Figure 21). The plate spacing is set by the individual plate thickness, 0.153” (3.89 mm); it is defined by the sum of the manifold thicknesses (0.078” and 0.035”), pill spacer thickness (0.035”), and two foil thicknesses (2 x 0.003”). 3C was designed with the ability to interlock plates, i.e., successive plates have manifolds located on the left, center, and right side or just left and right side, which allows plate spacing to be reduced by 1/2 or 1/3 to 1.95 mm and 1.30 mm, respectively.

The TFHX-3E-INT plates have a 0.25 m x 0.25 m heat transfer area, transition zones that connect the manifold to the heat transfer area, and two manifolds (inlet and outlet, Figure 22). The transition zone includes a triangular shaped region with large, low pressure-drop channels and a 0.02 m rectangular section with the same pattern as the test section. These two regions of the transition zone are intended to ensure ammonia is evenly distributed and has uniform flow direction by the time it reaches the test section. In TFHX-3E-INT, the nominal plate spacing is 2 mm and two plates can be interlocked to reduce the plate spacing to 1 mm.

An overview of the parameters of the four heat exchangers is summarized in Table 2. The effective ammonia channel spacing is measured with the plate depressurized and the effective seawater channel is calculated from the plate spacing (based on foil and manifold thickness) and the effective ammonia channel spacing.

The data processing and analysis methods are the same for each heat exchanger and described in Appendix A.

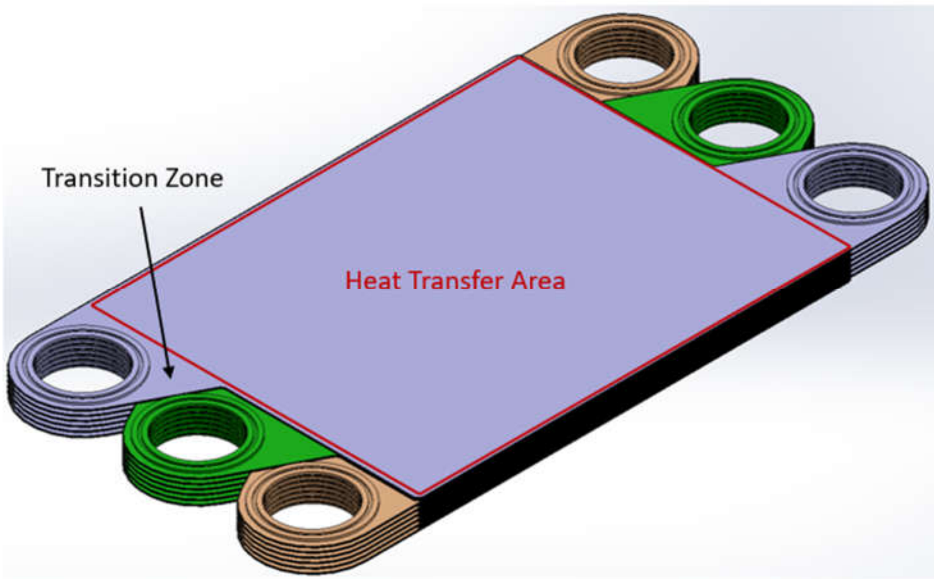

Figure 21. TFHX-3C plates.

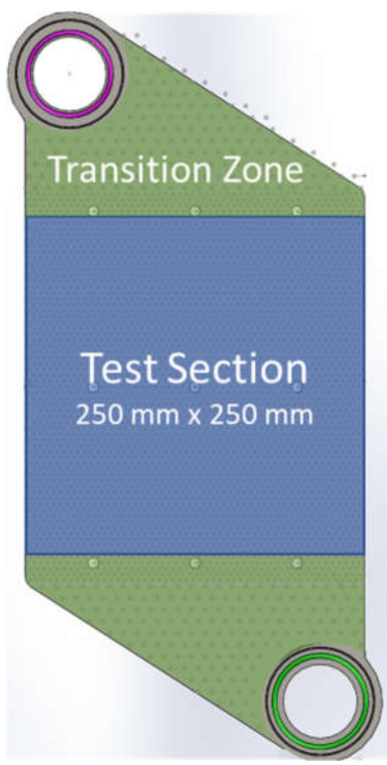

Figure 22. TFHX-3E-INT plate showing the manifolds, transition zones, and test section.

Table 2. Summary of Tested Ammonia-Seawater Heat Exchangers

	TFHX-3C-1	TFHX-3C-2	TFHX-3C-3	TFHX-3E-INT1
# plates	6	12	18	12
Effective Plate Spacing	3.886 mm	1.943 mm	1.295 mm	0.986 mm
Total Heat Transfer Area	1.16 m^2	2.32 m^2	3.48 m^2	1.4341
Effective Ammonia Channel Spacing	0.42 mm	0.42 mm	0.42 mm	0.373 mm
Ammonia Flow Path Length	0.37 m	0.37 m	0.37 m	0.25 m
Effective Seawater Channel Spacing	3.34 mm	1.40 mm	0.75 mm	0.410 mm
Seawater Flow Path Length	0.285 m	0.285 m	0.285 m	0.2495 m
Seawater Hydraulic Diameter	6.62 mm	2.78 mm	1.49 mm	0.819 mm
Seawater Cross Sectional Flow Area	0.0074 m^2	0.0062 m^2	0.0050 m^2	0.001271 m^2

3.2. TFHX-3C-1

TFHX-3C-1 consisted of six identically oriented plates, with the manifolds on the right side. Testing was conducted at various seawater flow rates and ammonia (vapor) flow rates (Table 3). For each test point, the expansion valve was maintained at 100% open and the ammonia vapor flow rate was controlled by controlling seawater flow through the companion heat exchanger.

Table 3. Overview of Condenser Test Points

			Ammonia Vapor Flow Rate [kg/s]							
	[gpm]	**[m/s]**	**0.008**	**0.016**	**0.024**	**0.032**	**0.04**	**0.048**	**0.056**	**0.064**
Seawater Flow Rate	**30**	**0.26**	x	x	x					
	40	**0.34**	x	x	x					
	50	**0.43**	x	x	x					
	58.8	**0.50**	x	x	x	x	x			
	117.5	**1.00**	x	x	x	x	x	x	x	x
	176.3	**1.50**	x	x	x	x	x	x	x	x

Table 4. Overview of Evaporator Test Points

			Ammonia Vapor Flow Rate [kg/s]						
Seawater Flow Rate	[gpm]	[m/s]	0.008	0.016	0.024	0.032	0.04	0.048	0.064
	20	0.17	x	x					
	30	0.26	x	x	x				
	35	0.30	x	x	x				
	40	0.34	x	x	x	x			
	45	0.38	x	x	x	x			
	50	0.43		x	x	x			
	60	0.51		x	x	x	x		
	117.5	1.00		x	x	x	x	x	
	176.3	1.50		x	x	x	x	x	x

* Evaporator testing was conducted at 40%, 60%, and 80% quality. Not every test point was tested for each quality.

3.2.1. Seawater Differential Pressure

Seawater-side pressure drop is related to the pumping power required to provide a certain seawater flow rate through the heat exchanger. The Darcy-Weisbach equation can be used to predict pressure drop as a function of the channel geometry and seawater velocity. The total seawater cross-sectional flow area is calculated from the effective seawater channel spacing (Table 2). The average seawater velocity is calculated from the measured seawater flow rate (in gpm) and the seawater cross-sectional flow area. The friction factor for smooth tubes, $f = (0.79 \log Re - 1.64)^{-2}$, was used. Since the overall dP includes entrance and exit losses, minor loss coefficients of 0.5 for the entrance and 1 for the exit were used. Seawater properties used in the calculations are summarized in Table 5. The variation in measured dP may be attributed to: 1) flutter in plates with increased seawater velocity, 2) uneven plate spacings either between inner plates and/or the effect of outer channel plate spacing, 3) changes in ammonia channel height due to changes in ammonia-side operating pressure, 4) error in the static head offset, and 6) limitations in sensor accuracy. The predicted dP was within 2 kPa of the measured dP (Figure 23). The effect of the outer channels has been neglected in calculating the seawater cross sectional flow area. This approximation affects calculation of seawater velocity (and therefore, Reynolds number, friction factor, and the predicted dP).

Table 5. Seawater properties used in seawater dP calculations

	Condenser	Evaporator
Temperature	6 °C	25.5 °C
Salinity	34.7 ppt	34.7 ppt
Density	1027.3 kg/m^3	1023.21 kg/m^3
Kinematic Viscosity	1.53E-6 m^2/s	9.26E-07 m^2/s
Thermal Conductivity	0.580 W/m/K	0.609 W/m/K
Prandtl Number	10.815	6.224

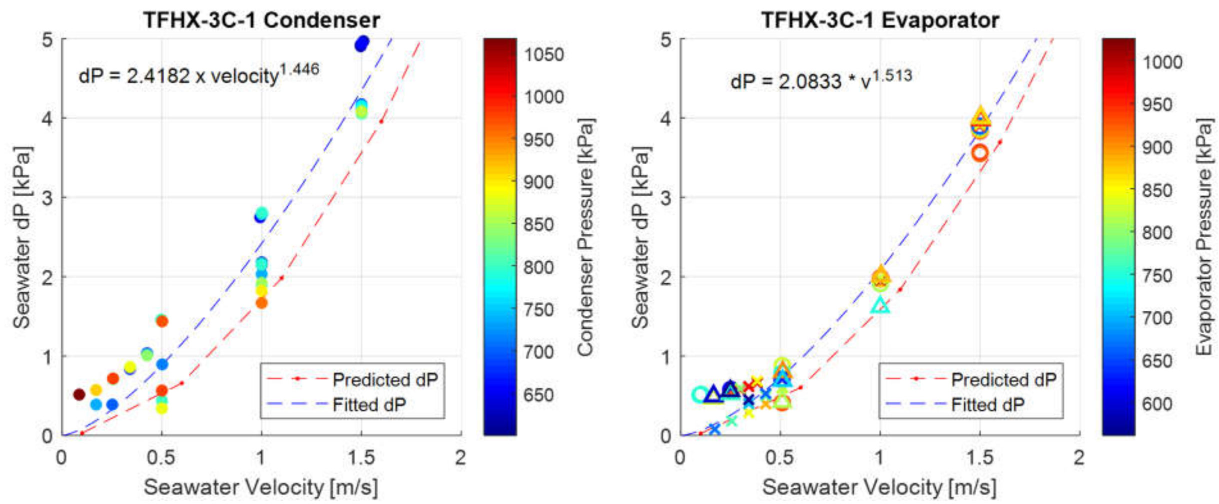

Figure 23. TFHX-3C-1 seawater pressure drop. Filled circles are data points; dotted lines represent predicted dP using the Darcy-Weisbach equation. Discrepancy at low velocities may be due to limitations in accuracy of sensors.

3.2.2. Ammonia Differential Pressure

Ammonia-side differential pressure is an important consideration for a heat exchanger. In a closed-cycle system, minimizing the pressure drop reduces the pumping power required to recirculate refrigerant and, in an OTEC system, increases the available differential pressure across a turbine. Ammonia pressure drop is strongly dependent on ammonia vapor flow rate, quality, and heat exchanger geometry.

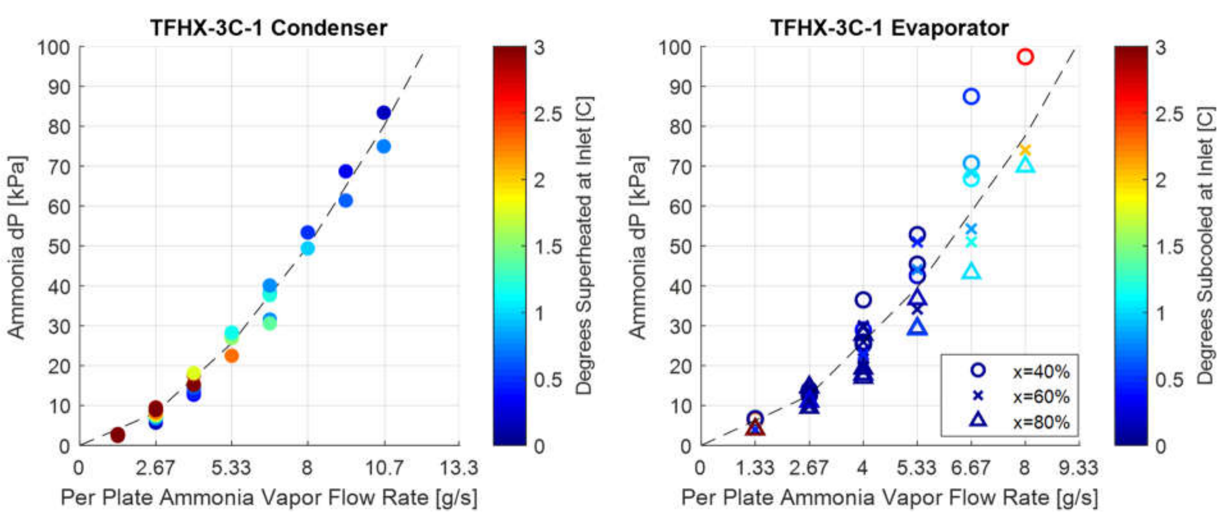

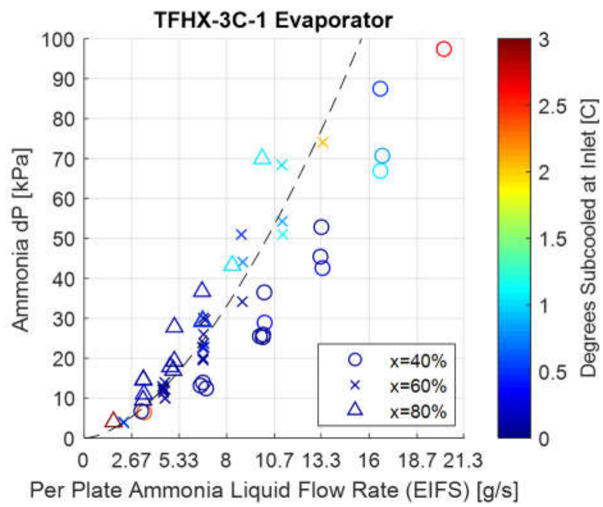

Figure 24. TFHX-3C-1 ammonia-side pressure drop vs ammonia flow rate.

Although the effective ammonia channel spacing is comparable to previously tested TFHX-3B-2 and the ammonia path length is only 33% longer, the ammonia pressure drop in TFHX-3C-1 is significantly higher. In TFHX-3C, ammonia flow is constrained by the limited flow area at the exit of the manifold (which was necessary to be able to interlock 3 plates to obtain the 0.8 mm effective seawater channel spacing). This transition zone has been redesigned for future TFHX versions.

3.2.1. Ammonia-Side Operating Pressure

Heat exchanger pressure is determined by the seawater temperature, seawater flow rate, ammonia vapor flow rate, quality (for an evaporator), and degree of subcooling/superheating. For a fixed seawater and ammonia flow rate and quality, heat exchanger pressure should only depend on seawater inlet temperature and is expected to follow the slope of the ammonia saturation curve.

In general, pressure vs. seawater inlet temperature follow closely with the ammonia saturation curves. Discrepancies were attributed to variations in seawater and ammonia flow rate (both vapor and liquid). The lack of sensitivity and hysteresis in the seawater control valves made it difficult to hold a fixed seawater and ammonia vapor flow rate. Heat exchanger pressure was also affected by oscillations in feed pump flow rate. At some test points, feed pump fluctuations translated into a +/- 2 kPa oscillation in ammonia inlet pressure and temperature.

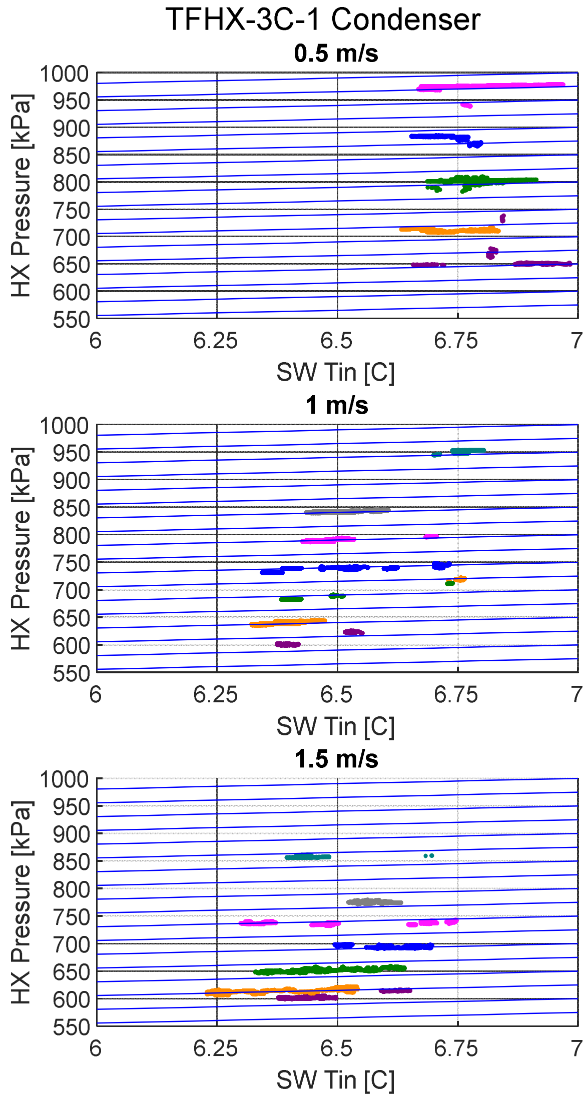

Figure 25. Condenser pressure vs seawater inlet temperature for different seawater and ammonia vapor flow rates. Marker colors: purple = 1.33 g/s, orange = 2.67 g/s, green = 4 g/s, blue = 5.33 g/s, magenta = 6.67 kg/s, grey = 8 g/s, and teal = 10.67 g/s of ammonia vapor flow per plate. Blue lines indicate the ammonia saturation curve with offsets of 25 kPa.

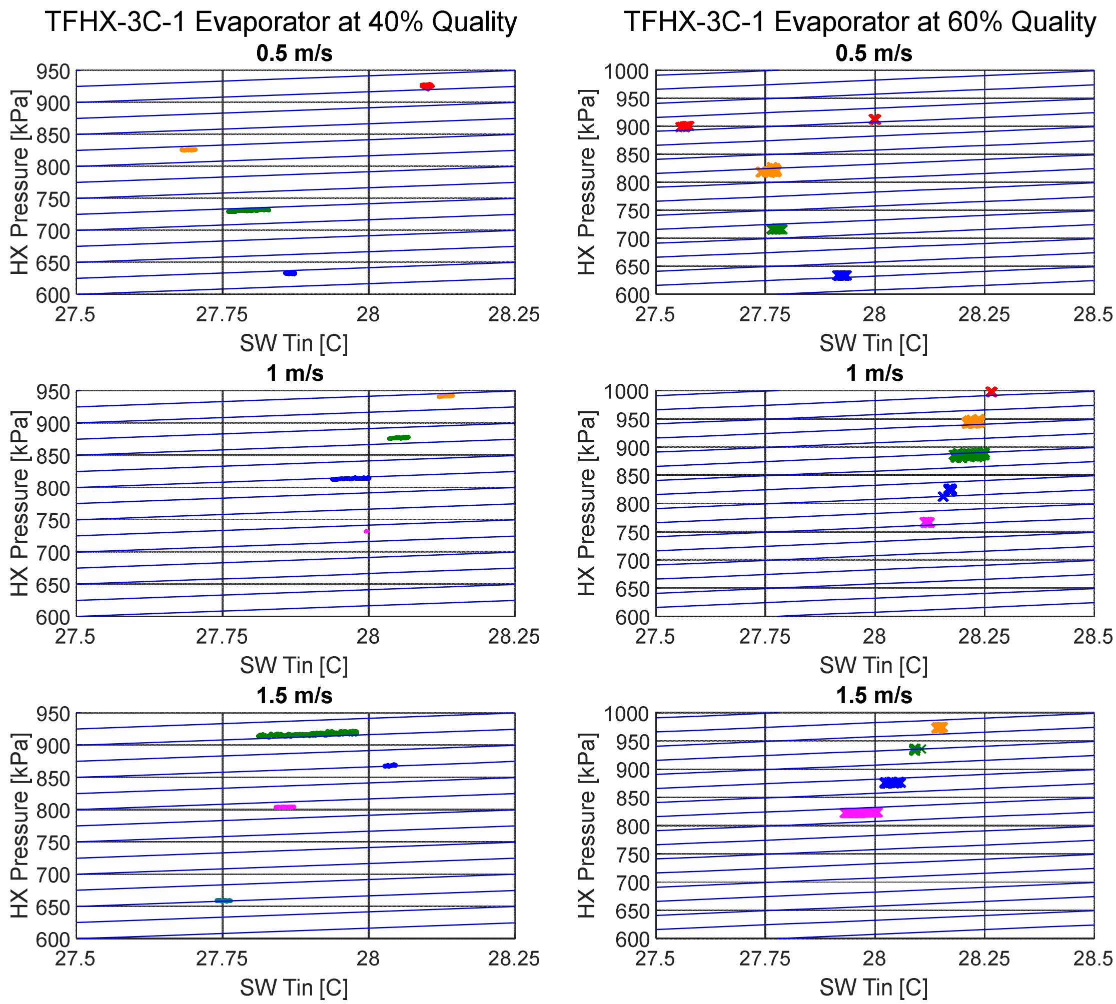
TFHX-3C-1 Evaporator at 40% Quality
TFHX-3C-1 Evaporator at 60% Quality
0.5 m/s
1 m/s
1.5 m/s
HX Pressure [kPa]
SW Tin [C]
600
650
700
750
800
850
900
950
1000
27.5
27.75
28
28.25
28.5

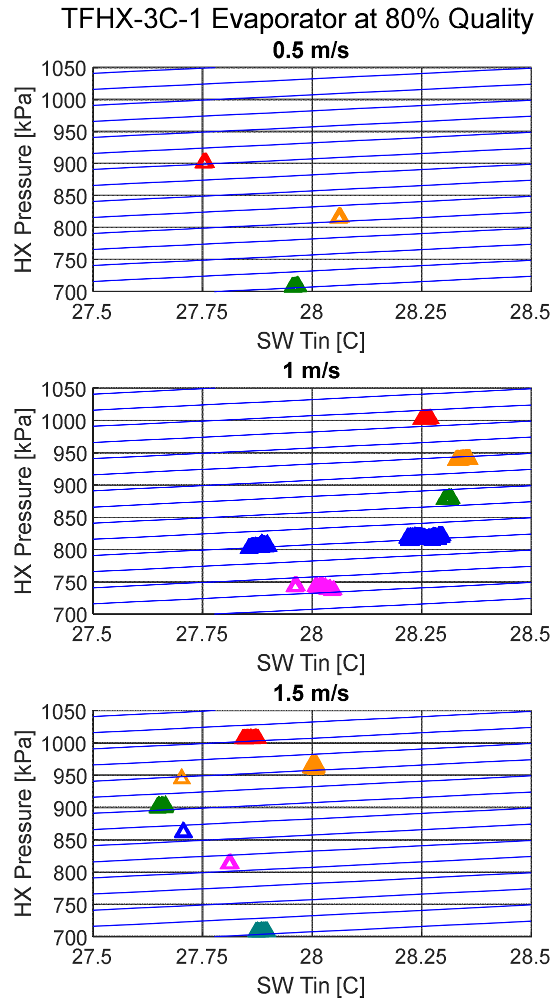

Figure 26. Evaporator pressure vs. seawater inlet temperature for different seawater and ammonia vapor flow rates. Marker colors: red = 2 g/s, orange = 2.67 g/s, green = 4 g/s, blue = 5.33 g/s, magenta = 6.67 kg/s, grey = 8 g/s, and teal = 10.67 g/s of ammonia vapor flow per plate. Blue lines indicate the ammonia saturation curve with offsets of 25 kPa.

The approach temperature is defined by the difference between the seawater inlet temperature and the ammonia saturation temperature corresponding to the heat exchanger operating pressure. A low approach temperature is more favorable. For a fixed seawater velocity, approach temperatures increase linearly with energy density. For the same energy density, increasing seawater velocity lowers the approach temperature.

The approach temperature combines individual the pressure vs seawater inlet temperatures graphs into one and, since the seawater temperatures varied during testing, provides a more direct comparison between operating points and heat exchangers.

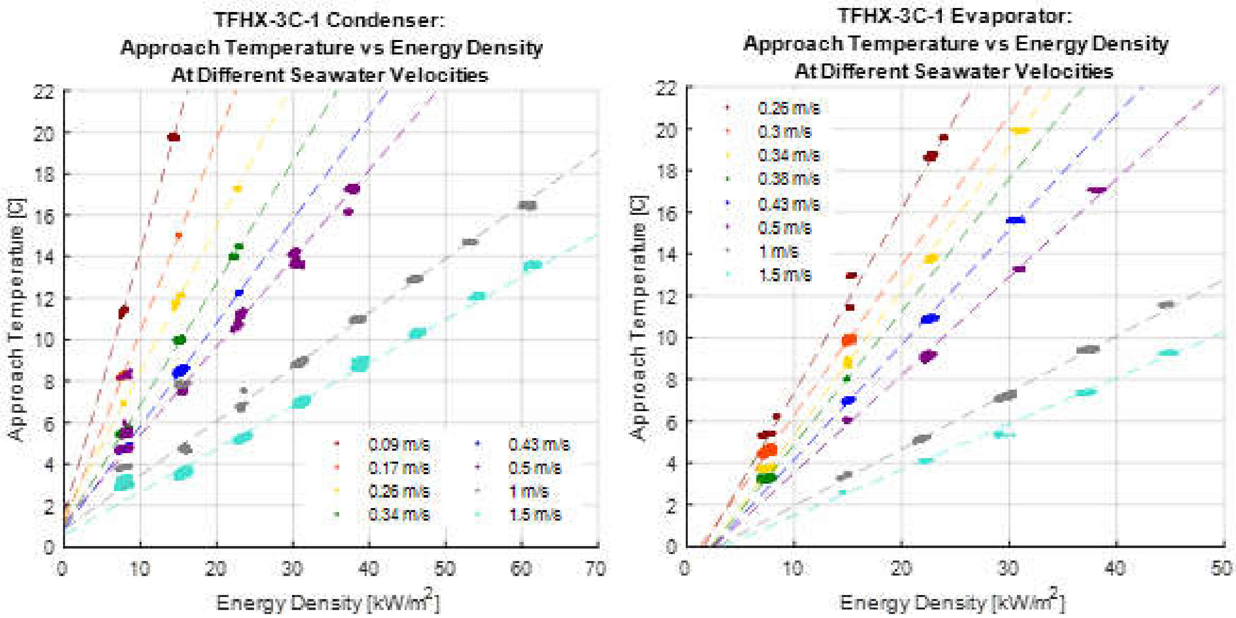

Figure 27. TFHX-3C-1 approach temperature vs energy density at different seawater velocities.

3.2.2. Overall Heat Transfer Coefficient

Only test points with less than 5°C of subcooling/superheating at the inlet were used in U-value calculations. This is because LMTD is calculated based on the saturation temperature at the measured inlet and outlet pressures. Heat exchanger pressure is mostly a function of seawater flow rate, seawater temperature, and ammonia vapor flow rate; therefore, the same LMTD would be calculated whether the inlet condition was saturated or subcooled. Because ammonia flow rate is fixed for a test point, a subcooled test point has a higher duty, and therefore, a higher U-value due to the way LMTD is calculated.

U-value is dependent on seawater flow rate, ammonia vapor flow rate, and quality. At the tested seawater velocities, U-value increased almost linearly with increasing seawater flow. Increasing seawater velocity resulted in a diminishing rate of increase in U-value, but the effect was not as drastic as previously observed logarithmic relationships. This is likely due to the tested seawater velocity range; the logarithmic relationship will likely be observed if higher seawater velocities were tested.

As a condenser, TFHX3C-1 had an increase in U-value with increasing ammonia vapor flow rate whereas U-value generally decreased with increasing ammonia vapor flow as an evaporator. U-value was comparable for 40% and 60% qualities but decreased slightly at 80% quality.

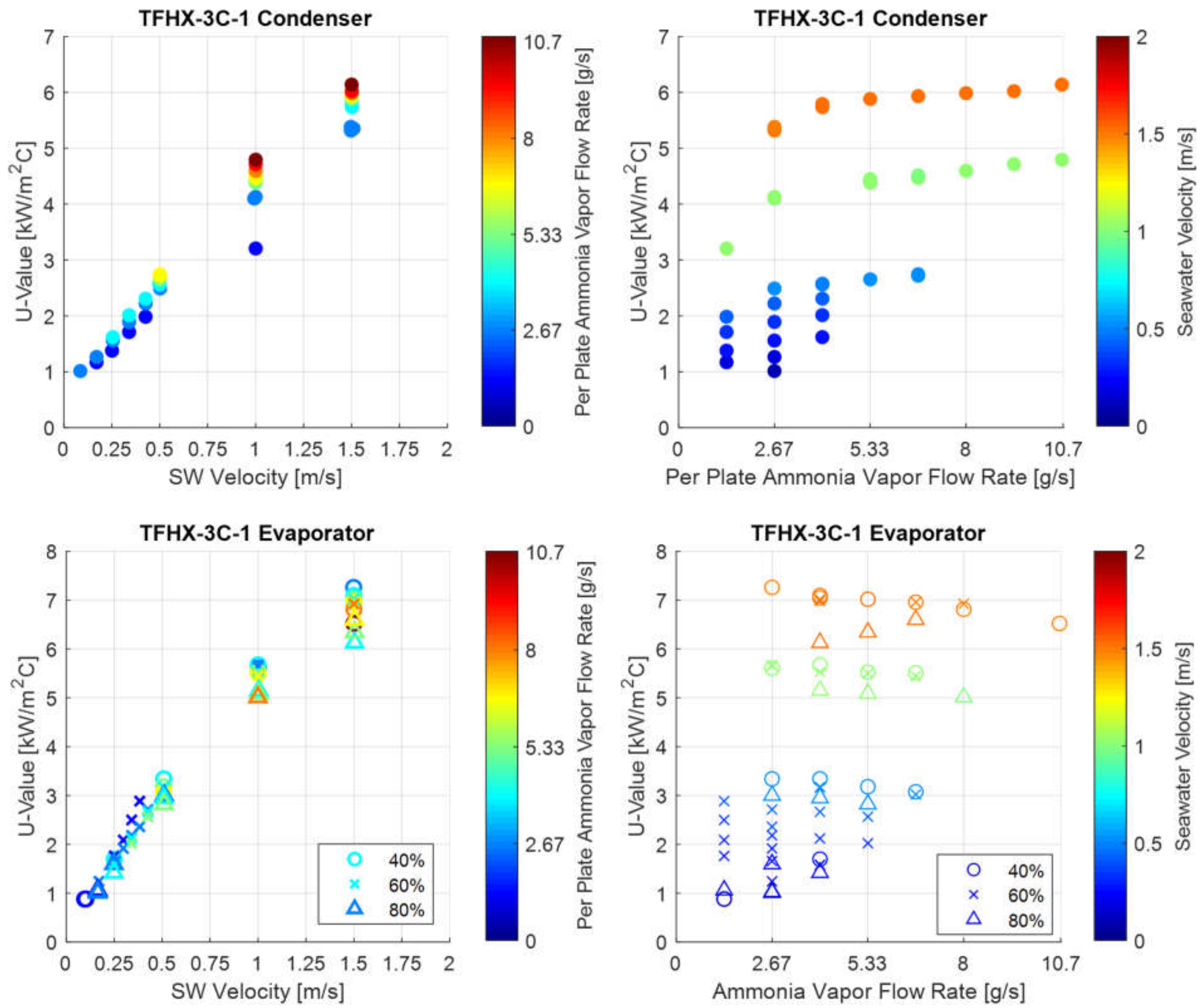

Figure 28. TFHX-3C-1 U-value vs seawater velocity and ammonia vapor flow rate.

3.2.3. Convective Heat Transfer Coefficients

Convective coefficients were calculated from all available data points using a constrained least-squares solver, where the lower bound for the convective coefficients is 0.

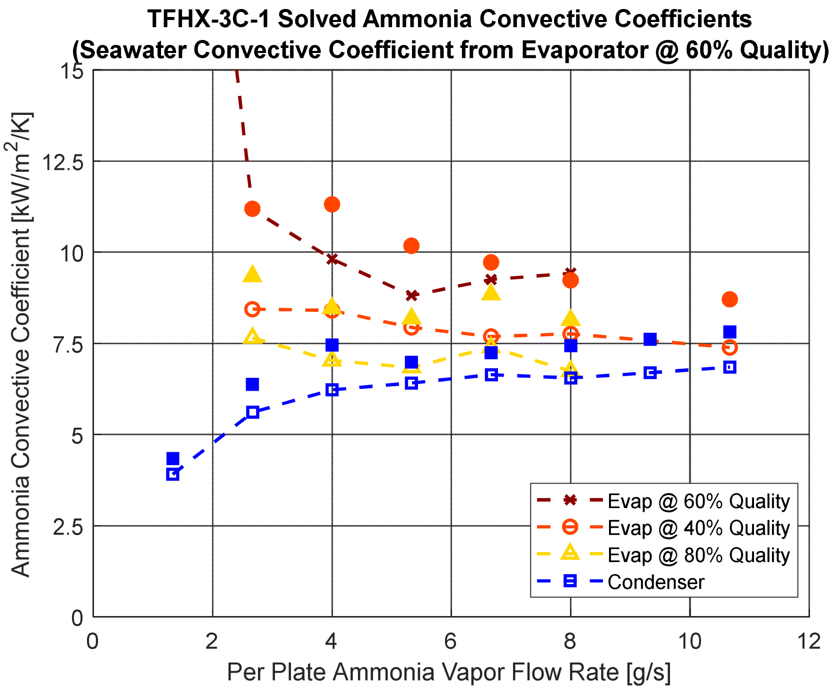

Figure 29. TFHX-3C-1 ammonia convective coefficients. The open circles represent the ammonia convective coefficient as solved using the constrained least-squares algorithm. The closed circles represent ammonia convective coefficients calculated by assuming the seawater convective coefficients are defined by a curve fitted to the seawater convective coefficients for the TFHX-3C-1 evaporator at 60% quality.

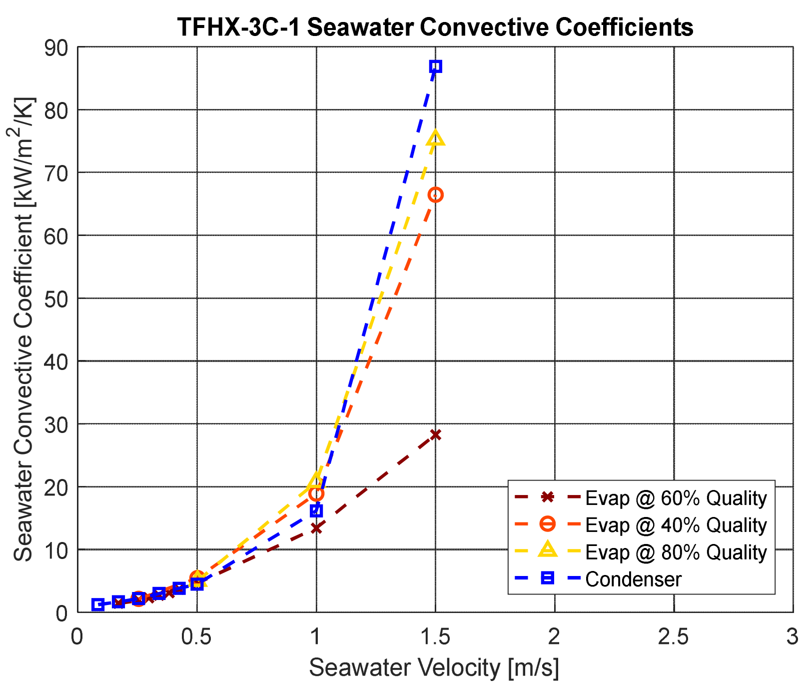

Figure 30. TFHX-3C-1 seawater convective coefficients.

Contrary to previously tested condensers, TFHX-3C-1's condensation coefficient increased with increasing vapor flow rate (Figure 29), indicating there may be a shear component at higher velocities, not just laminar falling film condensation. Similar to previously tested evaporators, TFHX-3C-1's boiling coefficient decreased with increasing ammonia flow rate.

With the exception of temperature related changes in seawater properties, the seawater convective coefficients should be similar whether TFHX-3C-1 is operating as a condenser or an evaporator. Furthermore, in evaporator mode, the seawater convective coefficient should be independent of the ammonia-side quality. The constrained least-squares solution provided similar seawater convective coefficients for all tested conditions up to seawater velocities of 1 m/s (Figure 30). At 1.5 m/s, the seawater convective coefficient for the evaporator at 60% quality was 2-3X lower than the other conditions tested.

When the seawater coefficients corresponding to the TFHX-3C-1 evaporator at 60% are applied to the condenser and evaporator at 40% and 80% quality test conditions, the ammonia convective coefficients can be solved for using the measured U-values, foil thickness, and titanium thermal conductivity. These ammonia convective coefficients are then averaged to determine the representative ammonia convective coefficient for a particular ammonia flow rate and result in averaged ammonia convective coefficients ~25% higher than determined from the constrained least-squares solution (Figure 29).

U values recalculated using the constrained least-squares solution convective coefficients were within 6% of the recorded U values. U values recalculated using the seawater convective coefficients at 60% quality and the averaged ammonia convective coefficients were within 12% of the recorded U values. Although the error is higher, the re-calculated convective coefficients are more in line with previously observed values and are more realistic. The few high ammonia flow rate points at lower seawater flow rates may have biased the constrained least squares solution.

3.3. TFHX-3C-2

TFHX-3C-2 consisted of 12 plates that had left and right manifolds. The six "right" oriented plates from TFHX-3C-1 were re-used. Testing was conducted at various seawater flow rates and ammonia (vapor) flow rates in both condenser and evaporator configurations (Table 6 and Table 7). For each test point, the expansion valve was maintained at 100% open and the ammonia vapor flow rate was controlled by controlling seawater flow through the companion heat exchanger.

3.3.1. Seawater Differential Pressure

Seawater-side pressure drop is related to the pumping power required to provide a certain seawater flow rate through the heat exchanger. The Darcy-Weisbach equation can be used to predict pressure drop as a function of the channel geometry and seawater velocity. The total seawater cross-sectional flow area is calculated from the effective seawater channel spacing (Table 2). The average seawater velocity is calculated from the measured seawater flow rate (in gpm) and the seawater cross-sectional flow area. The friction factor for smooth tubes, $f =$

$(0.79 \log Re - 1.64)^{-2}$, was used. Although the overall dP includes entrance and exit losses, adding minor loss coefficients for the entrance and exit losses overpredicted the pressure drop; no minor loss coefficients were applied. Seawater properties used in the calculations are summarized in Table 5. The predicted dP was within 1 kPa of the measured dP (Figure 23). The effect of the outer channels has been neglected in calculating the seawater cross sectional flow area. This approximation affects calculation of seawater velocity (and therefore, Reynolds number, friction factor, and the predicted dP).

Table 6. Overview of TFHX-3C-2 Condenser Test Points

			Ammonia Vapor Flow Rate [kg/s]					
Cold Seawater Flow Rate	[gpm]	[m/s]	0.016	0.024	0.032	0.048	0.064	0.08
	10.3	0.10	x					
	20.3	0.21	x	x				
	30.5	0.31	x	x	x			
	40.7	0.41	x	x	x			
	50.8	0.52	x	x	x			
	60.7	0.62	x	x	x	x		
	71	0.72	x	x	x	x		
	81.3	0.83	x	x	x	x		
	89.6	0.91			x	x		
	101.6	1.03		x	x	x	x	x
	111.7	1.14	x	x	x	x	x	
	127.1	1.29		x	x	x	x	x
	152.4	1.55		x	x	x	x	x
	172.7	1.76			x	x	x	x
	193	1.96			x	x	x	x
	213	2.17			x	x	x	x
	235	2.39			x	x	x	x
	254	2.58			x	x	x	x

Table 7. Overview of TFHX-3C-2 Evaporator Test Points

			Ammonia Vapor Flow Rate [kg/s] at 60% Quality					
Seawater Flow Rate	[gpm]	[m/s]	0.016	0.024	0.032	0.048	0.064	0.08
	10.1	0.10	x					
	20.3	0.20	x	x				
	30.4	0.30	x	x	x			
	40.7	0.40		x				
	50.8	0.50	x	x	x	x		
	61.0	0.60		x				
	71.1	0.70		x	x			
	81.3	0.80	x	x	x	x		
	91.5	0.90		x		x	x	
	101.6	1.00		x	x	x	x	
	111.8	1.10		x	x	x	x	x
	127.0	1.25		x	x	x	x	x
	152.4	1.50		x	x	x	x	x
	172.5	1.70			x	x	x	x
	193.6	1.91			x	x	x	x
	214.7	2.11			x	x	x	x
	233.7	2.30			x	x	x	x
	246.8	2.43			x	x	x	x

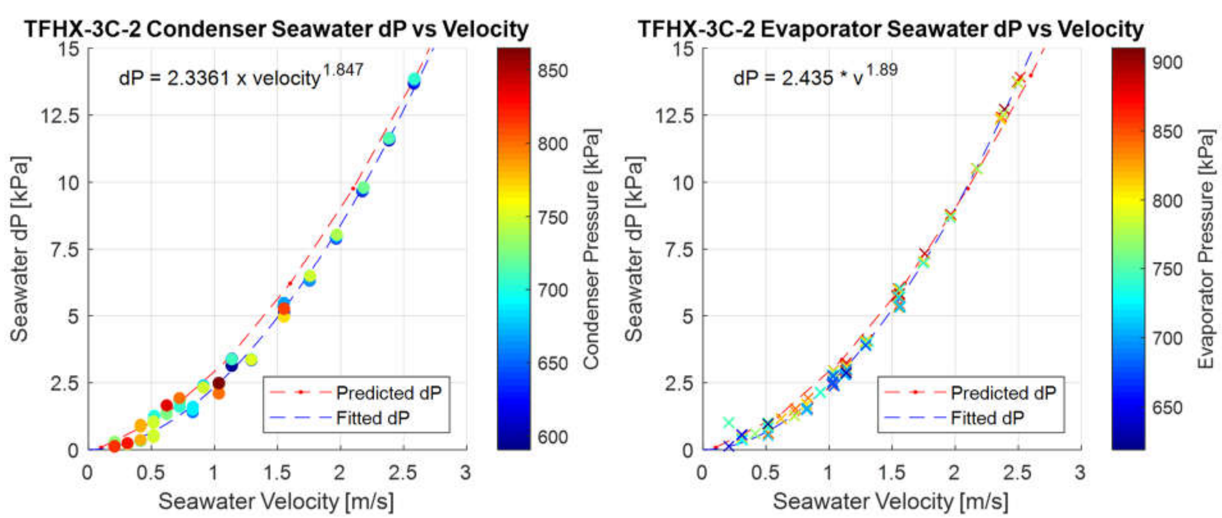

Figure 31. TFHX-3C-2 seawater pressure drop. Filled circles are data points; dotted lines represent predicted dP using the Darcy-Weisbach equation.

3.3.2. <u>Ammonia Differential Pressure</u>

Ammonia-side differential pressure is an important consideration for a heat exchanger. In a closed-cycle system, minimizing the pressure drop reduces the pumping power required to recirculate refrigerant and, in an OTEC system, increases the available differential pressure across a turbine. Ammonia pressure drop is strongly dependent on ammonia vapor flow rate, quality, and heat exchanger geometry.

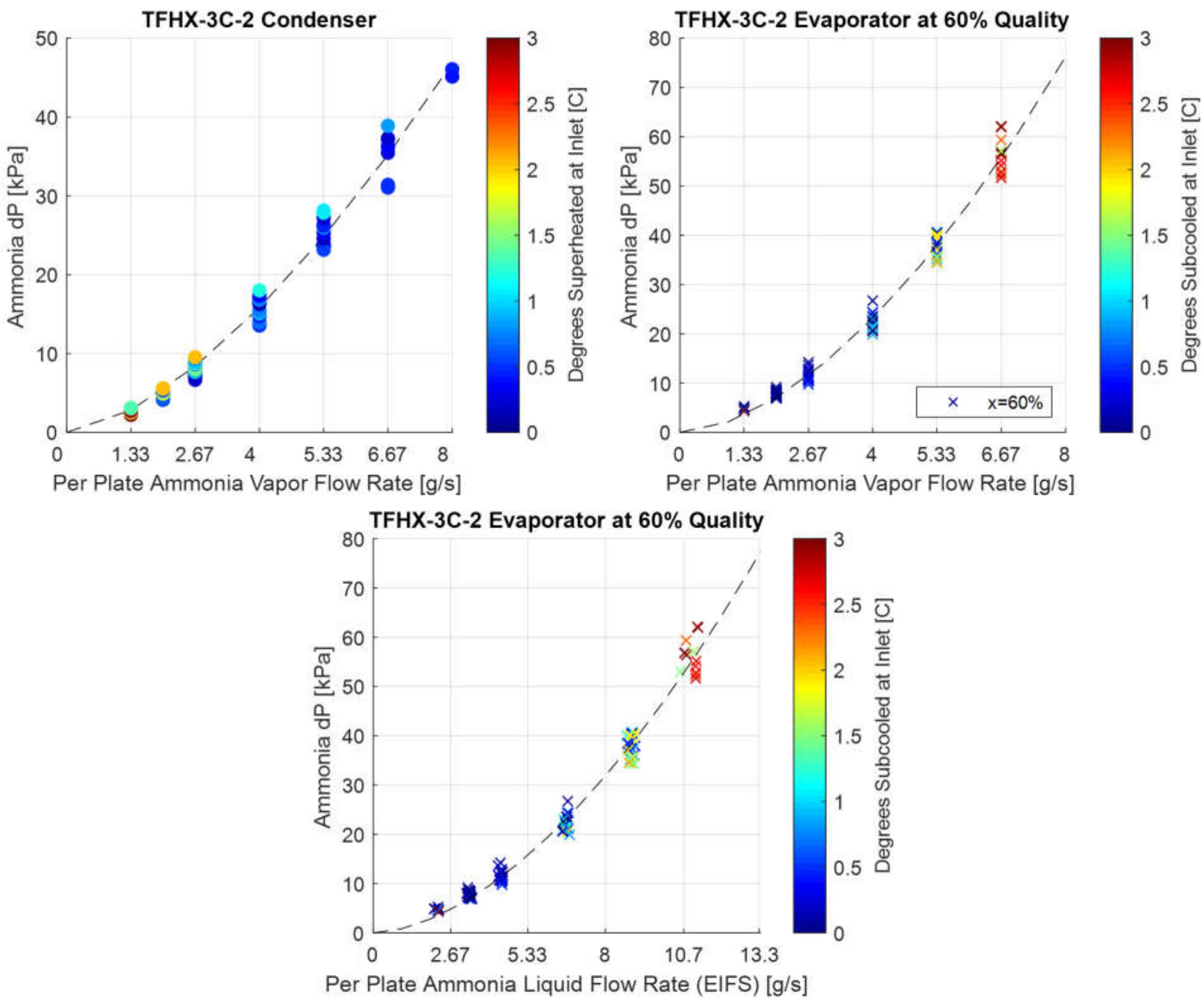

Figure 32. TFHX-3C-2 ammonia-side pressure drop vs ammonia flow rate.

3.3.3. Ammonia-side Operating Pressure

In general, pressure vs. seawater inlet temperature follow closely with the ammonia saturation curves.

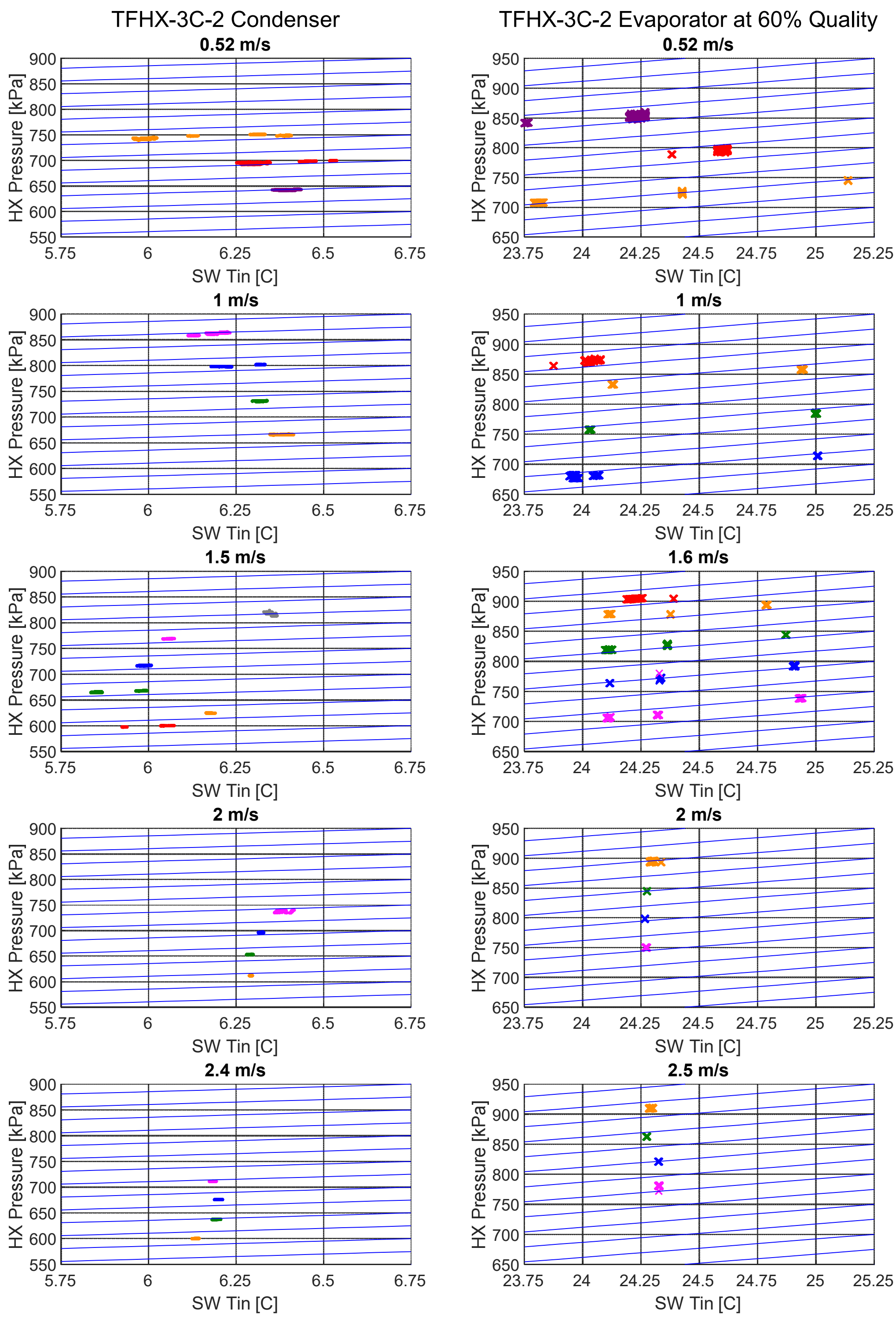

Figure 33. TFHX-3C-2 ammonia-side operating pressure vs seawater inlet temperature for different seawater and ammonia vapor flow rates. Marker colors: purple = 1.33 g/s, red = 2 g/s, orange = 2.67 g/s, green = 4 g/s, blue = 5.33 g/s, magenta = 6.67 kg/s, and grey = 8 g/s of ammonia vapor flow per plate. Blue lines indicate the ammonia saturation curve with offsets of 25 kPa.

The approach temperature is defined by the difference between the seawater inlet temperature and the ammonia saturation temperature corresponding to the heat exchanger operating pressure. A low approach temperature is more favorable. For a fixed seawater velocity, approach temperatures increase linearly with energy density. For the same energy density, increasing seawater velocity lowers the approach temperature.

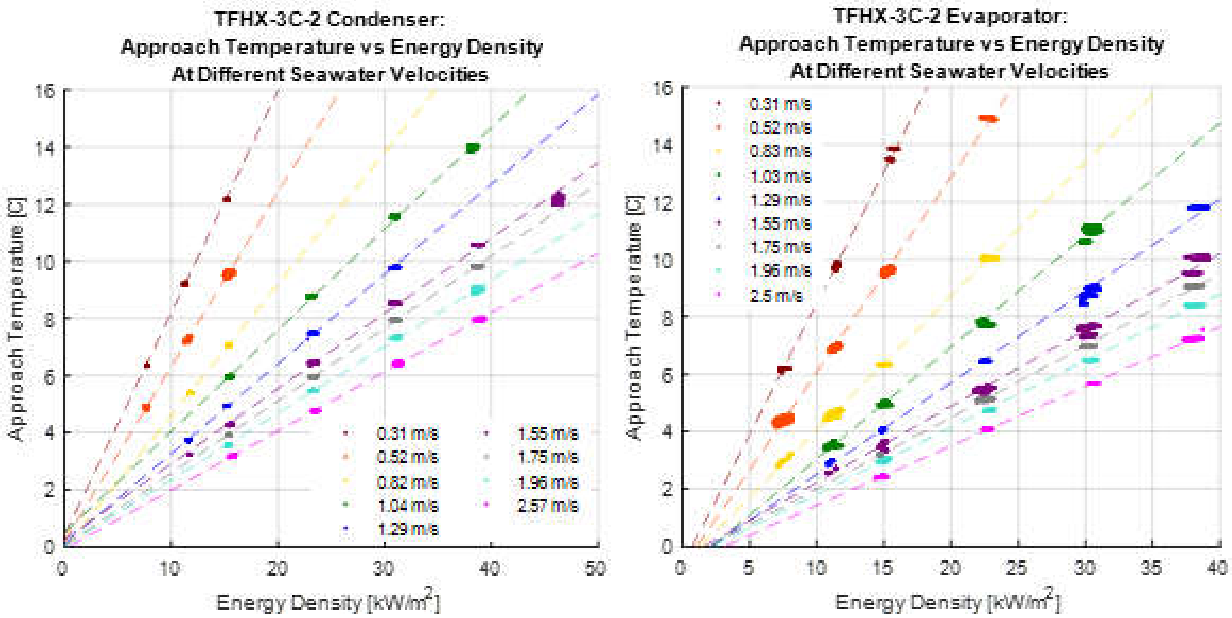

Figure 34. TFHX-3C-2 approach temperature vs energy density at different seawater velocities.

3.3.4. Overall Heat Transfer Coefficient

Only test points with less than 5°C of subcooling/superheating at the inlet were used in U-value calculations. This is because LMTD is calculated based on the saturation temperature at the measured inlet and outlet pressures. Heat exchanger pressure is mostly a function of seawater flow rate, seawater temperature, and ammonia vapor flow rate; therefore, the same LMTD would be calculated whether the inlet condition was saturated or subcooled. Because ammonia flow rate is fixed for a test point, a subcooled test point has a higher duty, and therefore, a higher U-value due to the way LMTD is calculated.

U-value is dependent on seawater flow rate, ammonia vapor flow rate, and quality. At the tested seawater velocities, U-value increased almost linearly with increasing seawater flow up to ~ 2 m/s. Above 2 m/s, increasing seawater velocity resulted in a diminishing rate of increase in U-value, but the effect was not as drastic as previously observed logarithmic relationships. As a condenser, TFHX-3C-2 had a slight increase in U-value with increasing ammonia vapor flow rate whereas U-value generally decreased with increasing ammonia vapor flow as an evaporator.

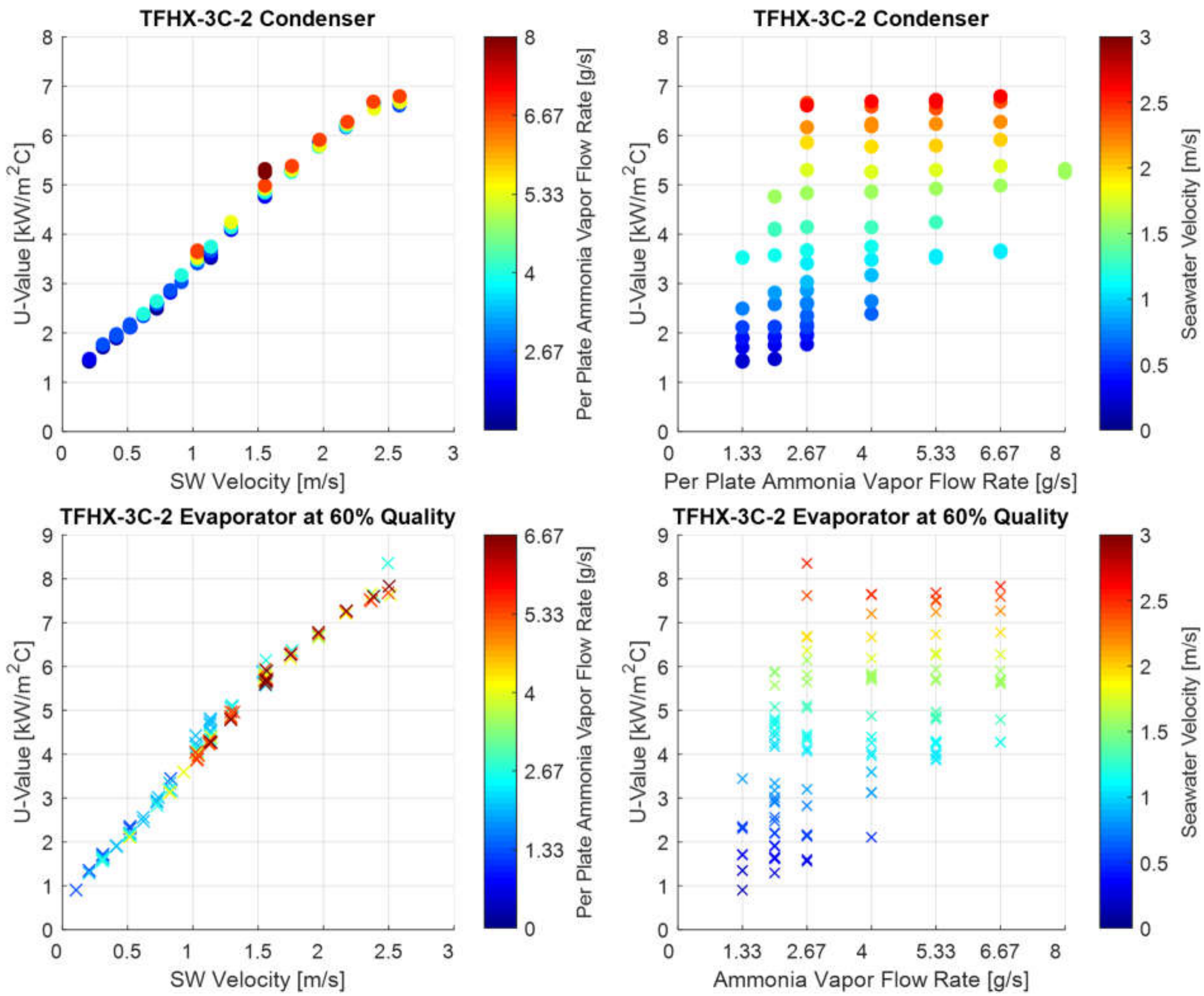

Figure 35. TFHX-3C-2 U-value vs seawater velocity and ammonia vapor flow rate.

3.3.5. Convective Heat Transfer Coefficients

Convective coefficients were calculated from all available data points using a constrained least-squares solver, where the lower bound for the convective coefficients is 0.

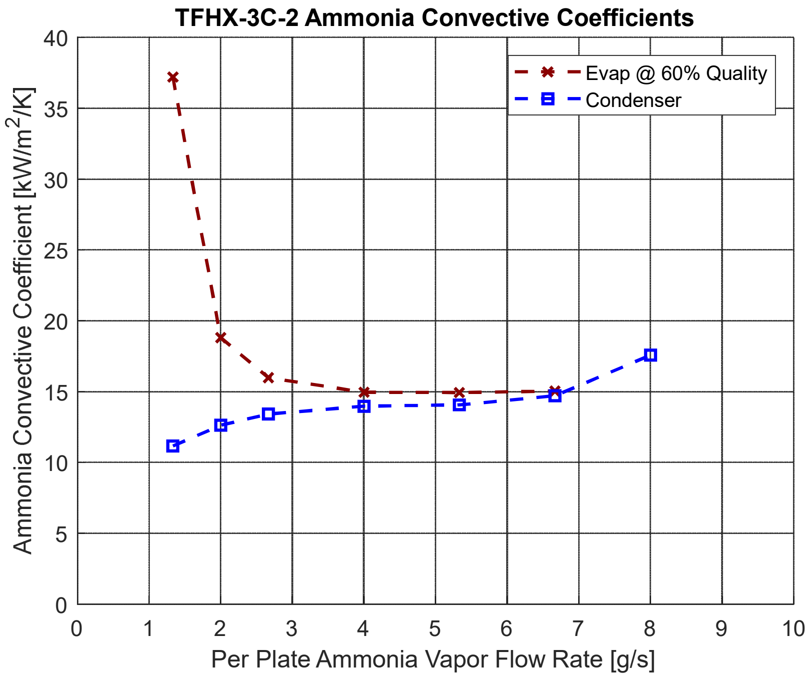

Figure 36. TFHX-3C-2 ammonia heat transfer coefficients.

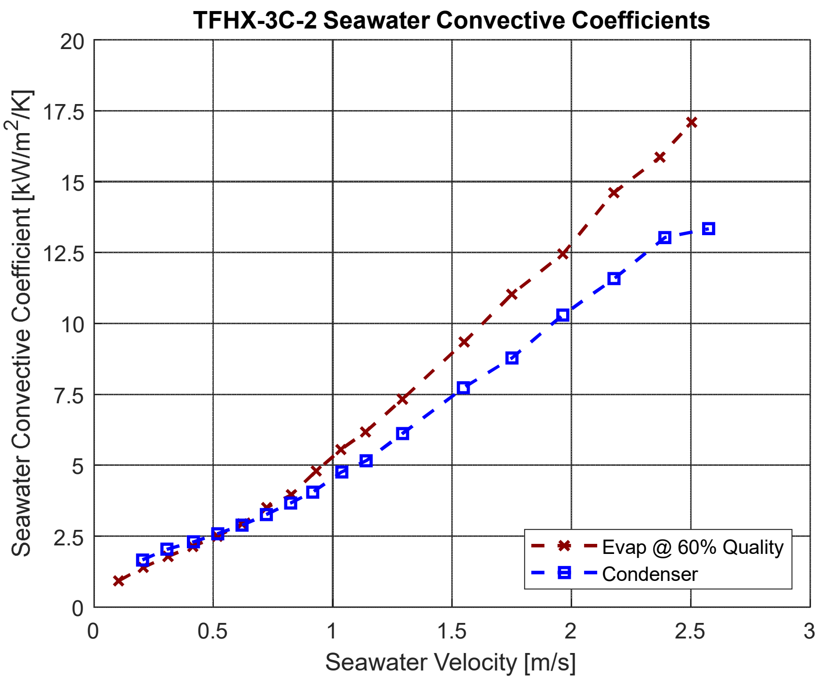

Figure 37. TFHX-3C-2 seawater convective coefficients.

The seawater convective coefficients show good agreement between condenser and evaporator test conditions. The ammonia convective coefficients follow the same trend as in TFHX-3C-1, increasing with increasing ammonia flow rate for the condenser and decreasing with increasing ammonia flow rate for the evaporator. U values recalculated using the convective coefficients were within +/- 6% of the observed U values.

3.4. TFHX-3C-3

TFHX-3C-3 consisted of 18 plates that had left, center, and right manifolds. The left and right oriented plates from TFHX-3C-2 were re-used.

Testing was conducted at various seawater flow rates and ammonia (vapor) flow rates in both condenser and evaporator configurations. During this testing, it was difficult to maintain ammonia flow rates using only the seawater control valves. In order to obtain stable data sets, the targeted ammonia flow rate was roughly attained by controlling seawater flow through the companion heat exchanger and the expansion valve was used to maintain the flow rate. This resulted in some test points having high superheat/subcooling but the ability to obtain stable data sets over a wide range of test points was more valuable.

Table 8. TFHX-3C-3 condenser test points.

			Ammonia Vapor Flow Rate [kg/s]				
Cold Seawater Flow Rate	gpm	[m/s]	0.024	0.036	0.048	0.072	0.096
	23.7	0.30	x	x			
	39.5	0.50	x	x	x		
	59.3	0.75	x	x	x		
	79	1.00	x	x	x	x	
	98.8	1.25	x	x	x	x	
	118.5	1.50	x	x	x	x	x
	158	2.00	x	x	x	x	x
	177.8	2.25	x	x	x	x	x
	197.5	2.50	x	x	x	x	x
	217.3	2.75				x	x

3.4.1. Seawater Differential Pressure

Seawater-side pressure drop is related to the pumping power required to provide a certain seawater flow rate through the heat exchanger. The Darcy-Weisbach equation can be used to predict pressure drop as a function of the channel geometry and seawater velocity. The total seawater cross-sectional flow area is calculated from the effective seawater channel spacing (Table 2). The average seawater velocity is calculated from the measured seawater flow rate (in gpm) and the seawater cross-sectional flow area. The friction factor for smooth tubes, $f = (0.79 \log Re - 1.64)^{-2}$, was used. Although the overall dP includes entrance and exit losses, adding minor loss coefficients for the entrance and exit losses overpredicted the pressure drop; no minor loss coefficients were applied. Seawater properties used in the calculations are summarized in Table 5. The predicted dP was within 5 kPa of the measured dP (Figure 38). The effect of the outer channels has been neglected in calculating the seawater cross sectional flow area. This approximation affects calculation of seawater velocity (and therefore, Reynolds number, friction factor, and the predicted dP).

Table 9. TFHX-3C-3 evaporator test points.

			Ammonia Vapor Flow Rate [kg/s]			
Warm Seawater Flow Rate	**gpm**	**[m/s]**	**0.024**	**0.036**	**0.048**	**0.072**
	23.7	0.30	x			
	39.5	0.50	x	x	x	
	59.3	0.75		x	x	
	79	1.01	x	x	x	x
	98.8	1.25	x	x	x	x
	118.5	1.50	x	x	x	x
	138.3	1.75	x	x	x	x
	158	2.00	x	x	x	x
	177.8	2.25		x	x	x
	197.5	2.50	x	x	x	x

* Evaporator testing was conducted at 40%, 60%, and 80% quality. Not every test point was tested for each quality.

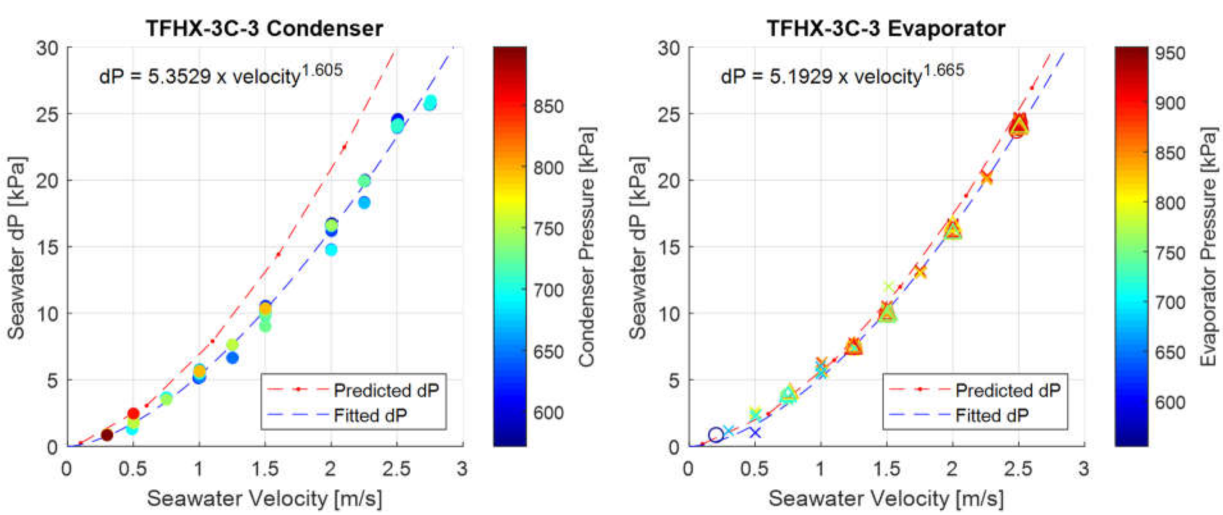

Figure 38. TFHX-3C-3 seawater pressure drop. Symbols are data points; dotted lines represent predicted dP using the Darcy-Weisbach equation.

3.4.2. Ammonia Differential Pressure

Ammonia-side differential pressure is an important consideration for a heat exchanger. In a closed-cycle system, minimizing the pressure drop reduces the pumping power required to recirculate refrigerant and, in an OTEC system, increases the available differential pressure across a turbine. Ammonia pressure drop is strongly dependent on ammonia vapor flow rate, quality, and heat exchanger geometry.

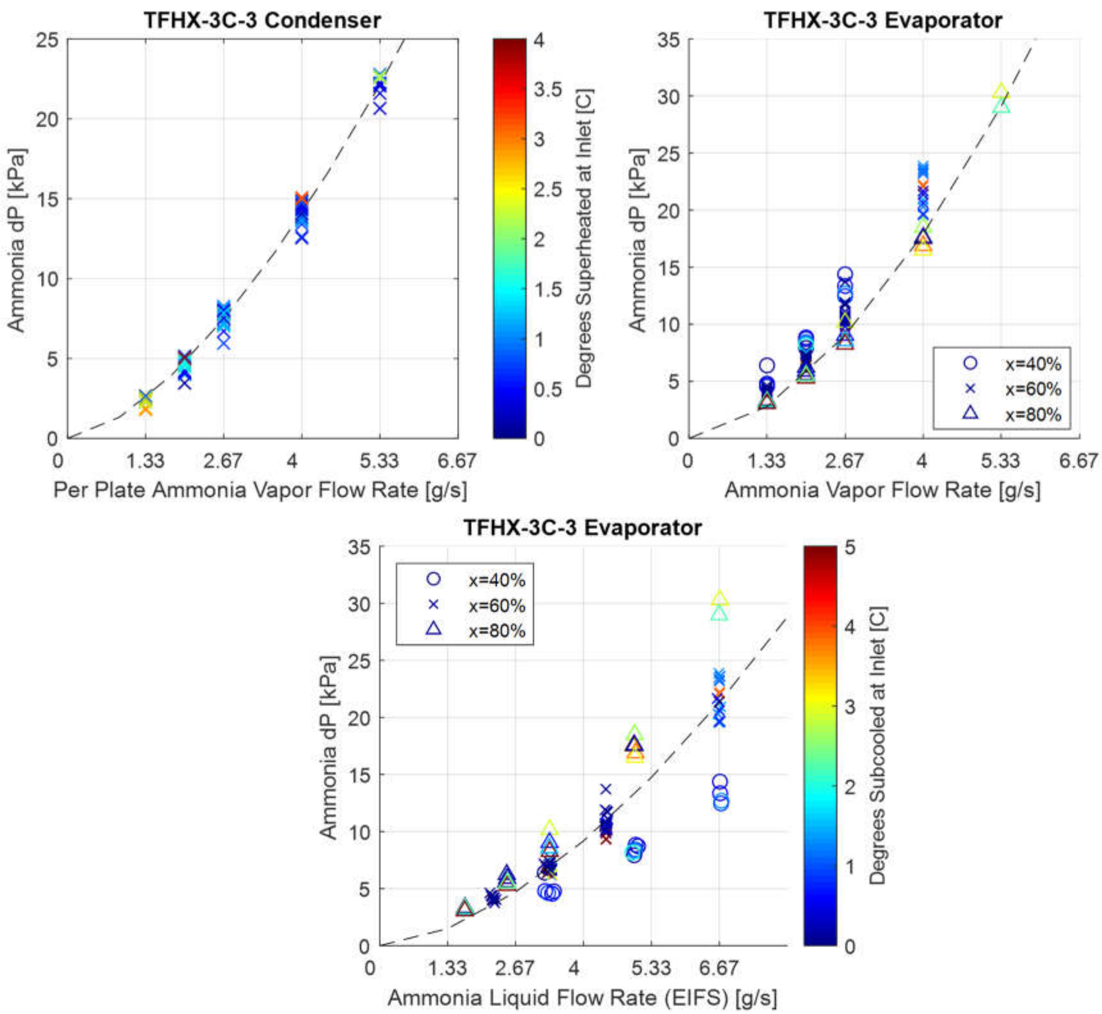

Figure 39. TFHX-3C-3 ammonia-side pressure drop vs ammonia flow rate.

3.4.3. Ammonia-side Operating Pressure

Heat exchanger pressure is determined by the seawater temperature, seawater flow rate, ammonia vapor flow rate, quality (for an evaporator), and degree of subcooling/superheating. For a fixed seawater and ammonia flow rate and quality, heat exchanger pressure should only depend on seawater inlet temperature and is expected to follow the slope of the ammonia saturation curve.

In general, pressure vs. seawater inlet temperature follow closely with the ammonia saturation curves. Discrepancies were attributed to variations in seawater and ammonia flow rate (both vapor and liquid). The lack of sensitivity and hysteresis in the seawater control valves made it difficult to hold a fixed seawater and ammonia vapor flow rate. For some data points, the expansion valve was used to control the ammonia vapor flow rate. The valve position and movement also affected heat exchanger pressure.

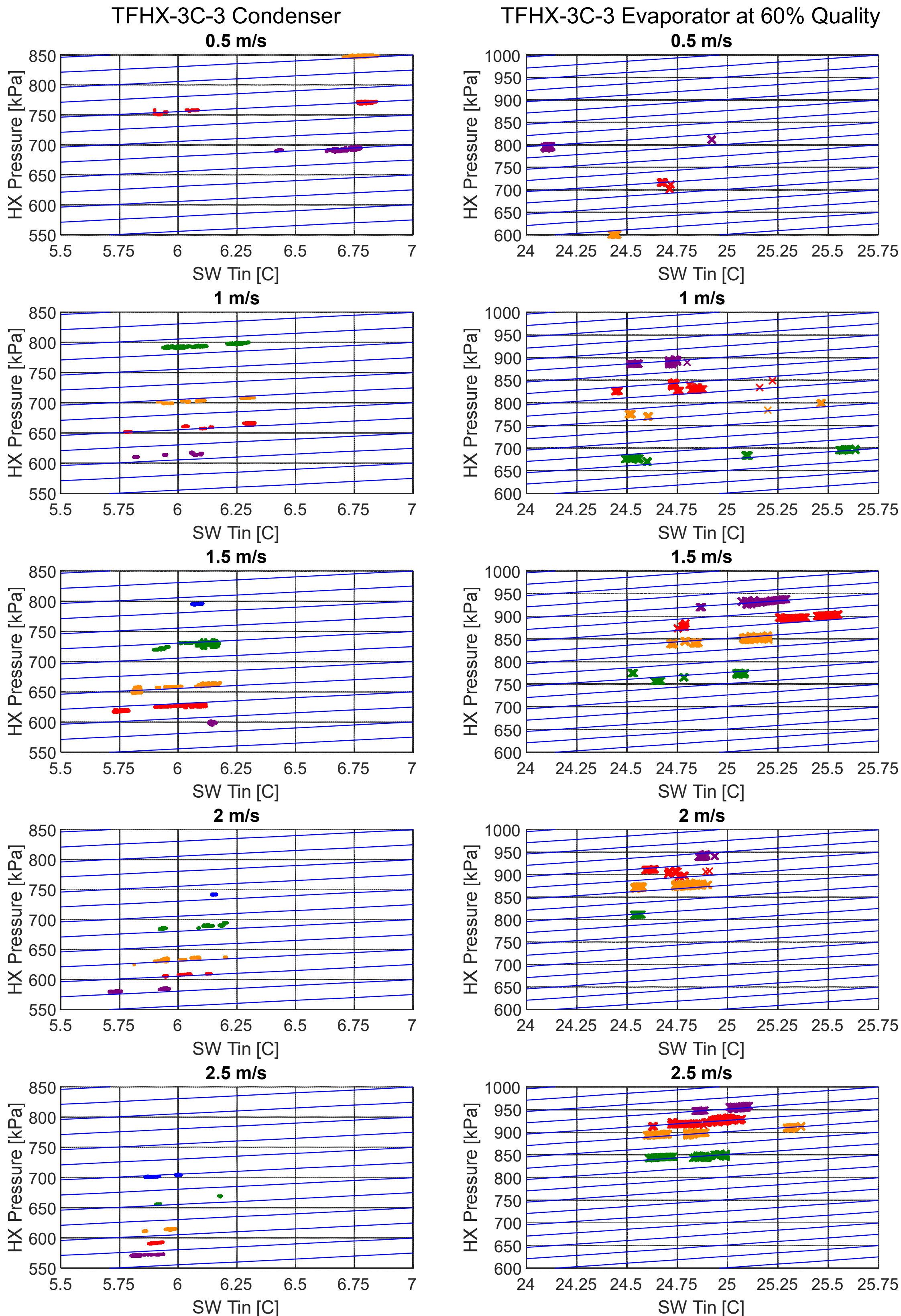
TFHX-3C-3 Condenser
TFHX-3C-3 Evaporator at 60% Quality
0.5 m/s
1 m/s
1.5 m/s
2 m/s
2.5 m/s
HX Pressure [kPa]
SW Tin [C]

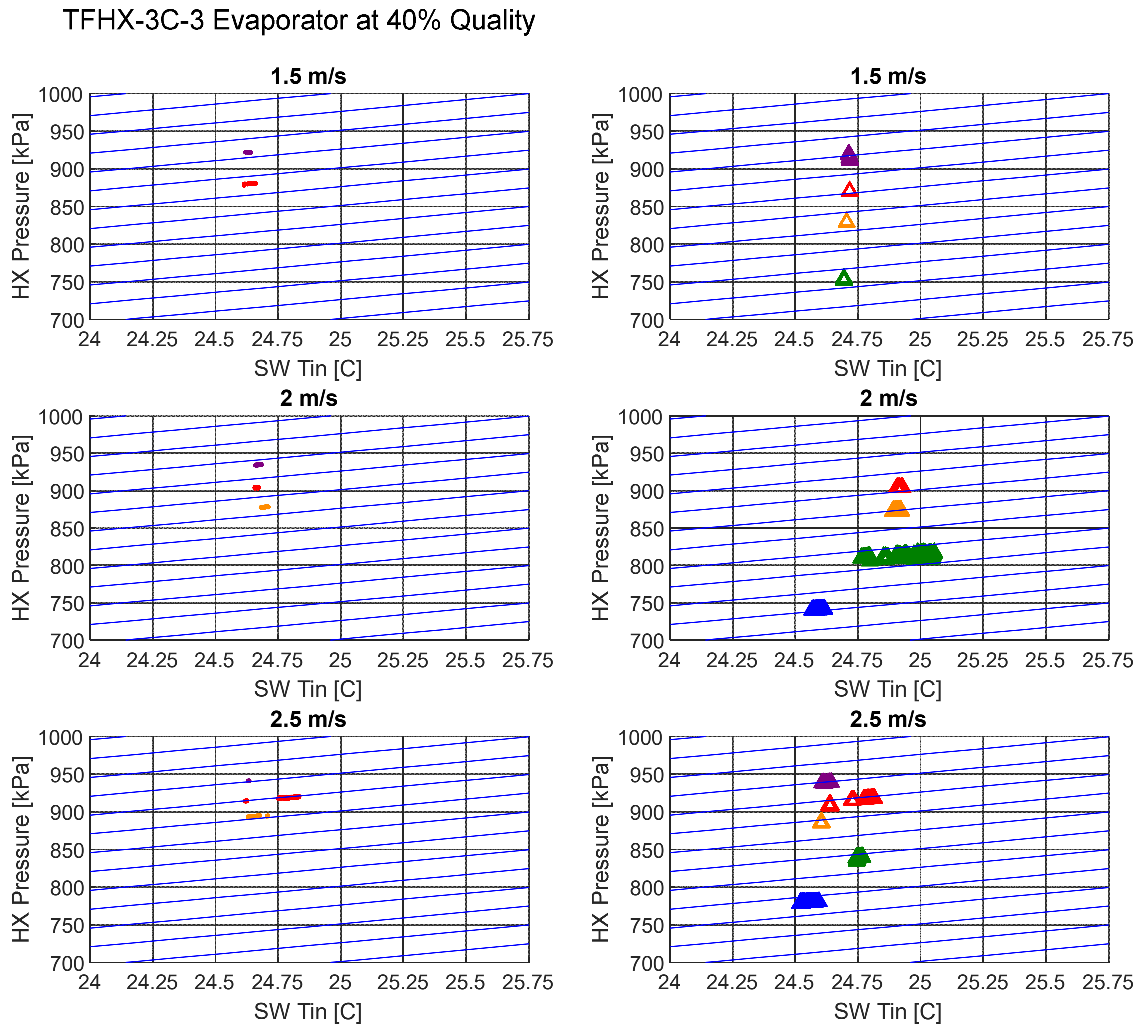

Figure 40. TFHX-3C-3 ammonia-side operating pressure vs seawater inlet temperature for different seawater and per plate ammonia vapor flow rates. Marker colors: purple = 1.33 g/s, red = 2 g/s, orange = 2.67 g/s, green = 4 g/s, blue = 5.33 g/s of ammonia vapor flow per plate. Blue lines indicate the ammonia saturation curve with offsets of 25 kPa.

The approach temperature is defined by the difference between the seawater inlet temperature and the ammonia saturation temperature corresponding to the heat exchanger operating pressure. A low approach temperature is more favorable. For a fixed seawater velocity, approach temperatures increase linearly with energy density. For the same energy density, increasing seawater velocity lowers the approach temperature.

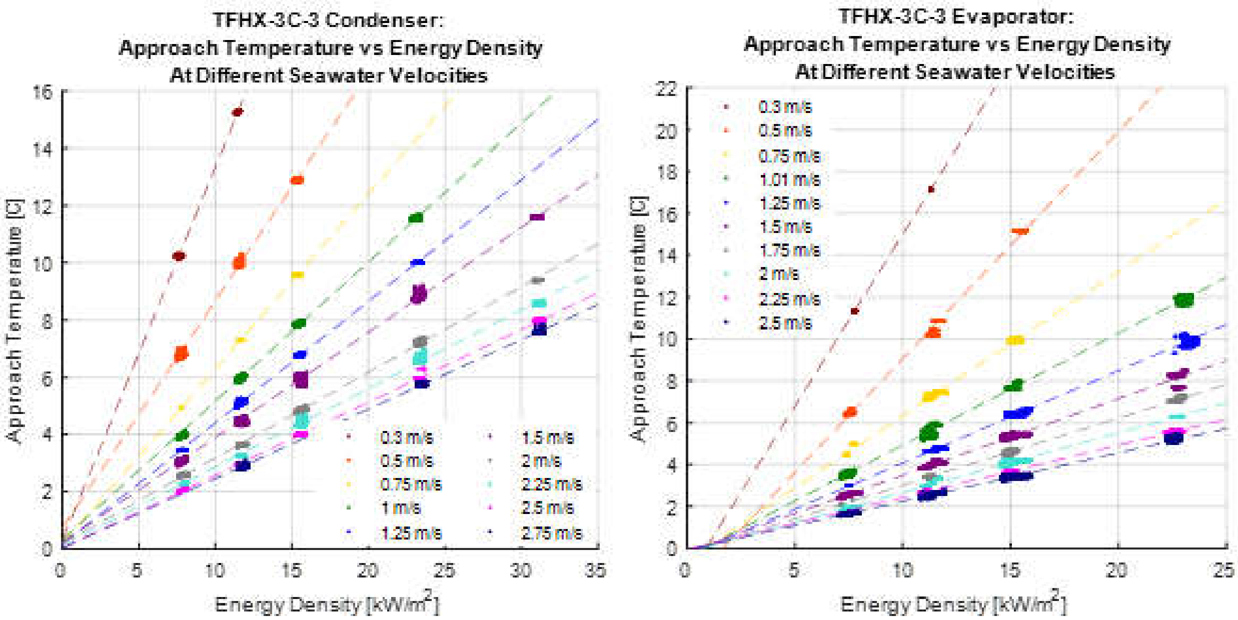

Figure 41. TFHX-3C-3 approach temperature vs energy density for different seawater velocities.

3.4.4. <u>Overall Heat Transfer Coefficient</u>

Due to the use of the expansion valve to control flow rate, test points with up to 10°C of subcooling/superheating at the inlet were used in U-value calculations. In order to calculate convective coefficients, it was more important to obtain U-values over a range of seawater and ammonia flow rates than a limited set of U-values taken at saturated conditions.

U-value is dependent on seawater flow rate, ammonia vapor flow rate, and quality. At the tested seawater velocities, U-value increased almost linearly with increasing seawater flow. Increasing seawater velocity resulted in a diminishing rate of increase in U-value, but the effect was not as drastic as previously observed logarithmic relationships. This is likely due to the tested seawater velocity range; the logarithmic relationship will likely be observed if higher seawater velocities were tested.

U-value increased slightly with increasing ammonia vapor flow rate as a condenser and decreased with increasing ammonia vapor flow as an evaporator. U-value was comparable for 40% and 60% qualities but slightly lower at 80% quality.

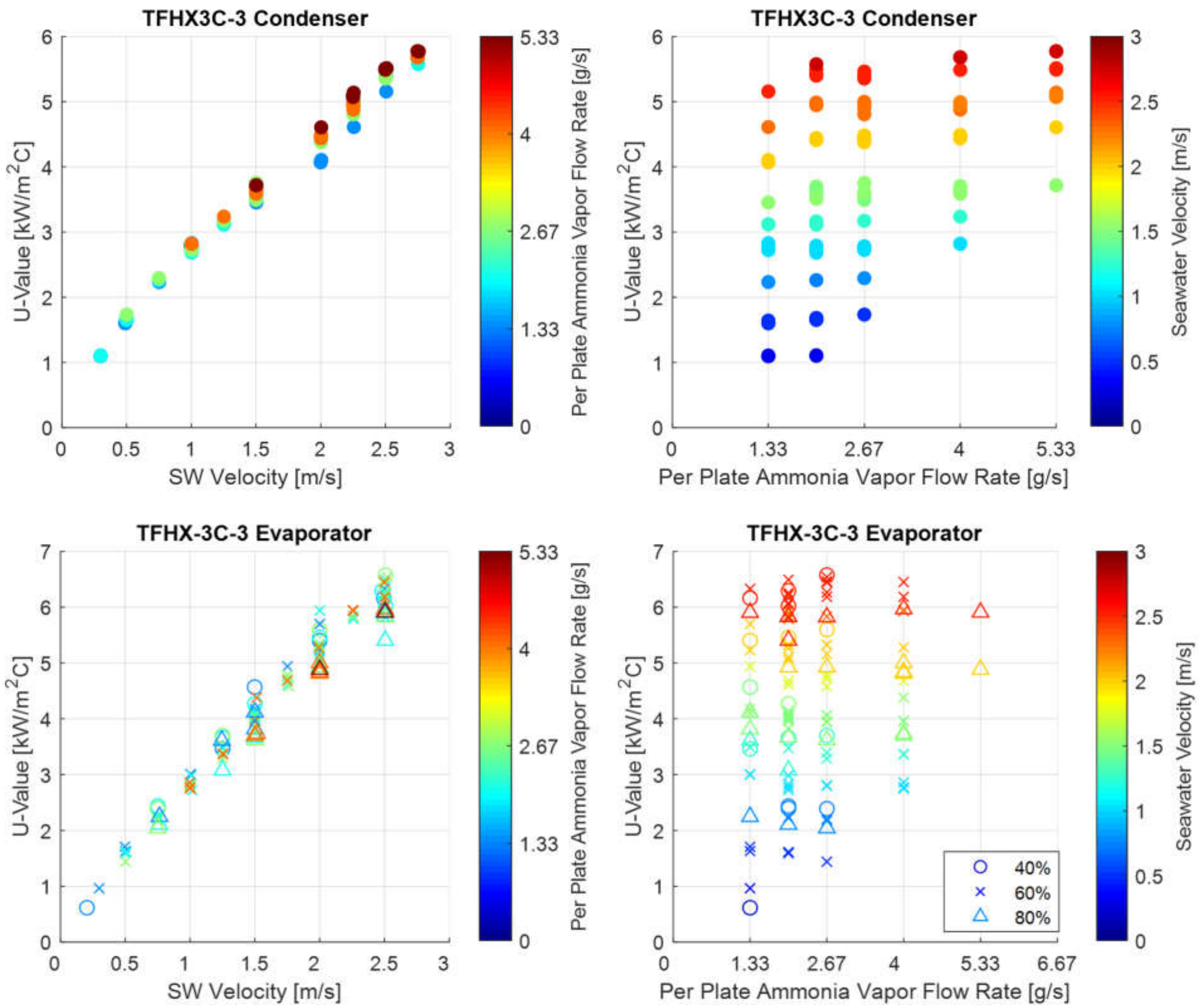

Figure 42. TFHX-3C-2 U-value vs seawater velocity and ammonia vapor flow rate.

3.4.5. Convective Coefficient

Convective coefficients were calculated from all available data points using a constrained least-squares solver, where the lower bound for the convective coefficients is 0.

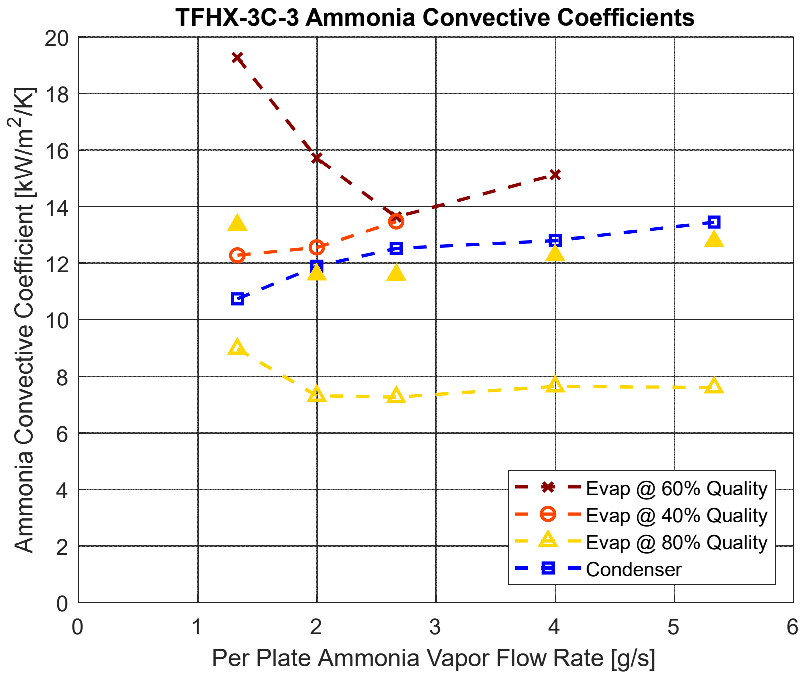

Figure 43. TFHX-3C-3 ammonia convective coefficients. The solid triangles represent ammonia convective coefficients for the evaporator at 80% quality calculated using seawater convective coefficients for the evaporator at 60% quality.

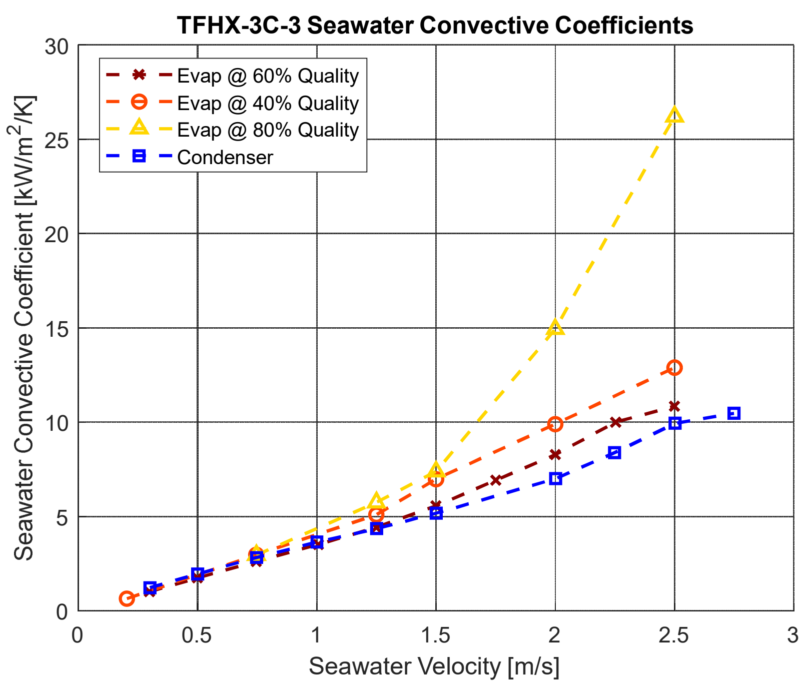

Figure 44. TFHX-3C-3 seawater convective coefficients.

Except for the evaporator at 80% quality above 1.5 m/s, the seawater convective coefficients show good agreement for all condenser and evaporator test conditions. The ammonia convective coefficients follow the same trend as in TFHX-3C-1, increasing with increasing ammonia flow rate for the condenser. However, there is no clear trend for the ammonia convective coefficient with ammonia flow rate for the evaporator.

U values recalculated using the convective coefficients were within +/- 11% of the observed U values. When the seawater convective coefficients for the evaporator at 60% quality were used to find the ammonia convective coefficients at 80% quality, the error in the re-calculated U values reduced from 11% to 6.9% even though the sum of the square of the errors was higher.

3.5. TFHX-3E-INT-1

TFHX-3E-INT1 consisted of 12 interlocking plates. Testing was conducted at various seawater flow rates and ammonia (vapor) flow rates in both condenser and evaporator configurations. Unlike previous testing, the ammonia flow rate was not preset. Instead, for each seawater flow rate through the TFHX, seawater flow through the companion heat exchanger was adjusted to get a range of ammonia flow rates. Although ammonia flow rates will not be precisely matched between seawater flow rates, each data point will be more stable and U values can be interpolated in calculations to obtain convective coefficients.

Table 10. TFHX-3E-INT1 condenser test points.

SW Flow Rate [gpm]	SW Velocity [m/s]	CIFS Range [kg/s]	
6.6	0.3	0.006	0.016
13.3	0.65	0.0078	0.0309
20	0.99	0.008	0.0387
25	1.24	0.0215	0.0346
26	1.29	0.0079	0.0452
31	1.54	0.0087	0.0492
41	2.04	0.0084	0.055
51	2.53	0.0319	0.0582

Table 11. TFHX-3E-INT1 evaporator test points.

SW Flow Rate [gpm]	SW Velocity [m/s]	CIFS Range [kg/s]*	
5	0.25	0.005	0.0189
10	0.50	0.0046	0.0303
15	0.74	0.0064	0.0382
20	0.99	0.0044	0.0462
30	1.49	0.0058	0.0575
40	1.99	0.006	0.0681
50	2.48	0.0045	0.0776

* Evaporator quality was not controlled.

3.5.1. Seawater Differential Pressure

Seawater-side pressure drop is related to the pumping power required to provide a certain seawater flow rate through the heat exchanger. The Darcy-Weisbach equation can be used to predict pressure drop as a function of the channel geometry and seawater velocity. The total seawater cross-sectional flow area is calculated from the effective seawater channel spacing (Table 2). The average seawater velocity is calculated from the measured seawater flow rate (in gpm) and the seawater cross-sectional flow area. The friction factor was found using $f = \frac{64}{Re}$ for Re < 1000 and the friction factor for smooth tubes, $f = (0.79 \log Re - 1.64)^{-2}$, was used for Re > 1000. Minor loss coefficients of 1 were applied for entrance and exit losses. Seawater properties used in the calculations are summarized in Table 12. The predicted dP was within 10 kPa of the measured dP (Figure 45).

Table 12. Seawater properties

	Cold Seawater	Warm Seawater
Temperature	7°C	27.5°C
Density	1027.2 kg/m^3	1022.1 kg/m^3
Kinematic Viscosity	1.48x10^{-6} m^2/s	8.87x10^{-7} m^2/s

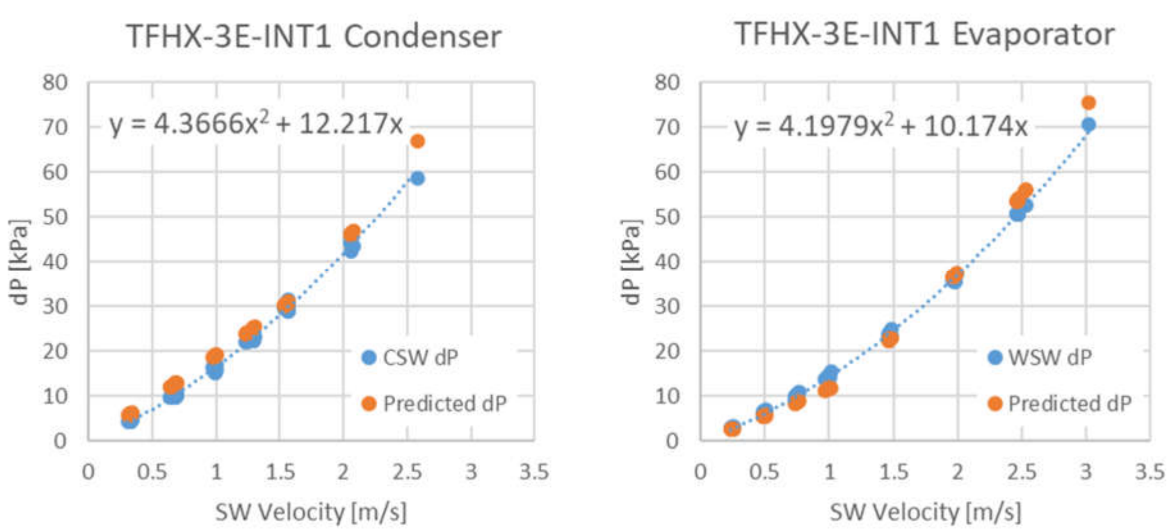

Figure 45. TFHX-3E-INT1 seawater pressure drop.

3.5.2. Ammonia Differential Pressure

Ammonia-side differential pressure is an important consideration for a heat exchanger. In a closed-cycle system, minimizing the pressure drop reduces the pumping power required to recirculate refrigerant and, in an OTEC system, increases the available differential pressure across a turbine. For the condenser, ammonia pressure drop is strongly dependent on ammonia vapor flow rate.

For the evaporator, ammonia pressure drop is strongly dependent on ammonia vapor flow rate and ammonia liquid flow rate. In this set of testing, the liquid ammonia flow rate, not quality was controlled. Depending on the ammonia vapor flow rate, the quality varied from 2.5-70%. When grouped by quality, ammonia pressure drop did not show correlation with energy density, whereas when grouped by liquid flow rate, the pressure drop strongly depended on energy density. This implies that at high ammonia liquid flow rates, a portion of the pressure drop is likely attributed to static head.

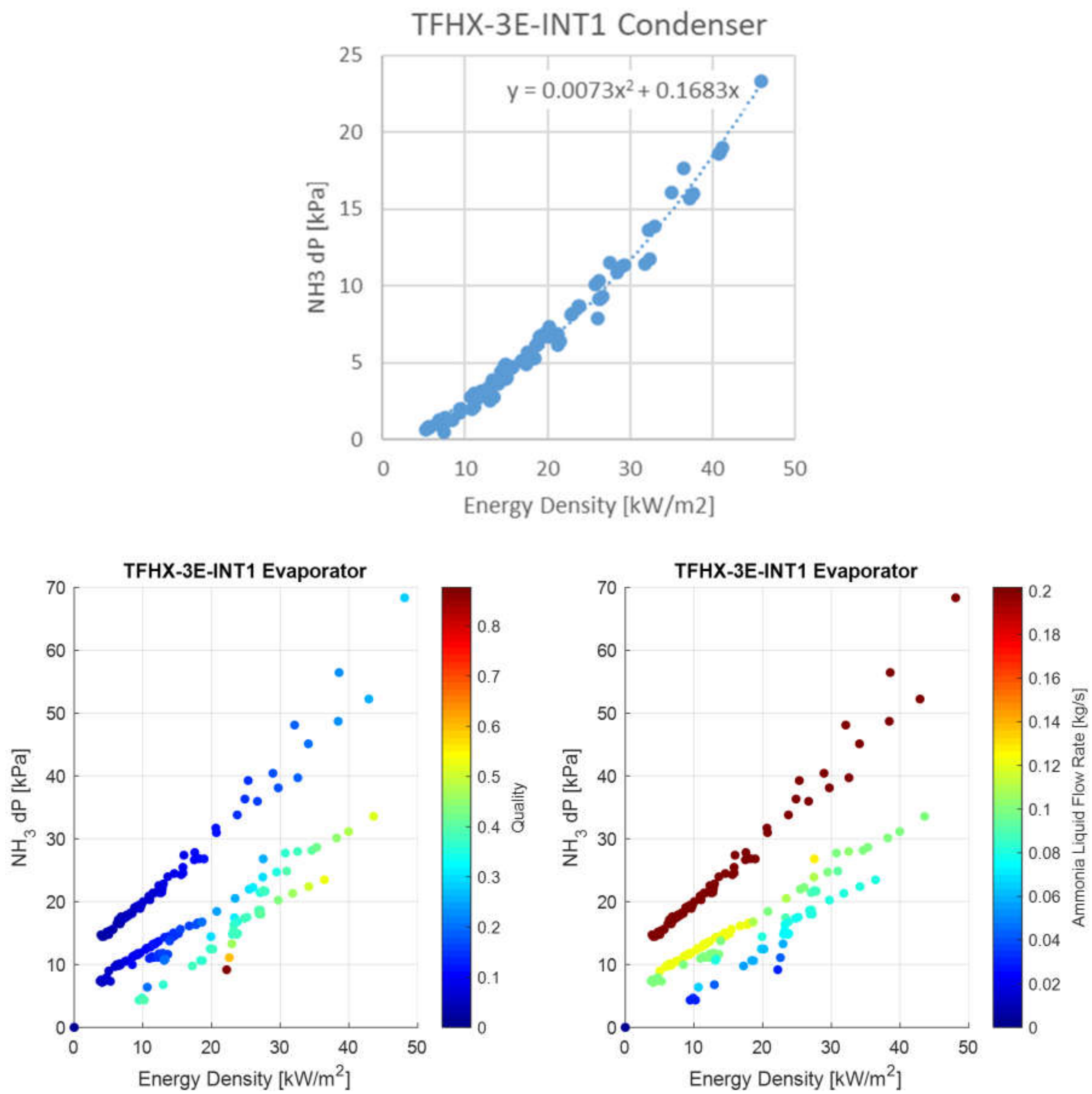

Figure 46. TFHX-3E-INT1 ammonia-side pressure drop vs energy density.

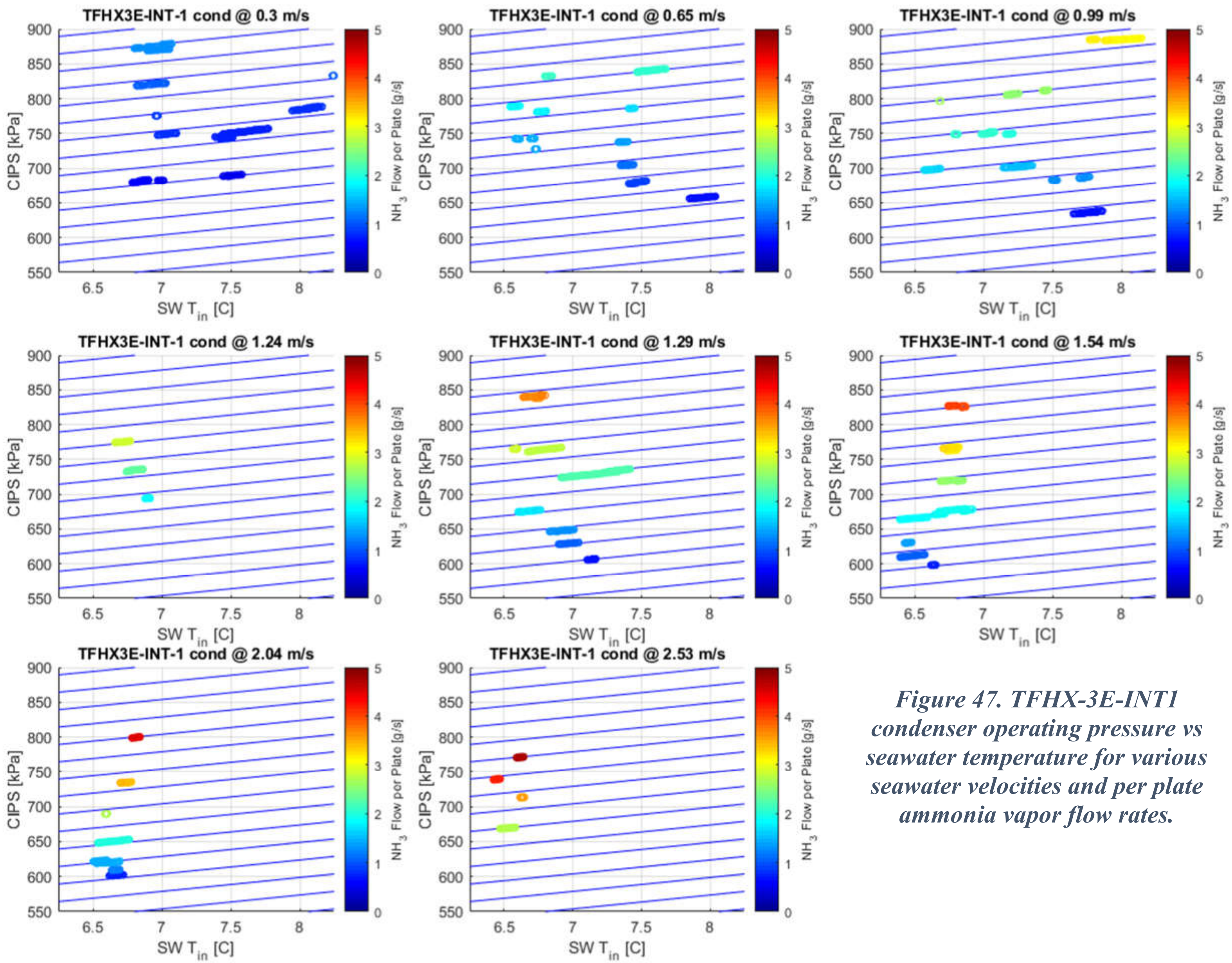

Figure 47. TFHX-3E-INT1 condenser operating pressure vs seawater temperature for various seawater velocities and per plate ammonia vapor flow rates.

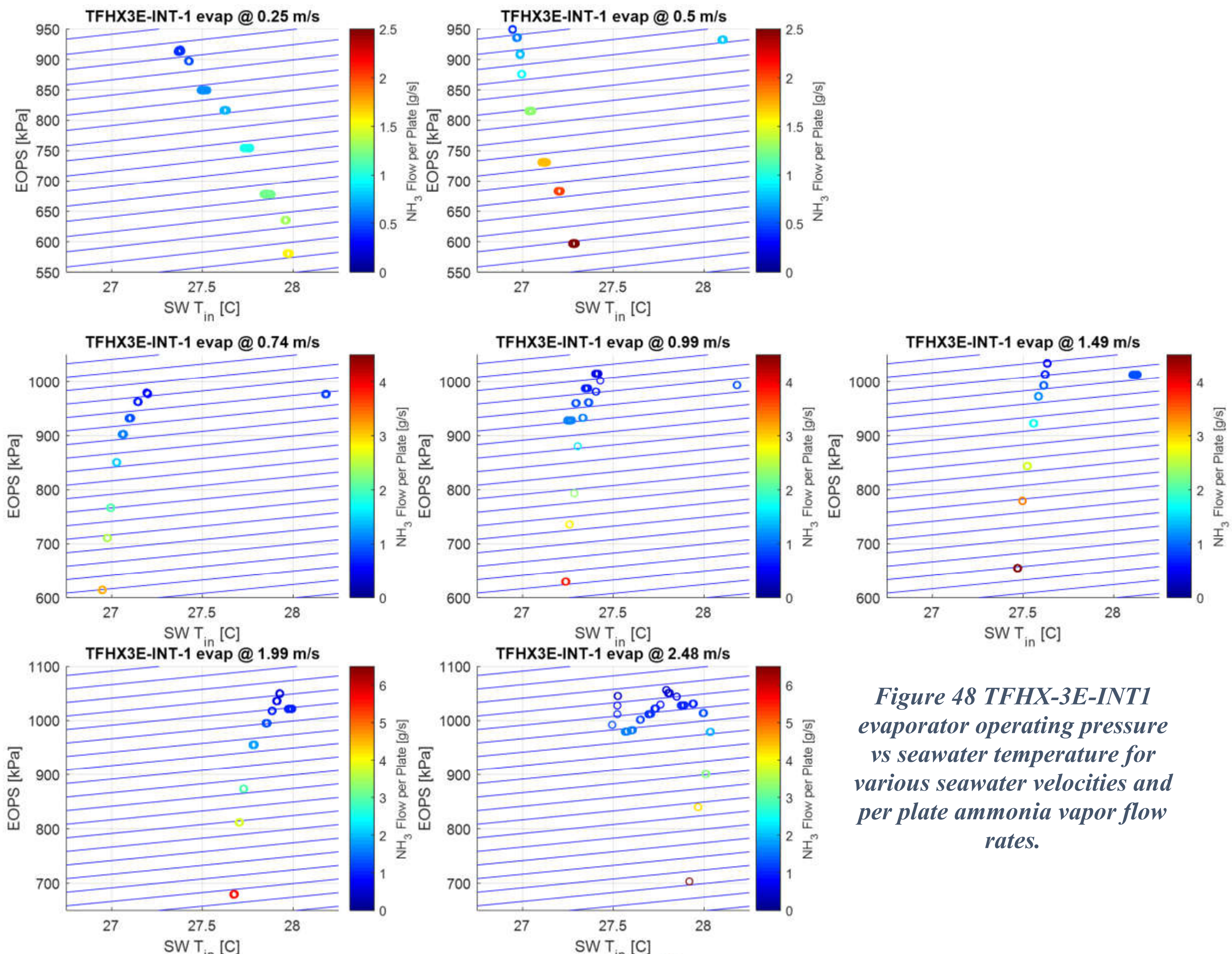

Figure 48 TFHX-3E-INT1 evaporator operating pressure vs seawater temperature for various seawater velocities and per plate ammonia vapor flow rates.

3.5.1. Ammonia-side Operating Pressure

In general, pressure vs. seawater inlet temperature follow closely with the ammonia saturation curves. Small variations in seawater flow rates can lead to deviations from the curve. For the evaporator, as pressure drop is dependent on the liquid ammonia flow rate, only data taken at constant ammonia liquid flow rate = 0.2 kg/s is shown.

The approach temperature is defined by the difference between the seawater inlet temperature and the ammonia saturation temperature corresponding to the heat exchanger operating pressure. A low approach temperature is more favorable. For a fixed seawater velocity, approach temperatures increase linearly with energy density. For the same energy density, increasing seawater velocity lowers the approach temperature.

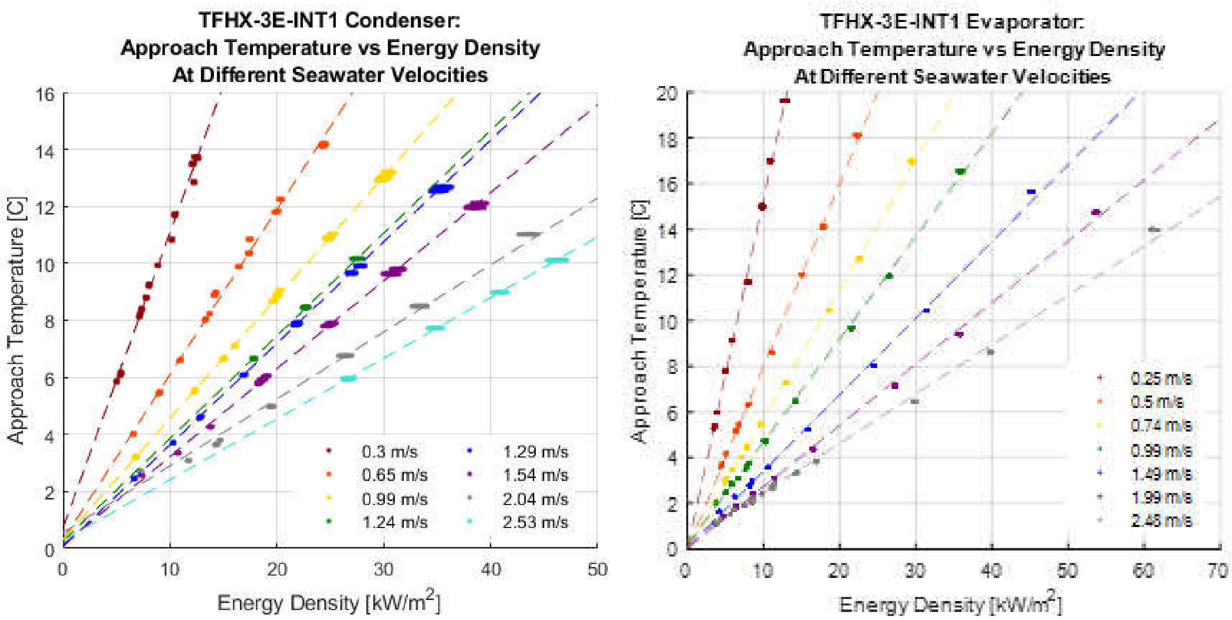

Figure 49. TFHX-3E-INT1 approach temperature vs energy density at different seawater velocities.

3.5.2. Overall Heat Transfer Coefficient

U-value is dependent on seawater flow rate, ammonia vapor flow rate, and quality. Increasing seawater velocity resulted in a diminishing rate of increase in U-value, but the effect was not as drastic as previously observed logarithmic relationships. This is likely due to the tested seawater velocity range; the logarithmic relationship will likely be observed if higher seawater velocities were tested.

As a condenser, U-value increased slightly with increasing ammonia vapor flow rate. As an evaporator, U values increased then decreased with ammonia vapor flow rates. The degree of increase depended on seawater velocity. For example, at 2.5 m/s, U value increased from 6 to 9 kW/m^2/K with increasing energy density before decreasing whereas at 1.5 m/s U value increased from 5 to 6 kW/m^2/K.

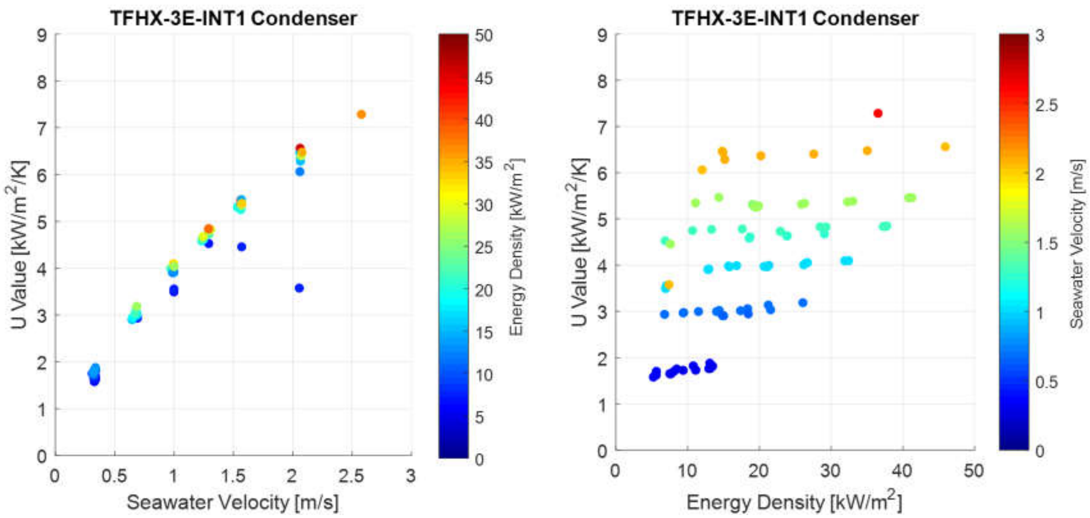

Figure 50. TFHX-3E-INT1 condenser U value versus seawater velocity and energy density.

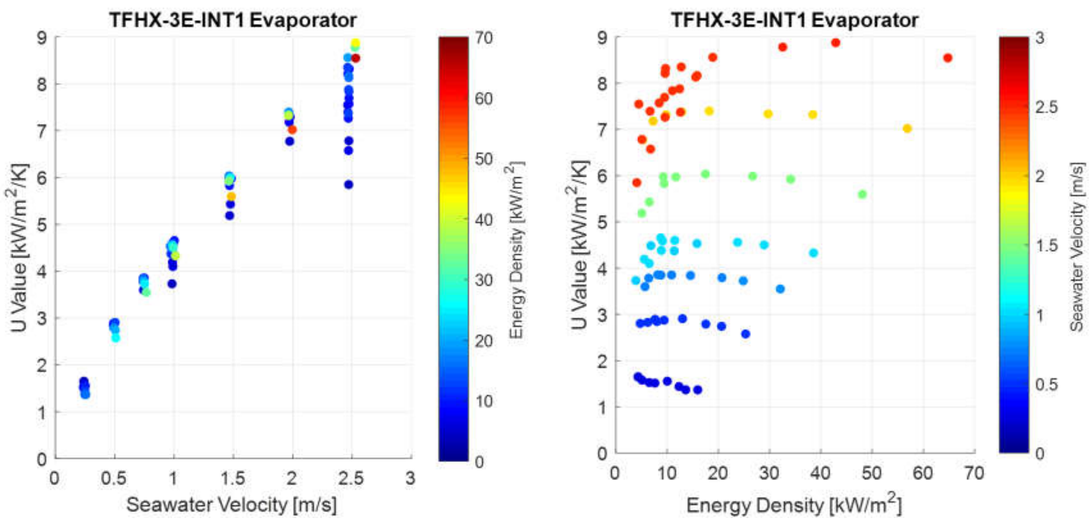

Figure 51. TFHX-3E-INT1 evaporator U value versus seawater velocity and energy density.

3.5.3. Convective Coefficient

Convective coefficients can be calculated from U values by making two assumptions: 1) The ammonia side convective coefficient depends only on the energy density (or ammonia flow rate) and is independent of the seawater side, and 2) the seawater convective coefficient is only dependent on the seawater velocity and is independent of the ammonia side. In order to solve for the convective coefficients, for each seawater flow rate, U values at matching energy densities must first be found. This is accomplished by fitting a curve to U vs energy density for each seawater velocity tested.

For the condenser, U values were fitted with a logarithmic curve, $U = a\log(Energy\ Density) + b$ (Figure 52). For the evaporator, U values were fitted with a 3rd order polynomial or Gaussian function, $U = e^{-\left(\frac{Energy\ Density - b}{c}\right)^2}$ (Figure 53). The fitted U values are plotted as lines and the averaged data points as x's in Figure 52 and Figure 53. U values used to calculate convective coefficients are shown in Table 13 and Table 14 and the resulting convective coefficients are shown in Figure 54.

The seawater convective coefficients (Figure 55) are in agreement between condenser and evaporator test conditions. For the condenser, the ammonia convective coefficient (Figure 55) increase with increasing ammonia flow rate whereas in the evaporator, the ammonia convective coefficient peaks at energy density between 15-20 kW/m^2.

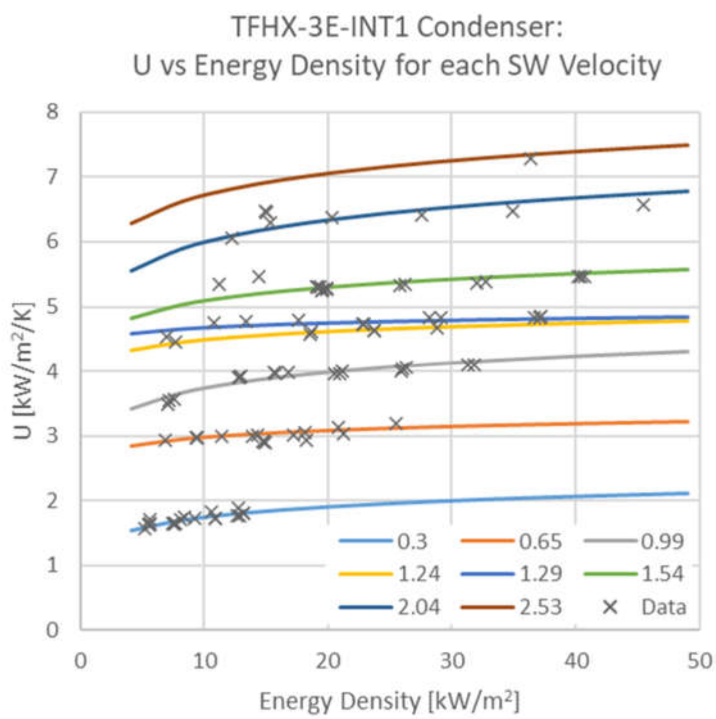

Figure 52. TFHX-3E-INT1 condenser fitted and summarized U values.

Table 13. TFHX-3E-INT1 condenser U values used to calculate convective coefficients

		Energy Density			
		8.541943	17.08389	25.62583	34.16777
m/s	0.3	1.704	1.859633	1.950672	2.015265
	0.65	2.948	3.053812	3.115708	3.159624
	0.99	3.6652	3.911563	4.055676	4.157926
	1.29	4.6528	4.726883	4.77022	4.800967
	1.54	5.0282	5.240095	5.364046	5.45199
	2.04	5.898	6.238766	6.438101	6.579532
	2.53	6.619	6.955251	7.151944	7.291501

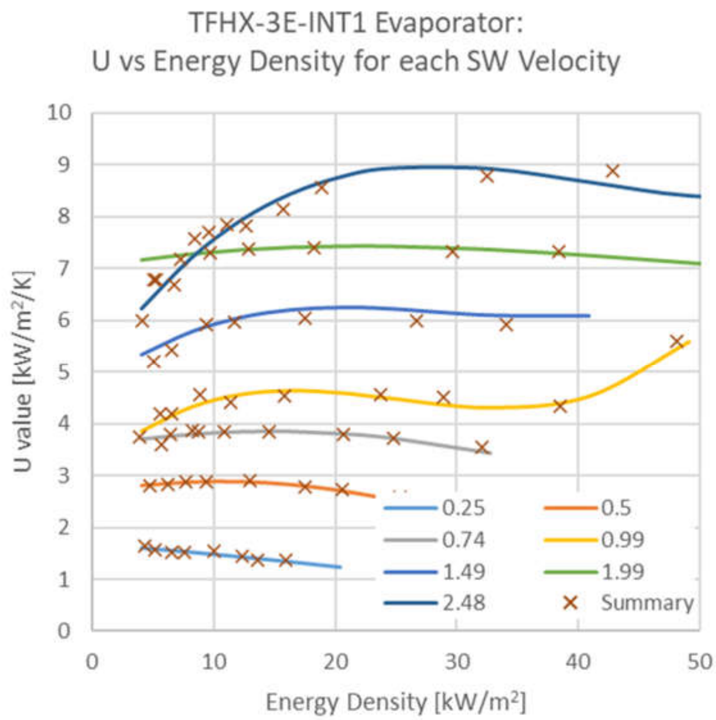

Figure 53. TFHX-3E-INT1 evaporator fitted and summarized U values

Table 14. TFHX-3E-INT1 evaporator U values used to calculate convective coefficients

		Energy Density				
		12.8129	17.0839	21.3549	25.6258	34.1678
m/s	0.25		1.3322			
	0.50		2.8239	2.7138	2.5544	
	0.74	3.8512	3.8551	3.8139	3.7290	3.4411
	0.99	4.5620	4.6346	4.5912	4.4860	4.3062
	1.49	6.0614	6.2096	6.2553	6.2310	6.1036
	1.99	7.3520	7.3989	7.4196	7.4174	7.3579
	2.48	7.9290	8.4383	8.7611	8.9283	8.9202

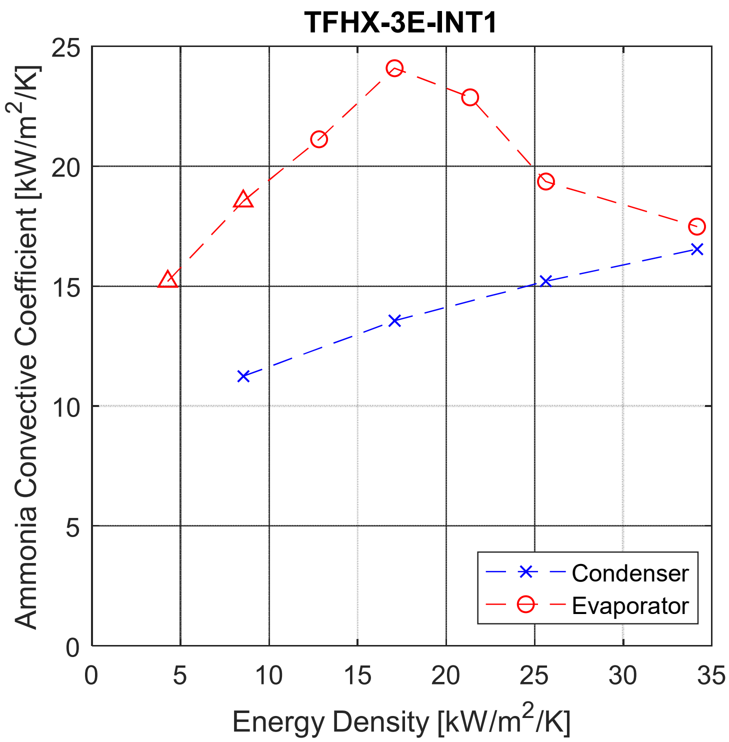

Figure 54. TFHX-3E-INT1 ammonia convective coefficients. The triangles represent ammonia convective coefficients for the evaporator calculated using seawater convective coefficients and averaged U values from the data.

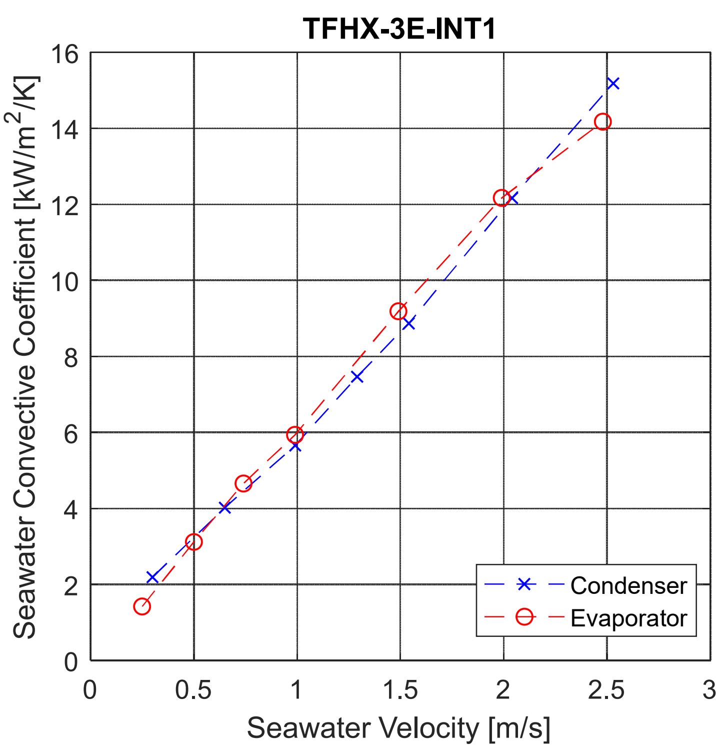

Figure 55. TFHX-3E-INT1 seawater convective coefficients.

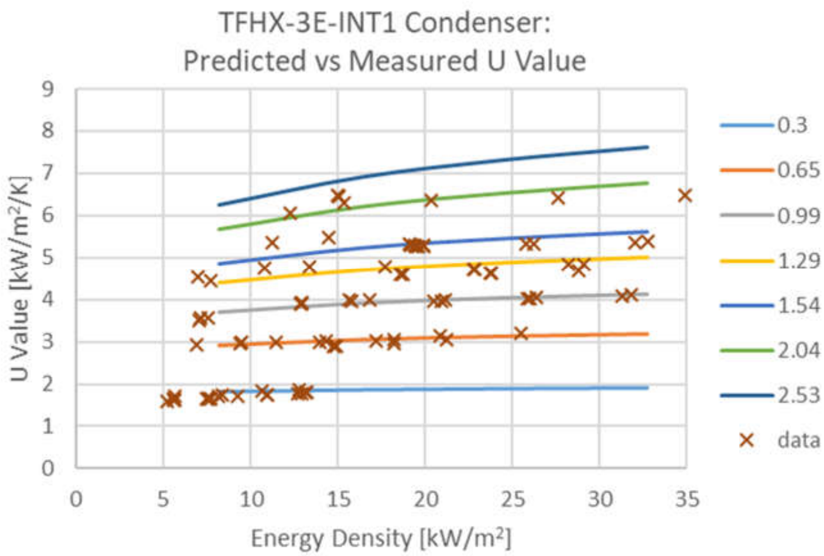

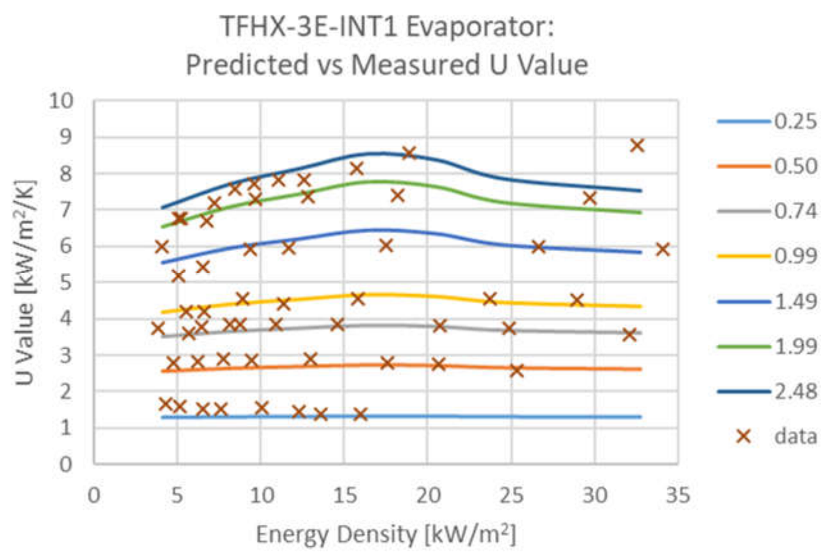

Figure 56. Predicted vs measured U values.

U values recalculated using the convective coefficients were within +/- 15% of the observed U values.

3.6. COMPARISON OF TFHX PERFORMANCE

In total, Makai has tested six configurations of seawater-ammonia TFHXs. All six configurations were in the cross-flow orientation with different manifold designs, varying ammonia and seawater channel spacings, and varying lengths (Table 15).

Table 15. TFHX dimension comparison

	3B-1	3B-2	3C-1	3C-2	3C-3	3E-INT1
NH3 Channel Spacing (mm)	0.745	0.386	0.42	0.42	0.42	0.373
NH3 Path Length (m)	0.2435	0.2435	0.46	0.46	0.46	0.46
SW Channel Spacing (mm)	3.015	3.374	3.339	1.396	0.7484	0.41
SW Path Length (m)	1.208	1.208	0.285	0.285	0.285	0.2495

3.6.1. Seawater Side

As expected, the length-adjusted pressure drop for smaller seawater channels was higher than for larger channels.

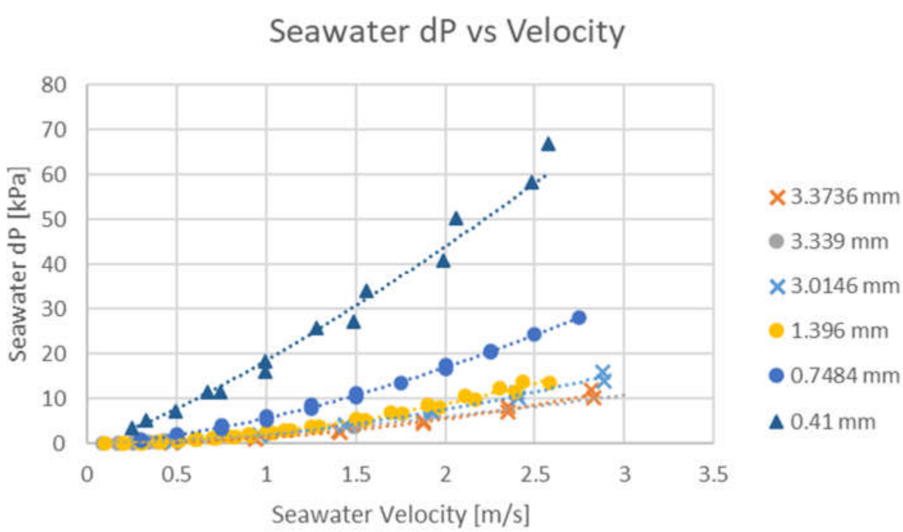

Figure 57. Comparison of TFHX seawater pressure drop (length adjusted).

Seawater heat transfer coefficients increased almost linearly with velocity. For the same pressure drop, larger channels have higher convective coefficients than smaller channels.

When plotted together, the seawater convective coefficient for TFHX-3E-INT1 appears high, suggesting the ammonia convective coefficients may actually be higher than reported in the next section. One explanation may be the increase in ammonia convective coefficients at low power densities in evaporator mode; this trend was not observed in other data sets and may indicate a non-uniform condition, particularly since testing was conducted at very low quality.

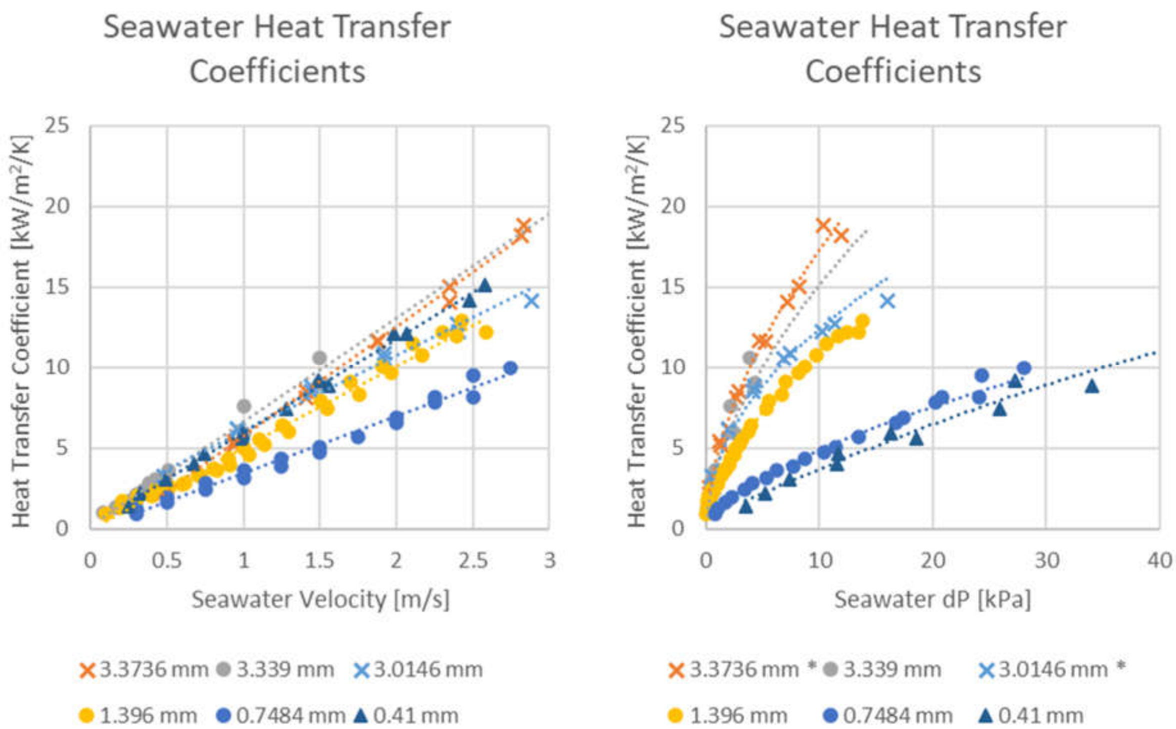

Figure 58. Comparison of TFHX seawater convective coefficient vs velocity and dP.

3.6.2. Ammonia Side

The ammonia-side convective coefficients had reasonable agreement across the different configurations (including previously tested TFHX-3B-1 and -2). TFHX-3B-2, TFHX-3Cs, and TFHX-3E-INT1 had comparable ammonia-side channel spacings, but the ammonia path length and manifold designs were significantly different. 3B-1 and 3B-2 utilized long manifolds with large openings that had low pressure drop and an overall ammonia passage length of 0.2435 m. TFHX-3Cs had significant pressure drop in the manifold and transition region and an ammonia path length at 0.460 m. The transition zone pattern constriction in TFHX-3C was corrected in TFHX-3E-INT1 which also had an ammonia passage length of 0.46 m[1]. The 3E-INT1 evaporator pressure drop is higher than expected due to the low quality (2.5-40%) maintained during testing.

[1] The ammonia passage length in the test section for the 3C plates was 0.37 m and the ammonia passage length in the 3E-INT1 test section was 0.25 m, but the measured pressure drop is for the entire ammonia passage length of the plate (0.46 m).

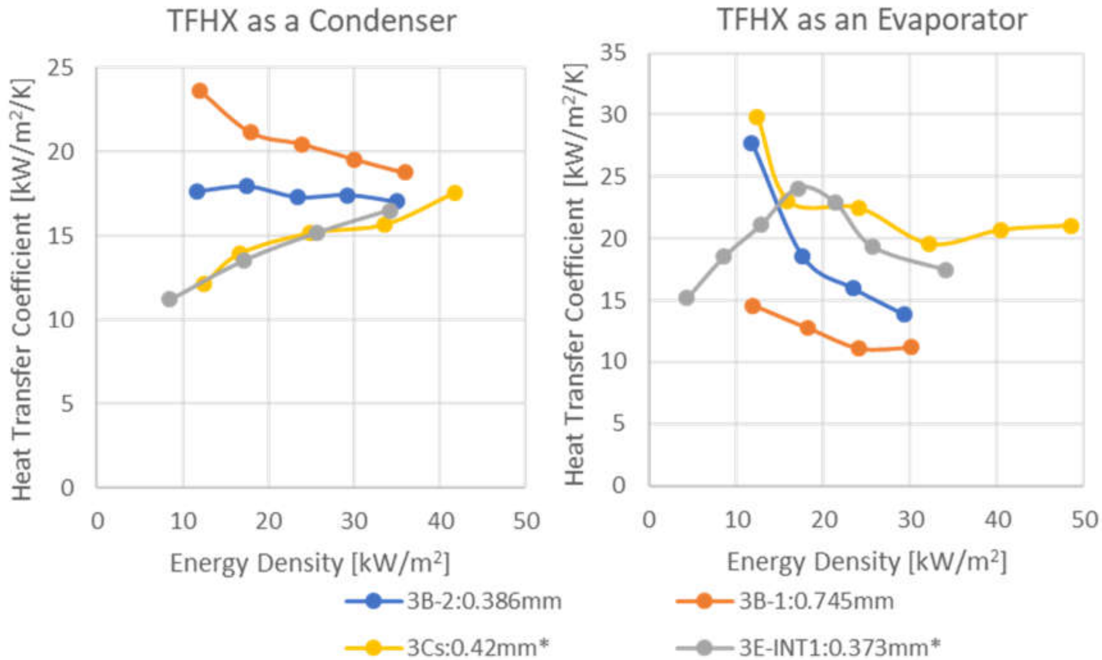

Figure 59. Comparison of TFHX ammonia heat transfer coefficient vs energy density.

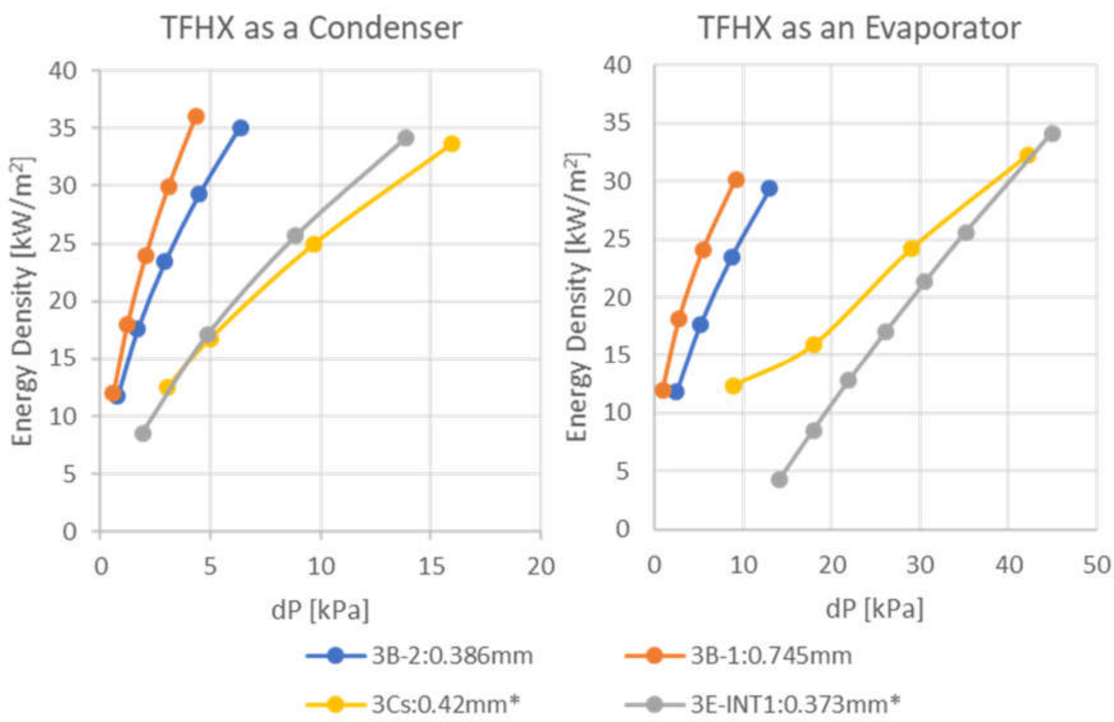

Figure 60. Comparison of TFHX ammonia heat transfer coefficient vs ammonia dP.

3.7. DISUSSION

TFHXs can be evaluated on the basis of compactness, performance, and cost.

3.7.1. Compactness

In terms of compactness, TFHX-3C-3 followed by the TFHX-3E-INT1 contain more heat transfer area per cubic meter (m^2/m^3) than the previously tested TFHX-3B style heat exchangers, APV's Plate-and-Frame condenser and evaporator, CHART's BAHX3 Brazed-Fin-Aluminum evaporator, and Lockheed Martin's shell and tube condenser.

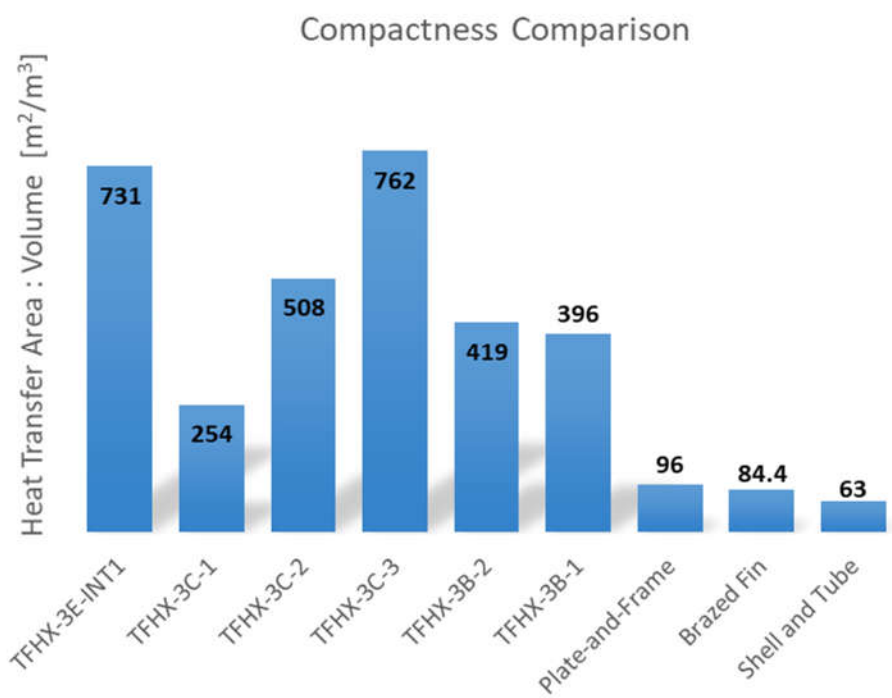

Figure 61. TFHX heat exchangers have more heat transfer area per volume compared to the previously tested plate-frame (APV), brazed fin (BAHX3), and shell and tube (ETHX) heat exchangers.

At the same energy density, TFHXs require only 5-10% of the volume of previously tested heat exchangers to produce the same duty.

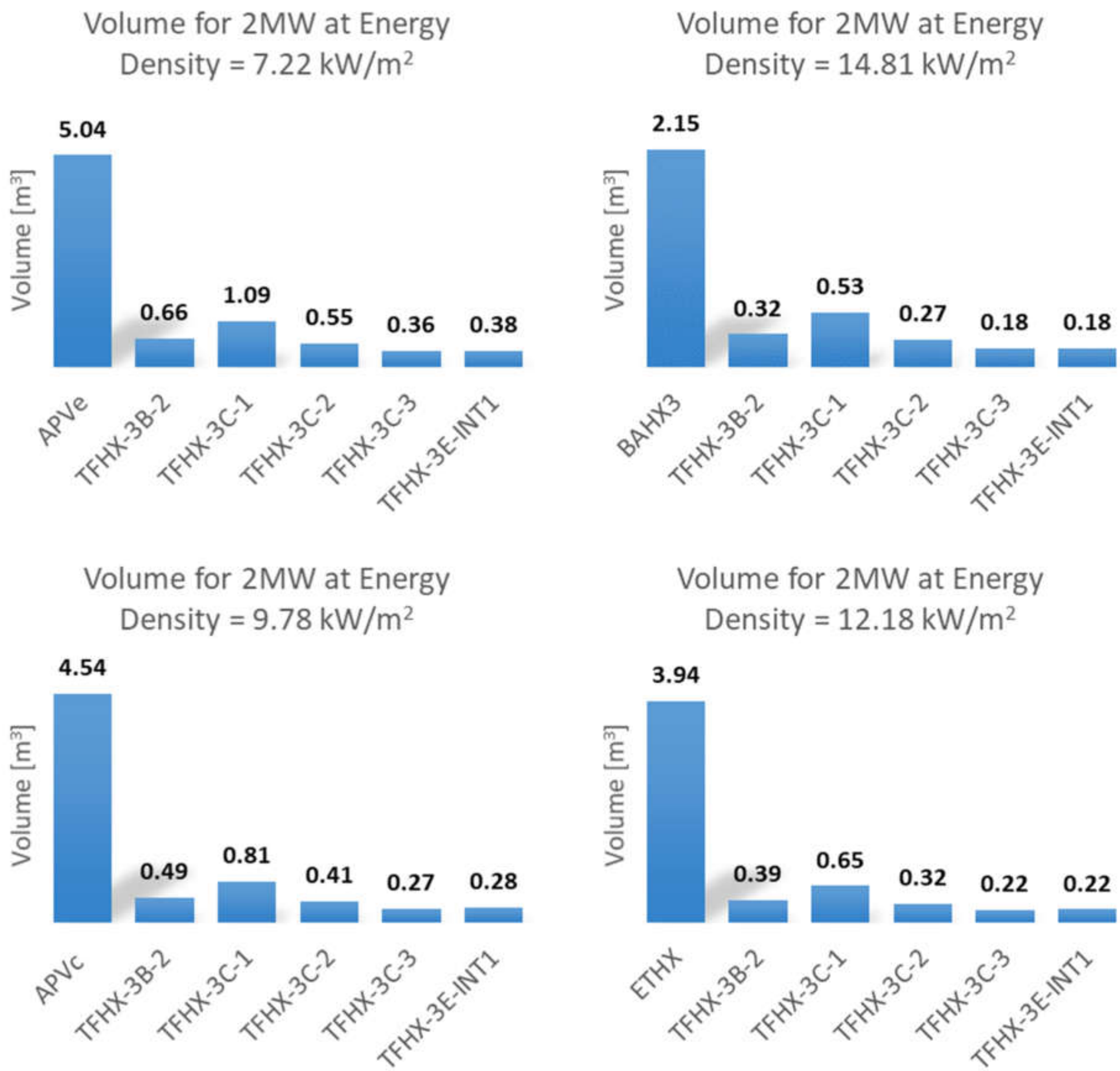

Figure 62. Comparison of volume required for 2MW of duty at various energy densities. Energy density was selected to match previously tested heat exchangers.

3.7.2. Overall Heat Transfer Coefficient

The overall heat transfer coefficient is largely dependent on seawater flow rate but some variation with ammonia flow rate was observed. To compare between the heat exchangers, the TFHXs were scaled up 2MW and then U-value was plotted as a function of seawater pumping power. The scaling was done at energy densities that were closest matches to the energy densities of the previously tested heat exchangers (Table 16). For example, to compare with the APV evaporator (energy density = 7.27 kW/m^2), the TFHX-3C-1 test point at energy density = 8.17 kW/m^2 was used; at this energy density, 1266 plates are required to produce 2MW. The seawater pumping power is calculated at various tested velocities by using the recorded pressure drop and the flow rate for 1266 plates.

Table 16. Energy densities corresponding to 2MW duty.

Heat Exchanger	Energy Density at 2MW duty [kW/m²]	Corresponding Energy Density for TFHXs used in comparisons [kW/m²]				
		TFHX-3E-INT1	TFHX-3C-1	TFHX-3C-2	TFHX-3C-3	TFHX-3B-2
APV condenser	9.71	8.18	8.52	8.49	8.53	11.69
ETHX	12.2	12.27	16.25	12.65	12.69	11.69
APV evaporator	7.27	8.18	8.17	8.23	8.13	11.8
BAHX3	14.81	16.36	16.25	16.42	16.5	17.6

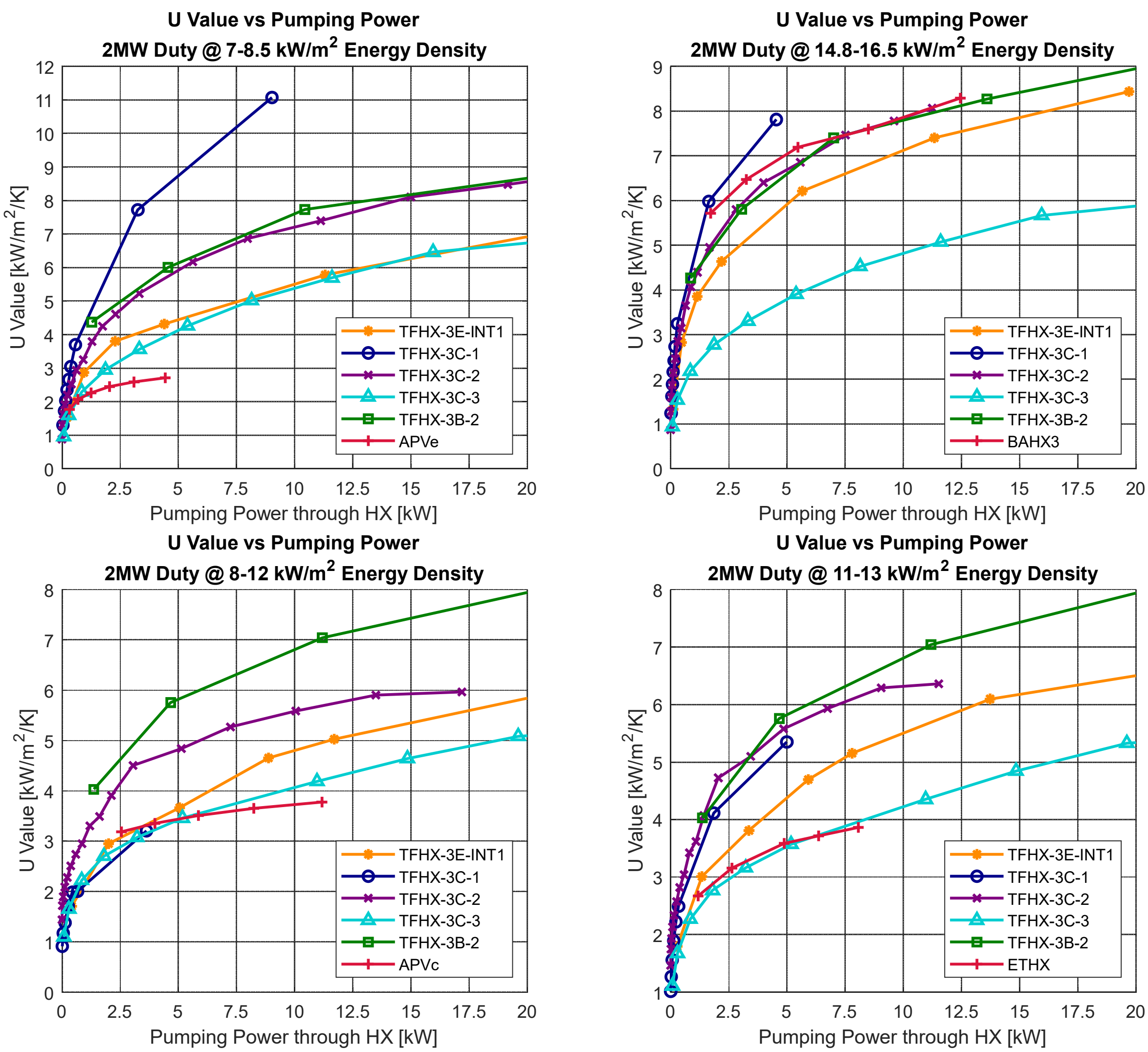

Figure 63. U-value vs Seawater Pumping Power comparison.

All TFHXs had higher than or comparable U values for the same seawater pumping power compared to all previously tested heat exchangers except BAHX3. With the small channels, TFHX-3C-3 and TFHX-3E-INT1 had lower U-values for the same pumping power compared to BAHX3 while the other TFHXs were comparable or better than BAHX3.

The TFHXs have comparable or better performance than previously tested performance with a 4-15X reduction in volume.

3.7.3. Convective Coefficients

Ammonia convective coefficients can be compared for different heat exchangers at the same energy density. As a condenser, unlike previously tested heat exchangers (including the TFHX-3Bs), TFHX-3E and THFX-3Cs show in increase in ammonia convective coefficient with increasing energy density, suggesting vapor shear contributes to the ammonia convective coefficient. Compared to TFHX-3B, although the effective ammonia channel spacing was the same, the THFX-3E and THFX-3Cs' condensation coefficients were up to 60% lower. The 3E and 3C manifolds are ~1/3 the plate width whereas in 3B heat exchangers, the manifolds were the full width of the plate. There is also a transition zone with a different weld patterns between the manifold and the main heat transfer area. Compared to TFHX-3Bs, the more constricted manifold and the additional length of travel in non-heat transfer areas may lead to superheating and contribute to a reduced overall heat transfer coefficient.

As an evaporator, the TFHX ammonia heat transfer coefficients were 1.5-2X higher than BAHX3 or APV, depending on the energy density. TFHXs were tested at higher energy densities than either APV or BAHX3. However, in the TFHXs, the ammonia convective coefficient decreases with increasing energy density whereas in BAHX3 and APVe, there is either no change or a slight increase in the convective coefficient with increasing energy density.

In the tested evaporators, ammonia boiling falls under the flow boiling classification – i.e., ammonia has a velocity relative to the heat transfer surface – vice pool boiling where ammonia is at rest relative to the heat transfer surface. Flow boiling can be further divided into subcooled boiling (where bubbles form locally but collapse/reabsorb into the bulk liquid that is still subcooled) and saturated boiling where the bulk liquid is at saturation and bubbles can form and grow. There are two main mechanisms of saturated boiling – nucleate boiling and convective boiling. In nucleate boiling, bubbles form at nucleation sites on the heat transfer surface. In convective boiling, ammonia is directly vaporized at the liquid/vapor interface without bubble formation. For either mechanism of saturated boiling, surface must be wetted (i.e., not experience dry-out) for efficient heat transfer. The ammonia-side convection coefficient solved using U-values is the overall average of all boiling mechanisms for that ammonia flow rate.

Compared to the APV evaporator, Makai believes TFHXs' ammonia-side convective coefficients are higher because the smaller ammonia channels result in higher ammonia liquid velocities which improve convective boiling. In BAHX3, fins are used to improve ammonia-side convection by increasing the heat transfer area (i.e., more wetted surface area). It is customary to use only the flat plate area (disregarding the increase in actual heat transfer area due to addition of fins) when calculating U-value. This means U-value will decrease if we were to use an effective area that includes the fin efficiency and increased heat transfer area due to fins.

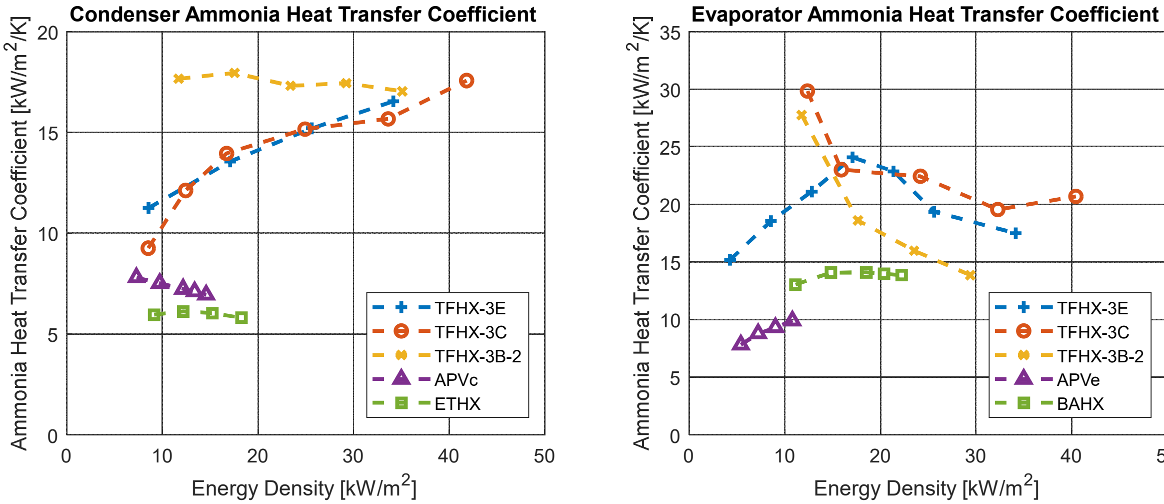

Figure 64. Comparison of ammonia convective coefficients.

Similar to U-value comparisons, seawater convective coefficients can be compared for the same seawater pumping power for the same duty at the same energy density. TFHX-3C-1 had the highest seawater convective coefficient vs pumping power in each case. The TFHX-3B-2 had comparable seawater convective coefficient to the heat exchanger it was being compared to. TFHX-3C-3 and TFHX-3E-INT1 had significantly smaller seawater channels and most of the tested seawater range remained in the laminar region (Re < 2300); seawater convective coefficients were expected to be low and pumping power high due to increased pressure drop.

Although the larger channels had higher convective coefficients for the same pumping power, the smaller channels can have 2-3X the heat transfer area within the same volume. As long as the convective coefficient is not 2-3X lower, for the same volume, the overall duty using a unit with smaller channels can be higher.

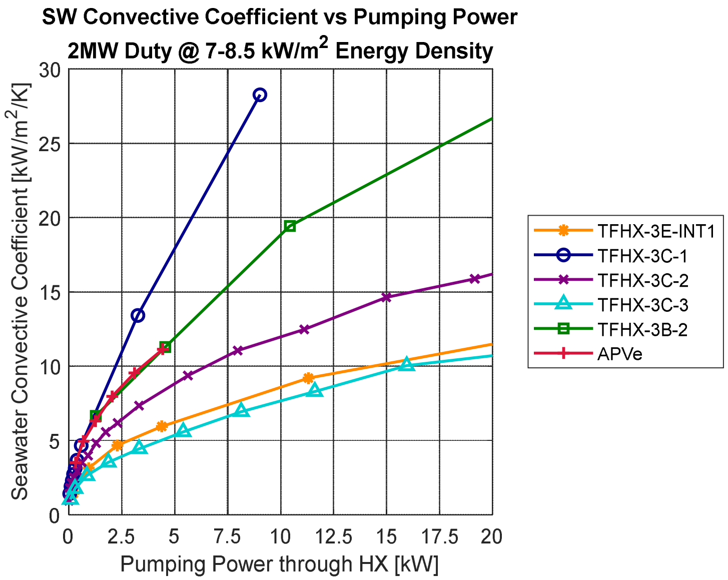
SW Convective Coefficient vs Pumping Power
2MW Duty @ 7-8.5 kW/m2 Energy Density
Seawater Convective Coefficient [kW/m2/K]
Pumping Power through HX [kW]
TFHX-3E-INT1
TFHX-3C-1
TFHX-3C-2
TFHX-3C-3
TFHX-3B-2
APVe

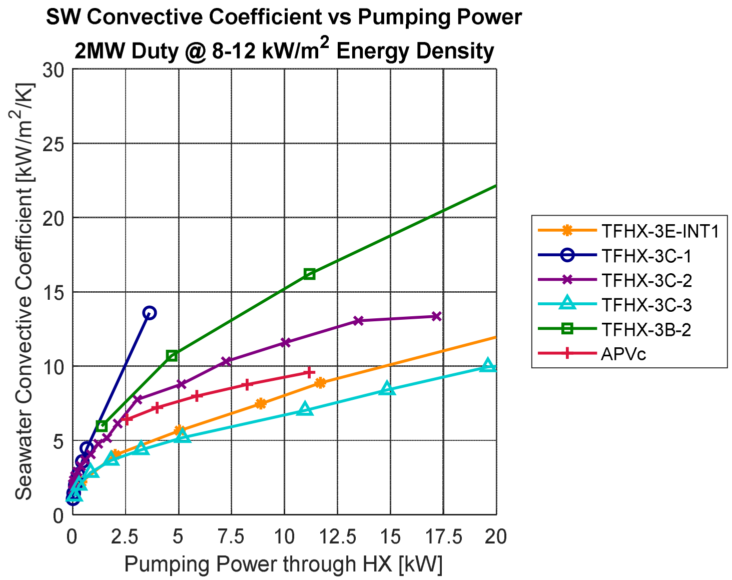
SW Convective Coefficient vs Pumping Power
2MW Duty @ 8-12 kW/m2 Energy Density
Seawater Convective Coefficient [kW/m2/K]
Pumping Power through HX [kW]
TFHX-3E-INT1
TFHX-3C-1
TFHX-3C-2
TFHX-3C-3
TFHX-3B-2
APVc

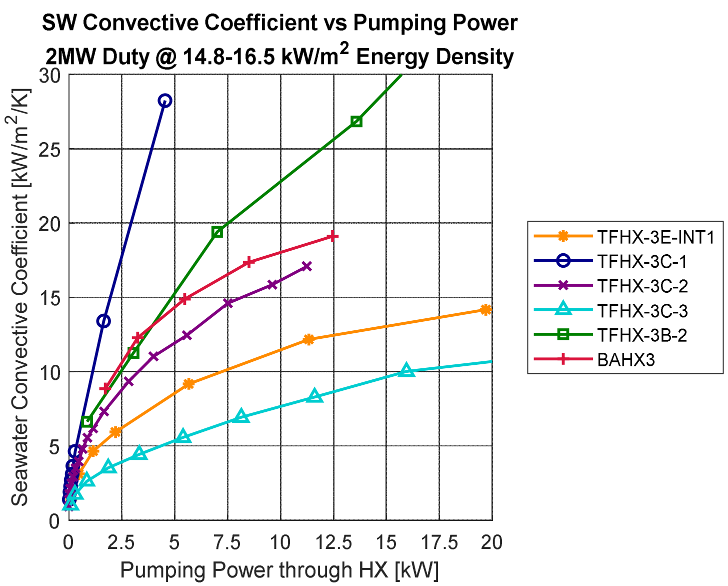
SW Convective Coefficient vs Pumping Power
2MW Duty @ 14.8-16.5 kW/m2 Energy Density
Seawater Convective Coefficient [kW/m2/K]
Pumping Power through HX [kW]
TFHX-3E-INT1
TFHX-3C-1
TFHX-3C-2
TFHX-3C-3
TFHX-3B-2
BAHX3

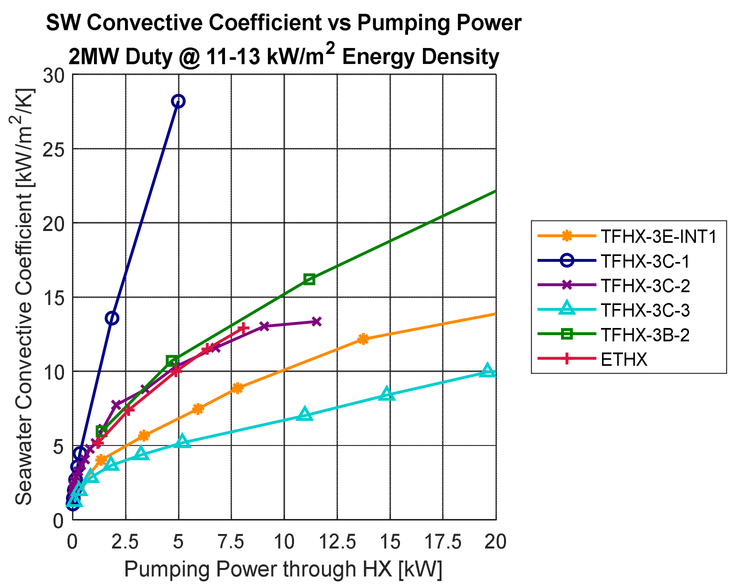
SW Convective Coefficient vs Pumping Power
2MW Duty @ 11-13 kW/m2 Energy Density
Seawater Convective Coefficient [kW/m2/K]
Pumping Power through HX [kW]
TFHX-3E-INT1
TFHX-3C-1
TFHX-3C-2
TFHX-3C-3
TFHX-3B-2
ETHX

Figure 65. Seawater convective coefficient vs pumping power comparison.

3.7.4. Approach Temperature

In OTEC applications, for a given seawater pumping power, having a tight approach temperature (the difference between the heat exchanger ammonia saturation temperature and the seawater inlet temperature) is advantageous in producing the highest pressure differential across the turbine for the lowest seawater pumping power. The approach temperature is affected by the seawater flow rate and energy density. Similar to the U value comparisons, approach temperatures can be compared to previously tested heat exchangers by scaling up the TFHXs to 2MW duty at comparable energy densities.

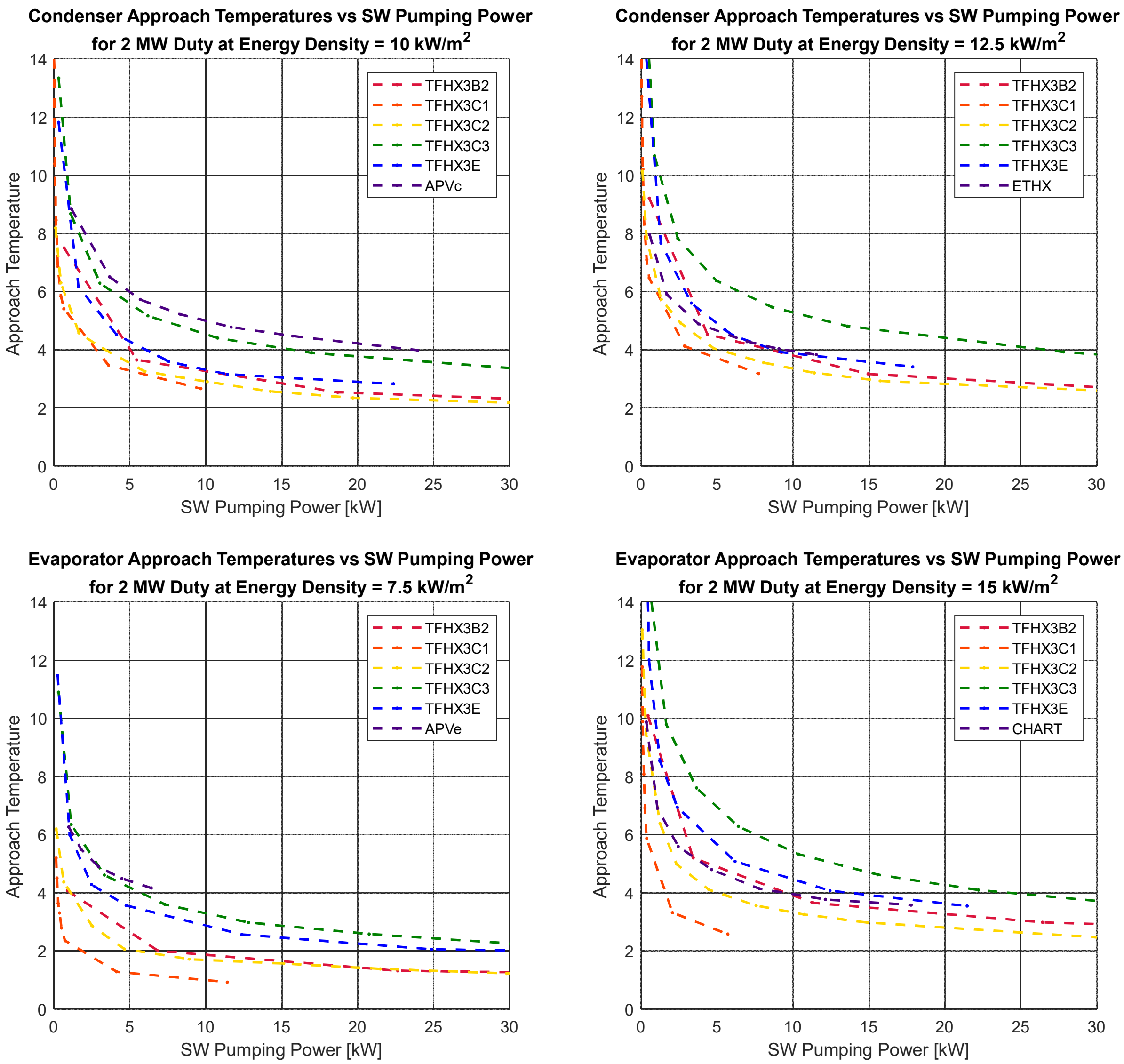

Figure 66. Comparison of approach temperature vs seawater pumping power at 2MW duty and comparable energy densities.

For the same pumping power, TFHX-3C-1 and 3C-2 had the lowest approach temperatures in all four comparisons. 3B-2 and 3E had comparable approach temperatures that were higher than 3C-1 and 3C-2 at low pumping powers (< 5 kW), but at higher pumping powers (> 5 kW), the difference was negligible.

The APV evaporator was in a crossflow configuration, the CHART evaporator was in counterflow configuration and both APV and ETHX condensers were in parallel flow; whereas all TFHXs were tested in a crossflow configuration. Approach temperatures are expected to improve in a counterflow configuration. Even with non-optimal flow arrangement, the TFHXs performance was on par or better than previously tested heat exchangers in a fraction of the volume.

3.7.5. Economics

In addition to improving the performance and compactness of heat exchangers, cost reduction is a key factor in Makai's heat exchanger development program. With each heat exchanger design iteration, Makai identifies and improves on the components that most significantly limit heat exchanger performance and cost.

Overall, the TFHX-3Bs cost was estimated at $2691/m^2 of heat transfer area. Several components were targeted for improvement:

- Plate size – the 1.2 m long plate was difficult and slow to fabricate.
- Plate spacing – the plate spacing was 3.92 mm, which limited the compactness
- Manifolds – materials comprised 54% of the TFHX-3B cost and manifolds (2 per plate) contributed 81% of the materials cost.

Makai has made significant improvement in reducing the material cost in TFHX-3C and TFHX-3E. Although manifolds still comprise ~70% of the material costs, material costs have been reduced by 50% from TFHX-3B. The overall cost per m^2 of heat transfer area was reduced from $2691/m^2 to $1877/m^2 in TFHX-3C and $1297/m^2 in TFHX-3E.

In terms of fabrication time, a TFHX-3B plate had 0.58 m^2 of heat transfer area and required 374 minutes to fabricate. A TFHX-3C plate has 0.21 m^2 of heat transfer area and requires 120.5 minutes to fabricate. Three TFHX-3C plates can be produced in the same time it takes to produce at TFHX-3B plate. A TFHX-3E plate had 0.125 m^2 of heat transfer area and required 60 min to fabricate.

Initially, the HSWS is expected to increase the hourly production of heat transfer area by 5X. This will lower TFHX-3E costs from $1300/m^2 to $415/m^2 by reducing the time to fabricate a plate from 60 minutes to 12 minutes. As discussed in Section 2.2, the time required to fabricate a 0.3m x 0.5m plate is actually 6 minutes; at full capacity, the HSWS will reduce the TFHX cost to < $300/m^2.

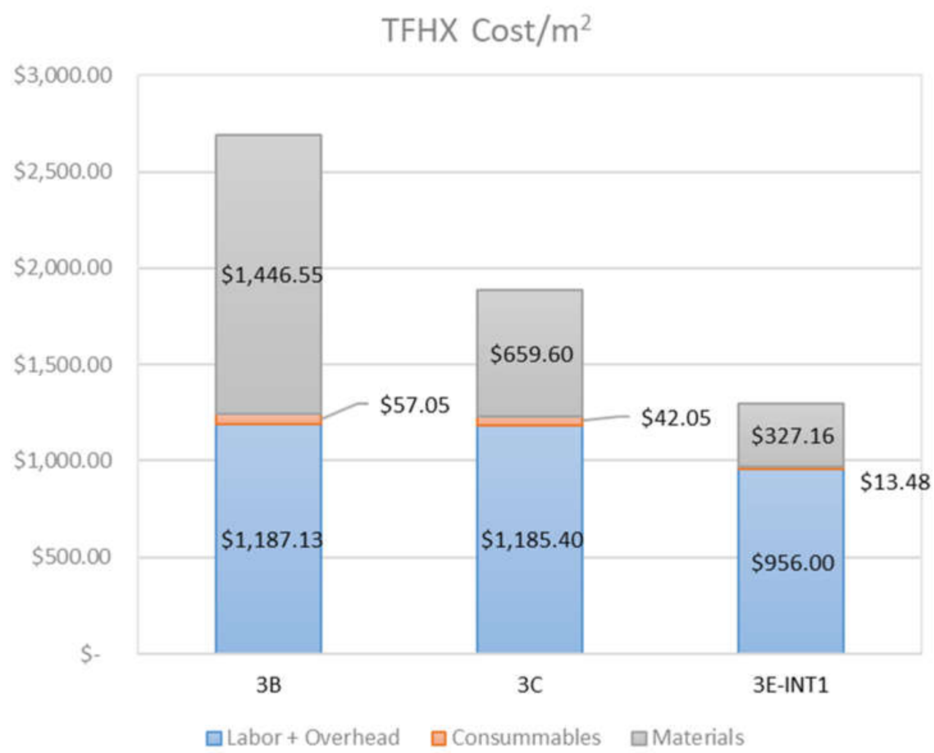

Figure 67. Comparison of costs for TFHX-3B, TFHX-3C, and TFHX-3E.

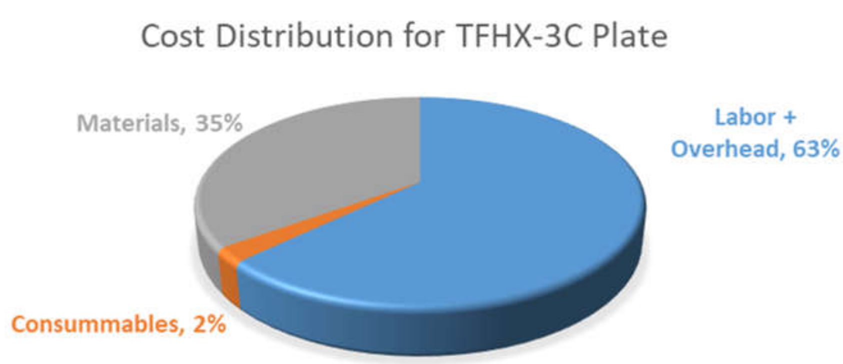

Category	Qty	Rate	Total Cost
Labor + Overhead	2 hrs	$100/hr	$ 200.00
Consummables	2.96 cu. ft.	$3.00 / cu. ft.	$ 8.87
Materials	0.215 m^2	$ 651.93 /m^2	$ 139.11
		Cost per Plate	$ 397.98
		Cost per m^2 heat transfer area	$ 1,887.05

Figure 68. Cost distribution for TFHX-3C plate.

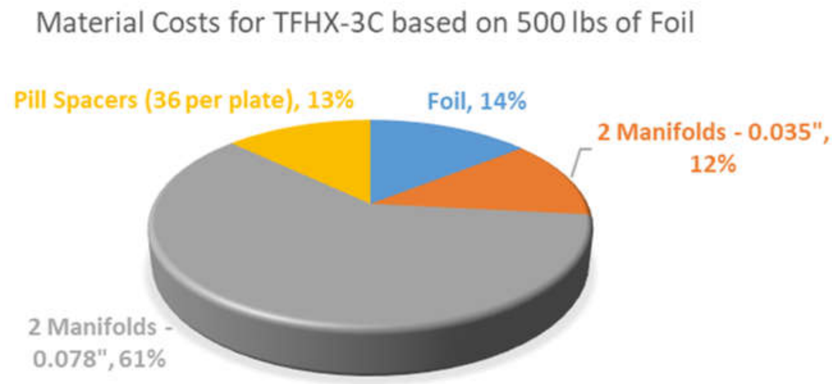

Plate Material	Qty.	Cost
Foil @ $75.18 / lb	0.28 lb	$ 19.91
2 Manifolds - 0.035"	2	$ 17.20
2 Manifolds - 0.078"	2	$ 84.00
Pill Spacers	36	$ 18.00
Material cost per plate	$139.11	
HX area per plate	0.211 m^2	
Material cost/m^2	$ 660	

Figure 69. Breakdown of material costs for TFHX-3C plate.

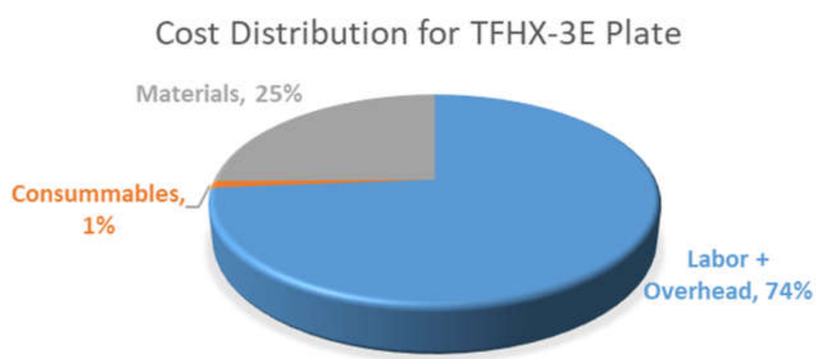

Category	Qty	Rate	Total Cost
Labor + Overhead	1.2 hrs	$100/hr	$ 119.50
Consummables	0.56 cu. ft.	$3.00 / cu. ft.	$ 1.69
Materials	0.125 m^2	$ 327.16 /m^2	$ 40.90
		Cost per Plate	$ 162.08
		Cost per m^2 heat transfer area	$ 1,296.64

Figure 70. Cost distribution for TFHX-3E plate.

Material Costs for TFHX-3E Plate based on 500 lbs of Foil

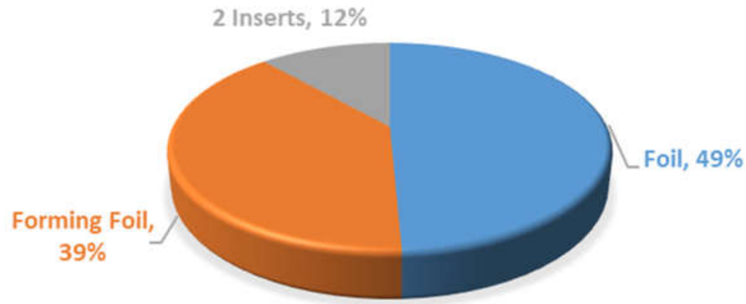

Plate Material	Qty.	Cost
Foil @ $75.18 / lb	0.28 lb	$ 20.16
Foil Forming	1	$16.00
Inserts	2	$4.74
Material cost per plate	$ 40.90	
HX area per plate	0.125 m^2	
Material cost/m^2	$ 327	

Figure 71. Breakdown of material costs for TFHX-3E plate.

3.7.6. Comparison of TFHX in OTEC Application

An analysis was conducted to compare the TFHX-3E-INT performance to previously specified heat exchangers for a 2.5 MW offshore OTEC plant. Design work for the 2.5MW OTEC plant was conducted under a prior NAVFAC contract. Using the same system design (cold water pipe, ammonia system (piping lengths, sizes, and elevations), turbine efficiency, pump efficiencies, etc.), three different comparisons of the net power production using TFHX versus previously selected heat exchangers were made. The previously selected heat exchangers were a brazed aluminum evaporator with fins on the ammonia passage side and 13,905 m^2 of heat transfer area and a titanium shell and tube condenser with twisted tubes and 13,225 m^2 of total heat transfer area. The costs for the evaporator and condenser outlined in the 2.5MW report was $561/$m^2$ and $770/$m^2$, respectively. After implementing high-speed welding operations, in-house foil forming processes, and a high-volume solution for the inserts (stamping vs injection molding), the TFHX is projected to cost < $300/$m^2$.

In the first comparison, seawater and ammonia flow rates were kept the same and TFHX area matched the previous evaporator and condenser areas. Using the TFHX, comparable net power can be produced in 1/10th the heat exchanger volume and half the cost (Table 17). Although the thermal duty was comparable, 164.6 MW vs 164 MW; the TFHX was predicted to produce higher gross power due to a better approach temperature (*even in a cross-flow configuration*) in the condenser. Cold seawater exits at 7.9°C in both condensers, but in the TFHX, the ammonia temperature is 9.8°C versus 10.1°C in the shell-and-tube condenser. A counterflow configuration is expected to further improve approach temperatures. The warm seawater pumping power through the TFHX evaporator is significantly higher than in the brazed aluminum evaporator, suggesting optimization may improve performance for a TFHX system.

Table 17. TFHX in 2.5MW OTEC plant: net power comparison for same heat exchanger area and flow conditions

	3E-INT		Mini SPAR		
	Evap	Cond	Evap	Cond	
SW GPM	244000	162000	252000	168000	
# units	9696	9221	3	3	
Total HX Area	13905	13224	13905	13225	m2
Duty	164620	159826	164000		kW
U	5.08	3.55	4.54	3.15	kW/m2/C
LMTD	2.33	3.41			C
SW dP	19.12	14.19	14.2	21	kPa
WF dP	21.50	3.19	17	1	kPa
SW Tin	25.7	4.1	25.7	4.1	C
SW Tout	23.09	7.91	23.1	7.9	C
HX Temp	21.29	9.81	21.2	10.1	C
HX Pressure	893.56	611.07	891	618	kPa
EIFS/CIFS	205	133.25	205	133	kg/s
Quality	0.65		0.65		
Turbine Pressure	877.24	613.02	873	621	kPa
Turbine dP/Efficiency	264.22	0.81	252	0.81	kPa
SW Pump Power	719.54	705.31	440	770	kW
feed/recirc Pump Power	149.41	16.19	150		kW
Gross/Net Power	4648.00	2787.54	4430	2780	kW
Plates	116352	110652			
Plate Spacing	0.001	0.001			m
Plate Height	0.56	0.56	5.5	5.84	m
Plate Width	0.25	0.25	3.8	2.7	m
Stack Depth	116.352	110.652	3.2	2.7	m
Volume	16.3	15.5	200.6	148.6	m3
Weight	16.42	15.62	81	81	tons
TFHX Cost @ $300/m2	$4.17	$3.97	$7.80	$10.18	million dollars
Total HX Cost	$8.14		$17.98		million dollars

In the second comparison, seawater and ammonia flow rates were varied to find the minimum TFHX area required to produce the same net power (Table 18). Evaporator and condenser areas were not significantly reduced (from 13,905 m^2 to 13,839 m^2 and 13,224 m^2 to 13,086 m^2, respectively). Warm seawater and cold seawater usage remained the same. Liquid ammonia flow rate increased from 205 kg/s to 210 kg/s.

Table 18. TFHX in 2.5 MW OTEC plant: minimum required TFHX area to match net power

	3E-INT		Mini SPAR		
	Evap	Cond	Evap	Cond	
SW GPM	244000	162000	252000	168000	
# units	9650	9125	3	3	
Total HX Area	13839.07	13086.16	13905	13225	m2
Duty	168539.97	163744.52	164000		kW
U	5.11	3.58	4.54	3.15	kW/m2/C
LMTD	2.38	3.49			C
SW dP	19.24	14.37	14.2	21	kPa
WF dP	21.84	3.34	17	1	kPa
SW Tin	25.7	4.1	25.7	4.1	C
SW Tout	23.03	8.01	23.1	7.9	C
HX Temp	21.20	9.95	21.2	10.1	C
HX Pressure	890.79	614.09	891	618	kPa
EIFS/CIFS	210	136.5	205	133	kg/s
Quality	0.65	0	0.65		
Turbine Pressure	874.32	616.25	873	621	kPa
Turbine dP/Efficiency	258.06	0.81	252	0.81	kPa
SW Pump Power	722.22	707.96	440	770	kW
feed/recirc Pump Power	151.38	17.14	150		kW
Gross/Net Power	4648.97	2780.27	4430	2780	kW

Plates	115800	109500			
Plate Spacing	0.001	0.001			m
Plate Height	0.56	0.56	5.5	5.84	m
Plate Width	0.25	0.25	3.8	2.7	m
Stack Depth	115.8	109.5	3.2	2.7	m
Volume	16.212	15.33	200.64	148.6098989	m3
Weight	16.34	15.45	81	81	tons
TFHX Cost @ $300/m2	$4.15	$3.93	$7.80	$10.18	million dollars
Total HX Cost	$8.08		$17.98		million dollars

Finally, for the same seawater flow rates, substantial improvements to net power can be achieved by adding TFHX area (Figure 72). TFHX area was allowed to increase to ~2X the original heat exchanger area (thus keeping costs comparable) and ammonia flow rates were varied to maximize net power. Net power production is projected to increase by 35% (from 2.78 MW to 3.56 MW) by doubling TFHX area (Table 19). A study weighing the increased revenue from higher net power production (or savings due to decreased fuel usage) versus the additional $10 million in capital investment for additional heat exchanger area would be required to determine the optimal size.

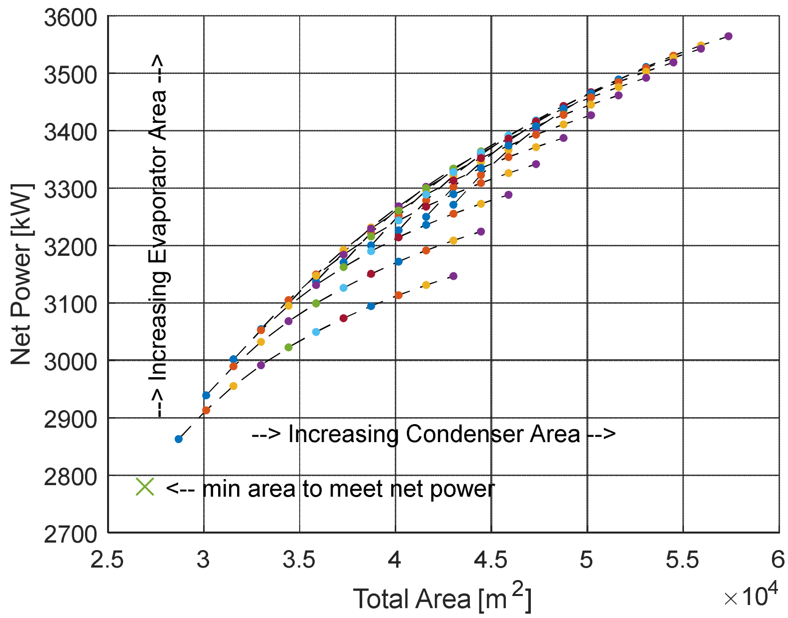

Figure 72. For fixed seawater flow rate, net power continues to increase with increasing TFHX area. Dashed lines show fixed evaporator area and increasing condenser area. Colored dots show fixed condenser area and increasing evaporator area.

With performance improvements and significant cost reduction in the 3E-INT design and introduction of the HSWS, the TFHX can provide a viable heat exchanger solution for an OTEC system. The reduced volume and weight of TFHXs compared to existing heat exchangers also enable a smaller, less expensive OTEC plant.

Table 19. TFHX in 2.5 MW OTEC plant: comparison of net power for comparable heat exchanger cost.

	3E-INT1		Mini SPAR		
	Evap	Cond	Evap	Cond	
SW GPM	244000	162000	252000	168000	*same mass flow rate
# units	20000	20000	3	3	
Total HX Area	28682	28682	13905	13225	m2
Duty	180594	175369	164000		kW
U	2.8	1.9	4.54	3.15	kW/m2/C
LMTD	2.2	3.2			C
SW dP	7.7	5.8	14.2	21	kPa
WF dP	16.3	1.3	17	1	kPa
SW Tin	25.7	4.1	25.7	4.1	C
SW Tout	22.8	8.3	23.1	7.9	C
HX Temp	21.3	9.9	21.2	10.1	C
HX Pressure	894.7	612.1	891	618	kPa
EIFS/CIFS	225	146.25	205	133	kg/s
Quality	0.65	0	0.65		
Turbine Pressure	877.7	615.0	873	621	kPa
Turbine dP/Efficiency	262.7	0.8	252	0.81	kPa
SW Pump Power	467.6	582.8	440	770	kW
feed/recirc Pump Power	162.1	16.4	150		kW
Gross/Net Power	5063.4	3564.5	4430	2780	kW
Plates	240000	240000			
Plate Spacing	0.001	0.001			m
Plate Height	0.25	0.25	5.5	5.84	m
Plate Width	0.25	0.25	3.8	2.7	m
Stack Depth	240	240	3.2	2.7	m
Volume	15	15	200.64	148.61	m3
Weight	15.12	15.12	81	81	tons
TFHX Cost @ $300/m2	$8.60	$8.60	$7.80	$10.18	million dollars
Total HX Cost	$17.21		$17.98		million dollars

3.8. BIOFOULING EFFECTS

The TFHX-3C-3 was used in long-term biofouling testing at the conclusion of performance testing. The TFHX-3C test housing contains an acrylic cover so the plates can be seen but also exposes the plates to sunlight. The TFHX-3C-3 was operated as an evaporator at a seawater flow rate corresponding to 1 m/s (Reynolds number = 1550). The ammonia flow rate was set at 0.048 kg/s, which was found to be a stable flow rate to maintain during performance testing. The moderate testing velocity and decision to maintain exposure to sunlight were chosen to accelerate biofouling.

Prior to biofouling testing, TFHX-3C-3 was switched several times between condenser and evaporator operations and the seawater velocities were varied from 0.1 – 3 m/s. No significant biofouling was observed on the surface of the plate although some material appeared on the inlet edge of the 18 plates after one week.

The biofouling test was started on April 5, 2019 and continued until May 6, 2019. Data was continuously recorded and pictures of the outermost plate were also taken. A layer of brown growth, presumably algae, covered the plate only 7 days into the start of the biofouling test. Two weeks later, thicker coverage was observed in discrete locations, as indicated by darker patches. At the end of the test, the areas of thicker biofouling continued to expand across the plate.

In terms of performance, the seawater dP nearly doubled but U value decreased only 5% (Figure 74).

It is likely that the biofouling on the outermost plate, directly exposed to sunlight, was not typical of the remaining 17 plates. The bulk of the increase in seawater dP is most likely due to buildup on the inlet edges of the plates, not constriction of the seawater channels.

This test was designed to accelerate biofouling and identify whether the effects could be identified in heat exchanger performance. Seawater dP was more sensitive to biofouling and it would be more effective to base the timing of treatments on increases seawater dP rather than decreases in U Value. An opaque housing should also delay the development of biofouling.

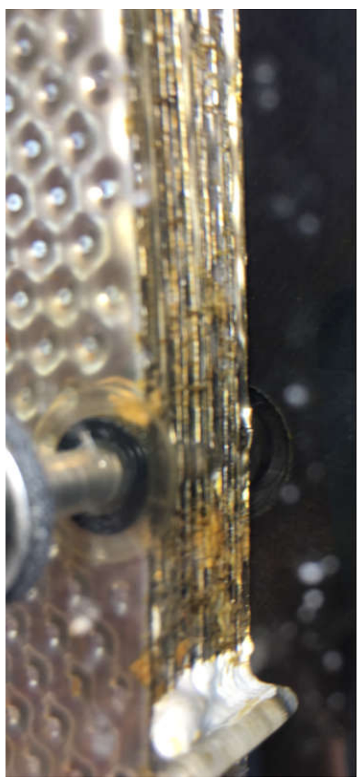

Figure 73. Biofouling on the inlet edge of the 18-plates after 1 week of performance testing.

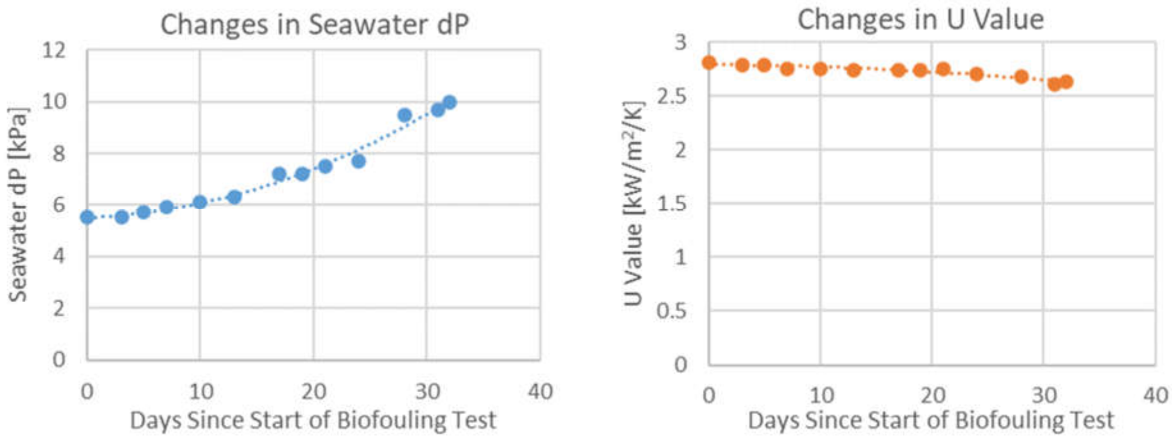

Figure 74. Biofouling-induced changes in TFHX-3C-3 performance.

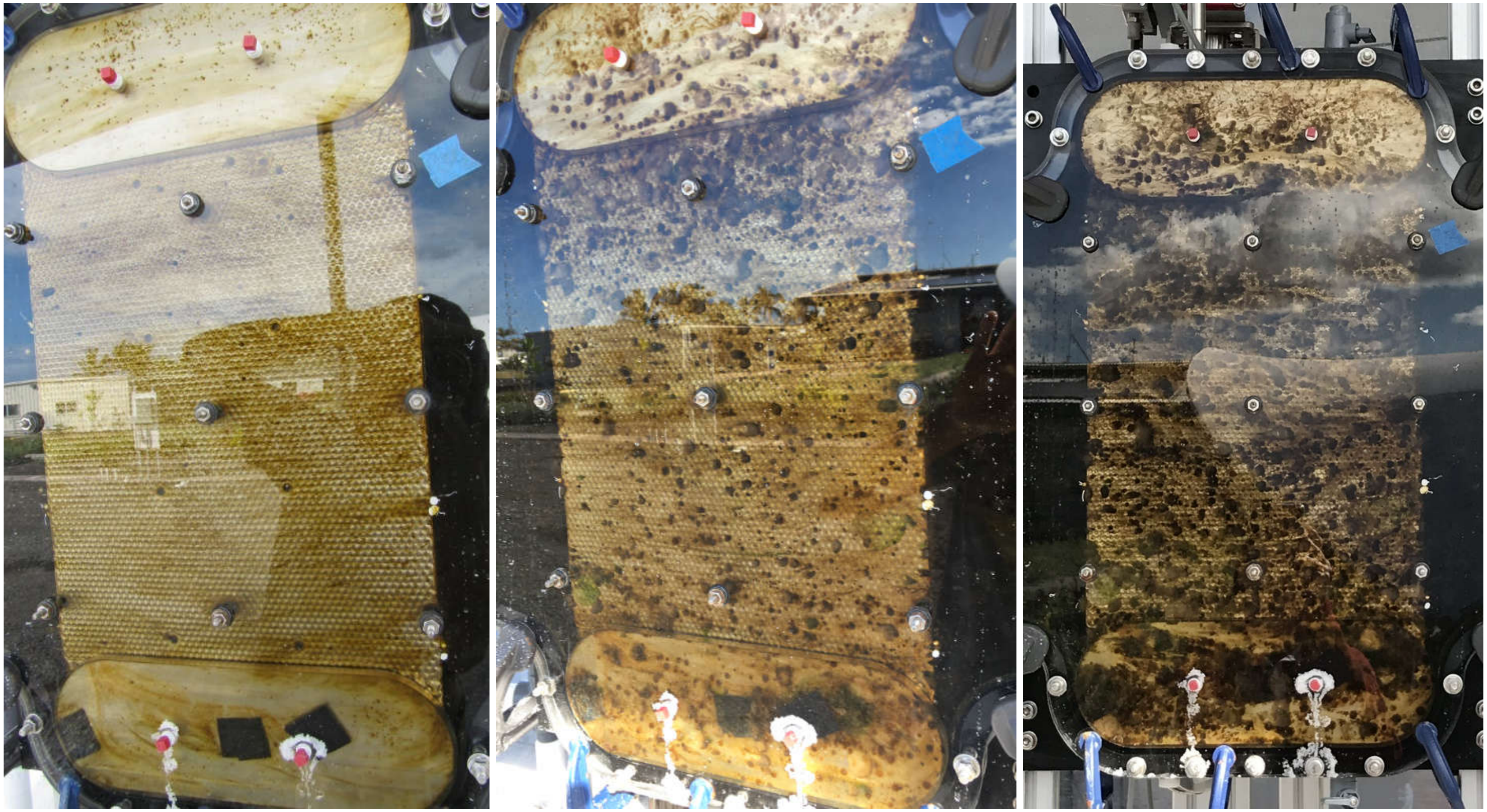

Figure 75. Biofouling coverage after 7 days, 21 days, and 32 days.

3.9. SUMMARY

Makai tested four crossflow ammonia-seawater heat exchangers. The most compact versions, TFHX-3C-3 and TFHX-3E-INT1, had over 700 m^2/m^3 of heat transfer area, which is over 5X the volumetric density compared to previously tested plate-frame, brazed fin, or shell-and-tube heat exchangers.

TFHX performance was compared to the previously tested heat exchangers by scaling the TFHXs to 2MW duty at the same energy density and comparing the seawater and ammonia convective coefficients, overall heat transfer coefficient, and approach temperatures for the same seawater pumping power or energy density. For the same seawater pumping power, seawater-side convective coefficients were higher in the TFHXs with the larger seawater channels; only TFHX-3C-1 and TFHX-3B-2 had seawater convective coefficients comparable to or higher than the previously tested heat exchangers. For the same energy density, the ammonia-side convective coefficients of all TFHXs were higher than (for some conditions, over twice as high as) the previously tested heat exchangers.

The significant improvement in ammonia-side convective coefficients resulted in comparable or higher overall heat transfer coefficients for all TFHXs compared to previously tested heat exchangers, except for BAHX3. Compared to BAHX3, the most compact TFHXs (3C-3 and 3E-INT1) had higher pumping powers due to the small seawater channels.

For the same duty, energy density, and seawater pumping power through the heat exchanger, 3C-1 and 3C-2 had the lowest approach temperature. 3E-INT1 and 3B-2 had comparable approach temperatures and while higher than 3C-1 and 3C-2, were about the same as the previously tested heat exchangers. TFHXs had tight approach temperatures even in a crossflow configuration. A counterflow configuration is predicted to have even better approach temperature.

The TFHX can provide the same or better performance, i.e., the same duty at comparable (or better) ammonia-side operating pressures using comparable (or lower) seawater pumping powers, in a fraction of the volume of existing heat exchangers. After implementing the High-Speed Welding Station, TFHXs are also projected to cost less per m^2 of heat transfer area compared to existing heat exchangers. In the 2.5 MW Mini Spar OTEC application, TFHXs can match the previously predicted performance at half the cost. Alternatively, for the same cost as previously specified heat exchangers, utilizing the TFHXs can provide up to 28% increase in net power production.

4. CROSSFLOW TFHX: AIR-WATER HEAT EXCHANGER TESTING

With thin foils, customizable geometries, and high compactness, the TFHX has the potential to provide substantial performance improvement over existing air-cooled heat exchangers. Makai constructed and tested 13 air-water TFHX configurations (Table 20). The goal of testing was to determine the air-side pressure drop and the air-side convective coefficients for a range of air flow velocities.

Table 20. Summary of tested TFHX air-water configurations

	TFAC-3C-1	TFAC-3C-2	TFAC-3C-3	TFAC-3C-4	TFAC-3C-5
Water-side Spacing [mm]	0.6	0.6	0.3	0.3	0.3
Air-side Spacing [mm]	0.68	0.41	0.51	0.69	0.95
HX Area [m^2]	0.0183	0.0228	0.0278	0.0232	0.0186
# of plates	4	5	6	5	4

	TFAC-3E-1	TFAC-3E-2 & TFAC-3E-9	TFAC-3E-3 & TFAC-3E-6	TFAC-3E-4 & TFAC-3E-7	TFAC-3E-5
Water-side Spacing [mm]	0.22	0.22	0.22	0.22	0.22
Air-side Spacing [mm]	0.36	0.59	1.03	0.46	0.77
HX Area [m^2]	0.0375	0.0281	0.0187	0.0328	0.0234
# of plates	8	6	4	7	5

4.1. TEST SETUP

In air convection testing, test plates are installed in an air convection test housing with connections for water to be pumped through the internal channels of the test plates and air ducted to flow between the plates (external channels). The water is heated with heating elements to 50°C. The air convection testing was performed in Michigan in 2018 and again in Kona in 2019. In the Michigan setup, air flow was provided by a blower or air compressor and the air velocity was measured at the exit of the test using anemometers. In Kona, the air flow was provided by a blower and air mass flow rate was measured using a Coriolis flow meter. Temperature and pressure sensors measured the air and water inlet and outlet conditions.

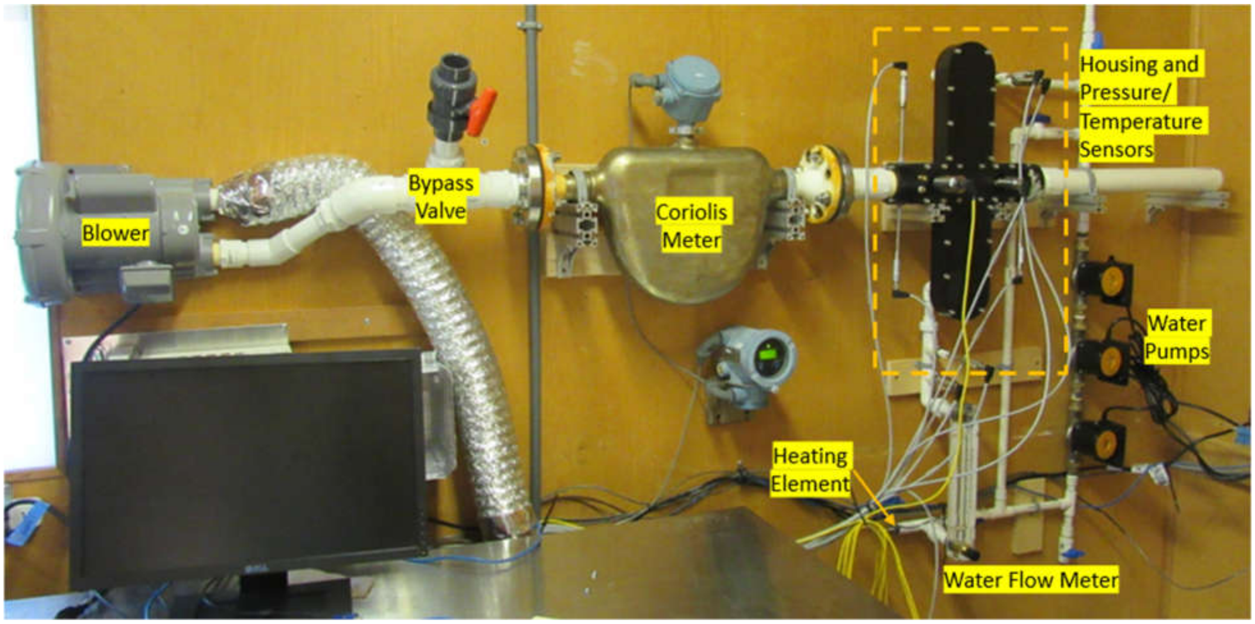

Figure 76. Air convection test setup.

An air convection test housing (Figure 77) was designed such that changing the number of plates stacked in the housing changed the effective air channel spacing from 0.3 to 1.0 mm. The air flow duct width was 6 mm. 3D printed spacers were used to hold the spacing between plates in the test section (Figure 78). Although each plate is 100 mm wide by 460 mm long, the test section only occupies a 50 mm x 50 mm section in the middle of the plate (Figure 79). 3C and 3E-style plates were used in testing but the overall plate shape and test area remained the same. A new housing was purchased when switching over to testing the 3E style plates to accommodate the 3E o-ring grooves.

A test point is defined by specifying the air- and water-side flow rate. The water-side flow rate is set first and different air-side flow rates are tested for the fixed water-side flow rate. The process is repeated for each new water-side flow rate using the same air-side flow rates. Air-side flow rates were selected to produce up 0-1 psi pressure drop, but were limited by the capacity of the blower, particularly at larger air channel spacings; for the 4-plate configurations, only pressure drops of ~ 0.5 psi could be attained. Approximately one hour of data was collected for each test point.

Summarized data points were then obtained by reviewing the test point and selecting a span of data that was representative of steady-state conditions. This was typically the last 5 minutes of a test point. Measurements were then averaged over the selected stable span. Detailed description of calculations and data processing are included in Appendix B.

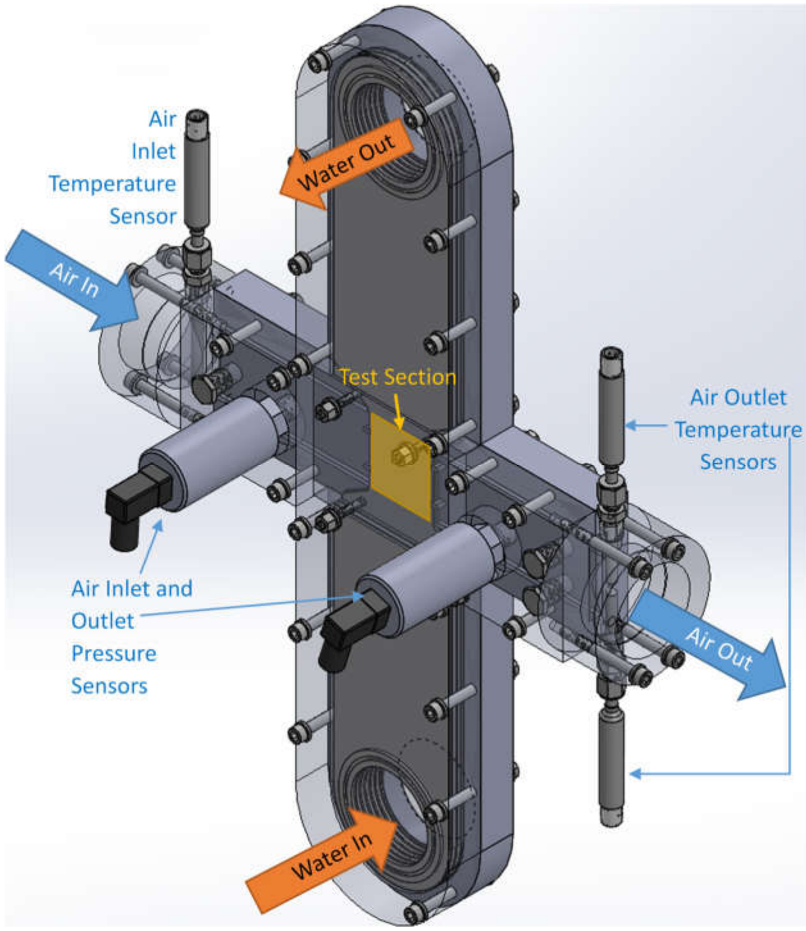

Figure 77. Apparatus used to experimentally determine air-side heat transfer coefficients

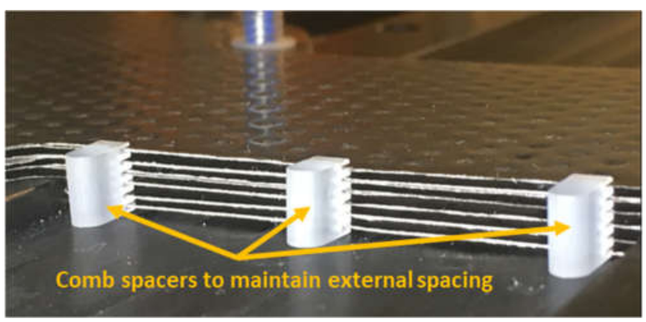

Figure 78. 3D printed comb spacers used to maintain air channel spacing.

Figure 79. Air-water test plate with 50 mm x 50 mm test section.

4.2. AIR-SIDE PRESSURE DROP

The air-side pressure drop limits the air channel spacing (compactness) and air velocity (performance). In some applications the air pressure drop is proportional to the available air mass flow rate; i.e., higher pressure drops mean lower available mass flow rate, and therefore, lower overall duty. TFHX design factors that affect the air pressure drop include the air channel spacing, the internal channel spacing, and the orientation that the TFHX plates are stacked together.

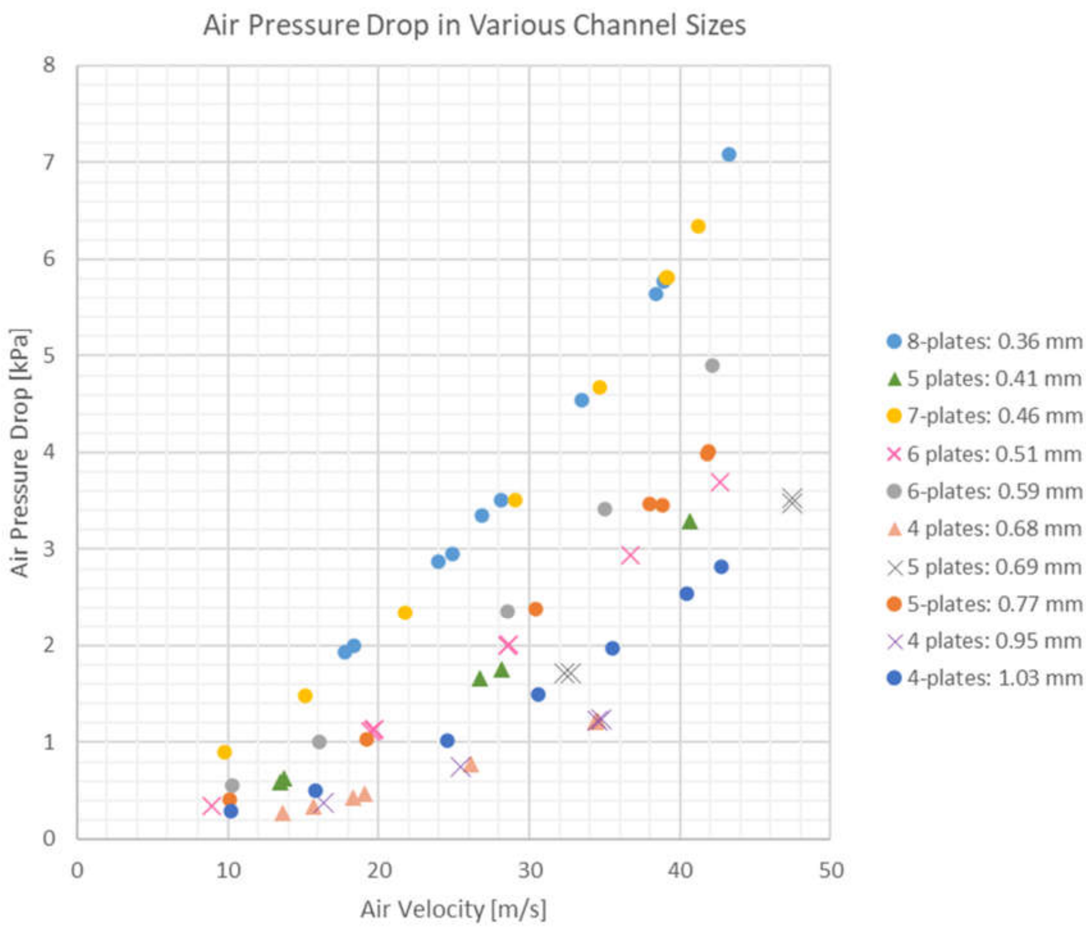

Figure 80. Air pressure drop for various channel sizes, stacking orientations, and internal channel spacings.

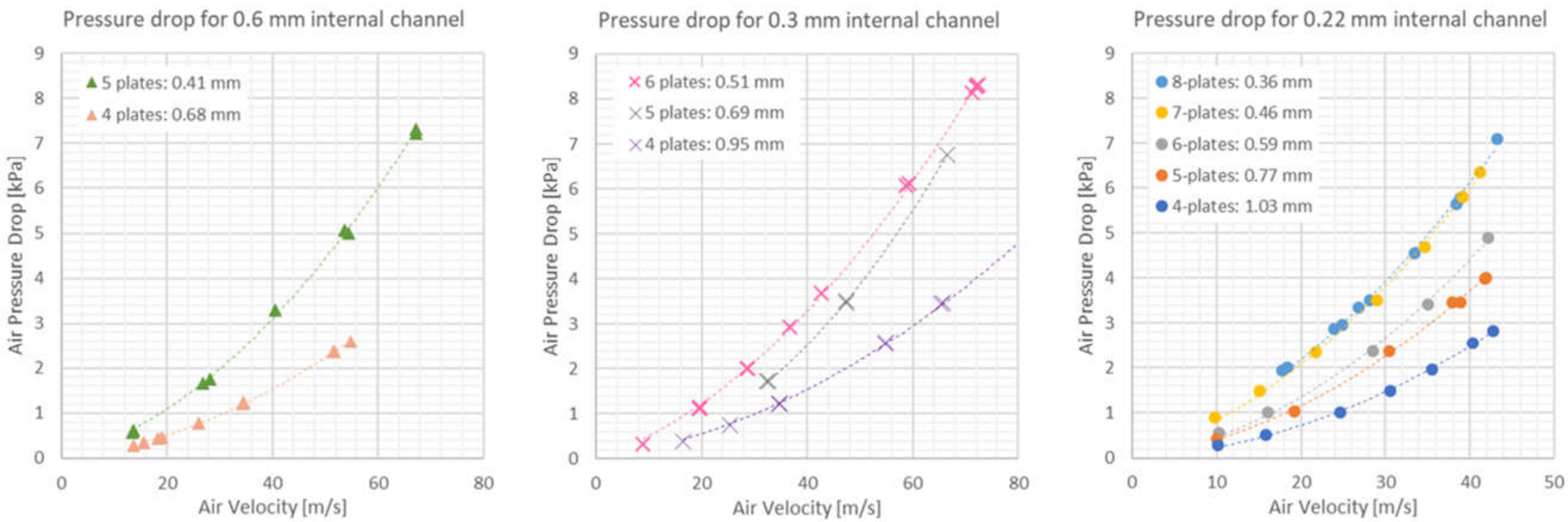

Figure 81. Air pressure drop for plates with the same orientation and internal channel spacing.

The 3C plates (circle symbols) were installed in a stacked orientation (weld over weld). In the stacked orientation, the local air channel spacing is more variable; the channel is largest where the welds overlap and smallest where the maximum internal channel heights overlap. For a 0.36 mm effective air channel, the maximum spacing is 0.58 mm and the smallest spacing is 0.14 mm. The 3E plates were installed in a staggered orientation. While the air channel is also non-uniform, there is less difference between the maximum and minimum spacing.

The 3E plates all had the same internal channel spacing of 0.22 mm. The 3C plates had internal channel spacing of 0.6 mm (triangles) and 0.3 mm (x's). The shape of the internal channel is also different with each height; different weld spacings were used to fabricate each internal channel spacing.

These geometrical differences make comparison of the pressure drop data across different internal channel spacings difficult and potentially misleading. Based on the current data, we verified that smaller air channels have higher pressure drops for the same velocity. Also, at the same velocity, smaller staggered channels have lower pressure drop than larger stacked channels. For the staggered orientation, the smaller air channels with larger internal channels had comparable pressure drop to a larger air channel with smaller internal channels. This result was unexpected.

4.3. AIR-SIDE CONVECTIVE COEFFICIENT

In most applications, the air-side convective coefficient is significantly lower than the convective coefficient of the accompanying heat transfer fluid. A detailed discussion on the calculation of the air-side convective coefficient can be found in Section 10.2.5.

In general, larger channels had higher air convective coefficients at the same velocity (Figure 82). For comparable air channel spacings, the plates with the 0.22 mm and 0.3 mm internal channel spacings had higher convective coefficients than the plates with the 0.6 mm internal channel spacing.

When air convective coefficient is plotted versus pressure drop, the staggered orientation plates with smaller air channel spacings had higher convective coefficients for the same pressure drop (Figure 83). Staggered plates with a comparable air channel spacing (0.68 mm) and smaller internal channel spacing (0.3 mm vs 0.6 mm) had higher air convective coefficient for the same pressure drop.

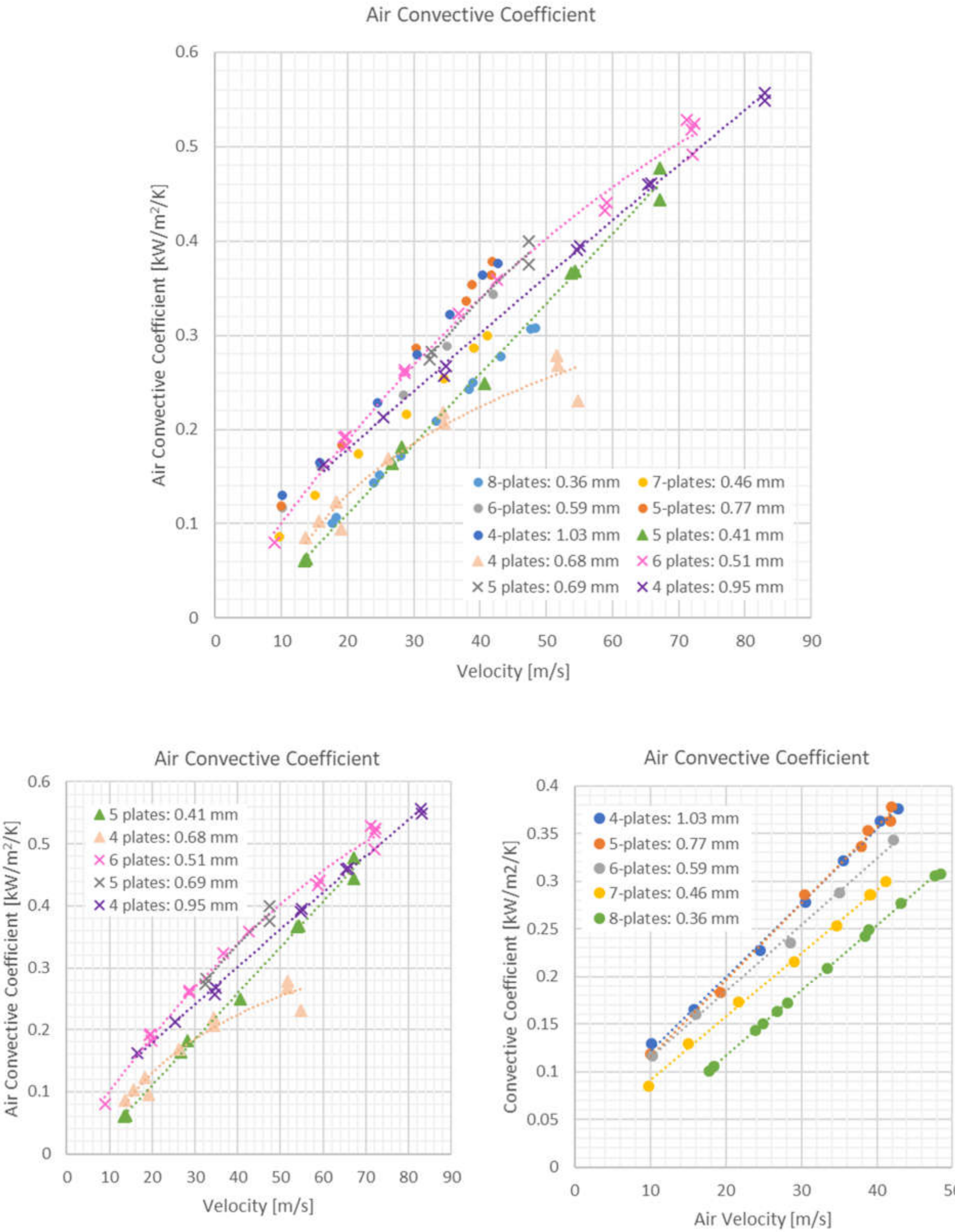

Figure 82. Air convective coefficient versus air velocity. All data is shown together on the top graph. The lower left graph has data from the TFHX-3C tests and the lower right graph has data from TFHX-3E tests.

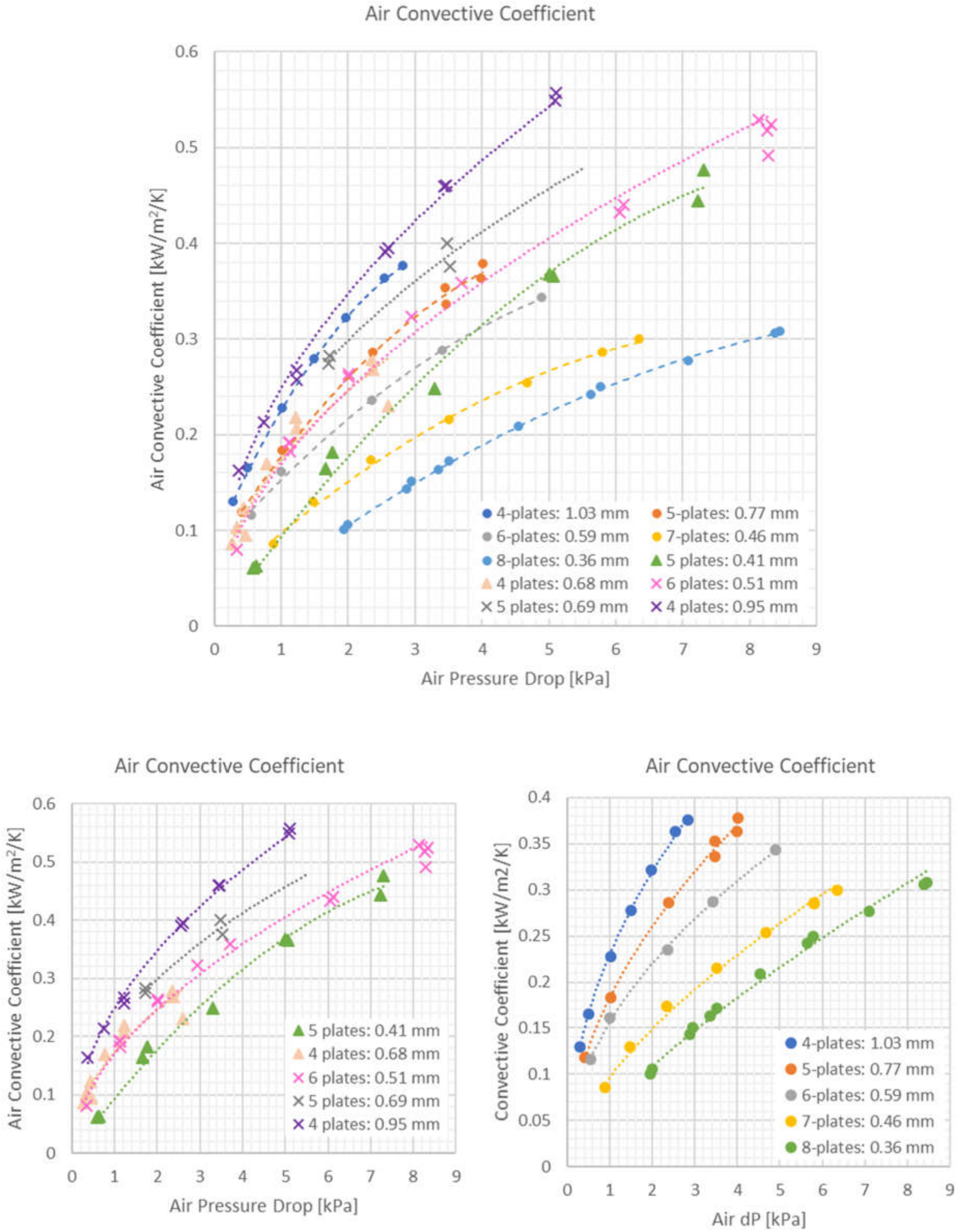

Figure 83. Air convective coefficient versus air pressure drop. All data is shown together on the top graph. The lower left graph has data from the TFHX-3C tests and the lower right graph has data from TFHX-3E tests

4.4. SUMMARY

There are some inconsistencies in the data collected which Makai has attributed to inaccurate plate spacings and the effect of environmental losses. With regards to plate spacing, plates were designed to be compressed in the test section to attain the required air channel size. However, squeezing the plates together introduced either a concave or convex shape in the plates (most severe in the outermost plates and in varying degrees for the middle plates). Even with spacers at four locations, some channels appeared differently spaced. Since a maximum of 8 plates were installed at a time, any bias in a single channel can have a significant impact on the overall test. Additionally, because the test section was small and 4-8 plates were used, the total duty for these tests was less than 250 W, with many points around 100 W. Bias in instrumentation in addition to heat loss (from the hot water) to the lab comprise a more significant percentage of duty.

Makai has already re-designed the next air-convection testing apparatus to utilize a larger test section and hold up to 32 plates. With these improvements, our initial air pressure drop and convective coefficient measurements can be verified.

For most applications, the optimal TFHX design accounts for the allowable pressure drop and required duty. Larger air channels have high air convective coefficients and low pressure drops but fewer plates (and therefore less heat transfer area) can be fit into a fixed volume. Depending on the conditions and application, for the same pressure drop, the overall duty of a TFHX with high air convection coefficients but fewer plates may be lower than a TFHX with lower air convection coefficients with more plates. An application-specific optimization is necessary to yield the best performing TFHX.

5. COUNTERFLOW TFHX: SEAWATER-SEAWATER HEAT EXCHANGER PERFORMANCE TESTING

The TFHX is fabricated from corrosion resistant titanium foil, making it an attractive option for seawater applications other than OTEC. In seawater air-conditioning or cooling applications, heat transfer regime is single phase, liquid-to-liquid. The thermal and hydraulic properties of the internal and external fluids are closely matched; the customizability of the internal and external channel spacings in the TFHX can provide performance improvements not realized in off-the-shelf heat exchangers.

5.1. TEST SETUP

Four single-plate and one 12-plate seawater-seawater heat exchangers were tested between August 2018 and November 2018. The heat exchanger plates were built using the TFHX-3C manifolds and the overall plate is shaped like a parallelogram (Figure 84). Both single and 12-plate heat exchangers were tested in the counter flow configuration, with cold seawater flowing upwards on the inside of the plates and warm seawater flowing downwards between plates. Dimensions for the tested heat exchangers are summarized in Table 21.

.

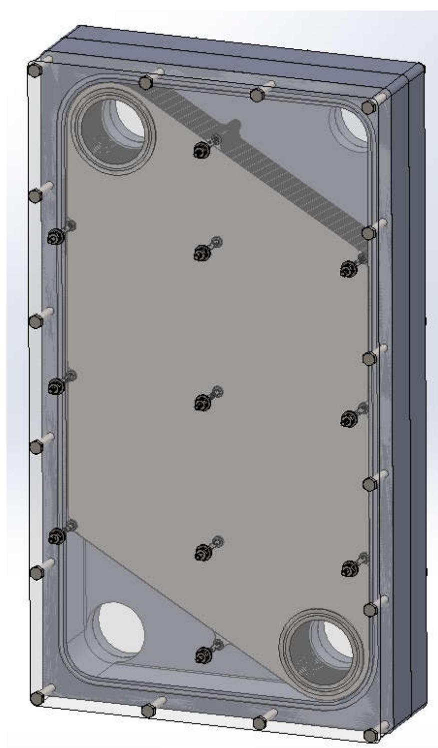

Figure 84. Seawater-seawater test plates and housing.

Table 21. Summary of seawater-seawater heat exchanger parameters.

	TFSW-1	TFSW-2	TFSW-3	TFSW-5	TFSW-6
Internal (CSW) spacing [mm]	2.27	1.14	0.72	1.5	1.51
External (WSW) spacing [mm]	1.29	1.86	2.07	1.68	2.25
Heat Transfer Area [m^2]	0.2070	0.2121	0.1905	0.2064	2.47 (12 plates)
Passage Length [m]	0.46	0.46	0.46	0.46	0.46
Plate Width [m]	0.285	0.285	0.285	0.285	0.285

5.2. SINGLE PLATE TESTS

Each heat exchanger was tested at 16-25 points by varying cold and warm seawater flow rates. For the single plate tests, seawater flow rates and temperatures were measured for both cold and warm seawater but only cold seawater pressure drop was measured.[2] For comparison, the internal (cold seawater) side is plotted versus pumping power (volumetric flow rate x pressure drop) and the external (warm seawater) side is plotted versus velocity (volumetric flow rate / cross-sectional flow area).

The main focus of the single plate tests was to determine the effect of the internal passage size on performance; the 12-plate test used the best-performing single plate to further evaluate performance in more representative heat exchanger configuration.

5.2.1. Pressure Drop

The measured cold seawater pressure drop plotted versus cold seawater velocity yielded inconsistent results. For the same velocity, a smaller channel should have a higher pressure drop compared to a larger channel. TFSW-3 had the smallest internal channel spacing and the highest pressure drop but TFSW-1, which had the largest internal channel, had pressure drops almost as high as TFSW-3. TFSW-2, which had a smaller channel than TFSW-5, had consistently lower pressure drops.

The most likely explanation is that since the internal channels were visually observed to deform with changes in warm and cold seawater flow, the actual channel spacing tested was different from the designed channel spacing. The combination of the foil thickness, pattern weld design, and forming parameter did not produce a plate that was stiff enough to resist deformation with changes internal/external pressure induced by changes in flow rates.

---

[2] Warm seawater side pressure drop was measured separately for TFSW-3C-5 by removing the pressure sensors from the cold seawater side and recording the pressure drop for different warm seawater flow rates. Cold seawater was kept at a constant flow rate.

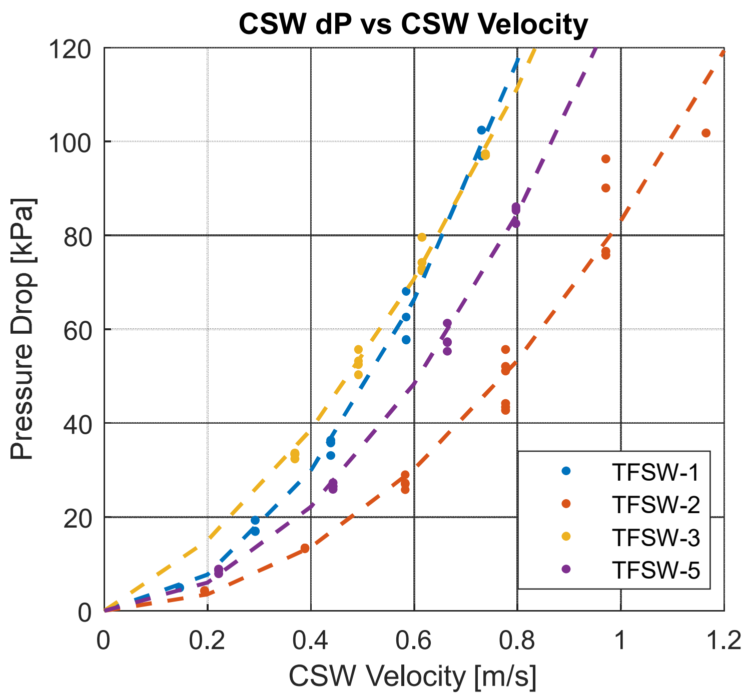

Figure 85. Cold seawater pressure drop versus cold seawater velocity for single-plate tests. The pressure drop data are inconsistent; at the same velocity, the largest internal channel had pressure drops comparable to the smallest internal channel.

5.2.2. Overall Heat Transfer Coefficient

Unlike seawater-ammonia testing, duties were not controlled and depended on both internal and external flow rates (Figure 86). In previous testing, the overall heat transfer coefficient was dominated by the external fluid flow rate (seawater or air); in seawater-seawater testing, U-value is dependent on both internal and external flow rates (Figure 87). U-values are plotted versus internal/external velocities because an unbiased comparison would require scaling up each individual data point to match duty and the resulting U-value would have to be plotted versus the combined pumping power (which was not possible without pressure drop measurement on the warm seawater side).

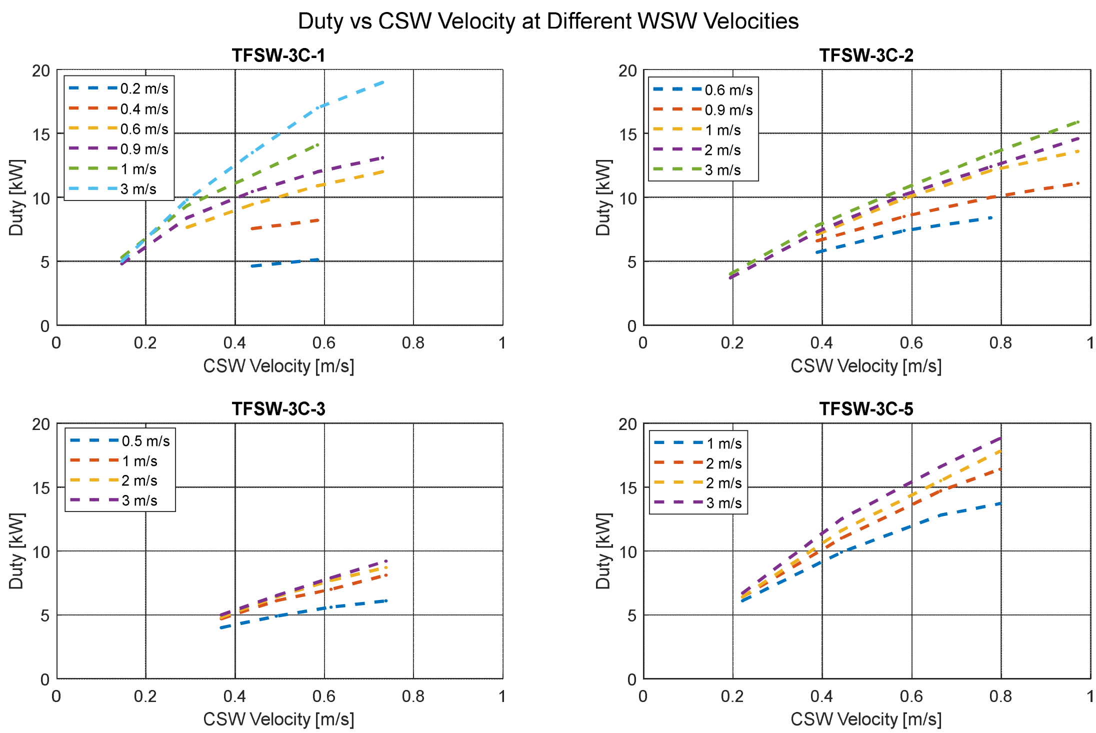

Figure 86. Variation in duty at the test points.

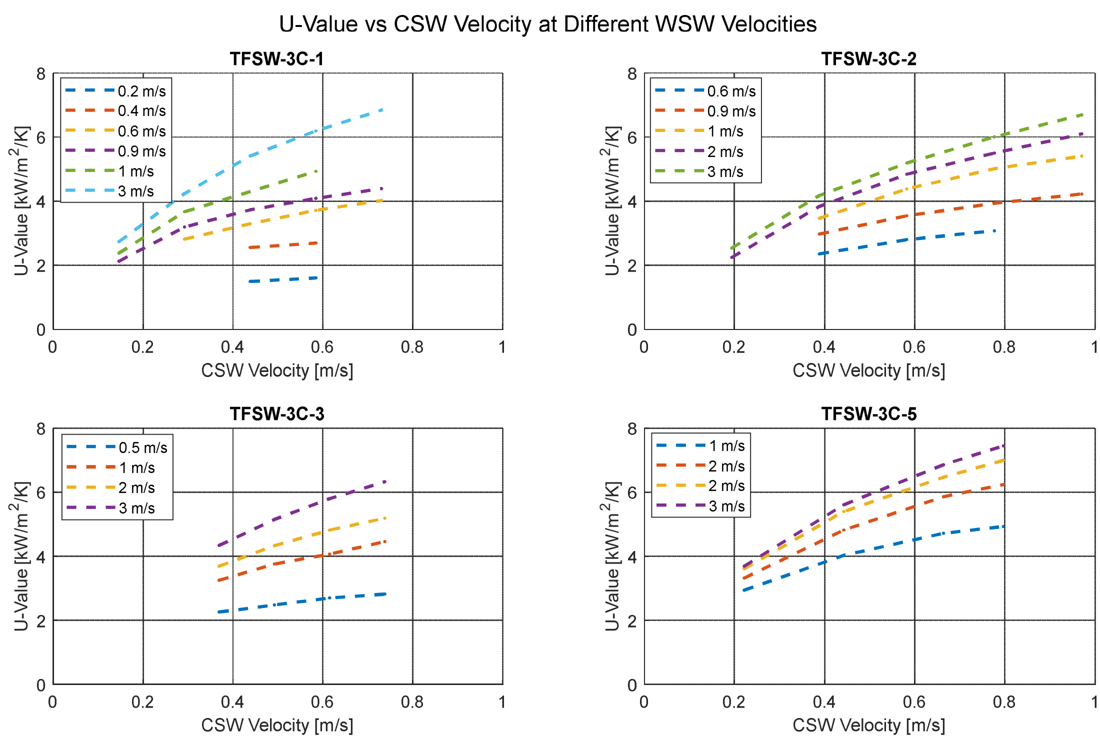

Figure 87. Overall heat transfer coefficients in the single plate tests.

5.2.3. Convective Coefficients

Convective coefficients were calculated from all available data points using a constrained least-squares solver, where the lower bound for the convective coefficients is 0. Similar to U-value results, seawater convective coefficients are plotted versus velocity due duty scaling issues and lack of pressure drop data.

For the same velocity, larger channels were previously observed to have higher convective coefficients, but this trend was not observed in the single-plate tests. At the same velocity, TFSW-2 had the lowest pressure drop (Figure 85), implying a larger channel, but also the lowest convective coefficient (Figure 88). However, TFSW-1,-3, and -5 results roughly follow previous trends.

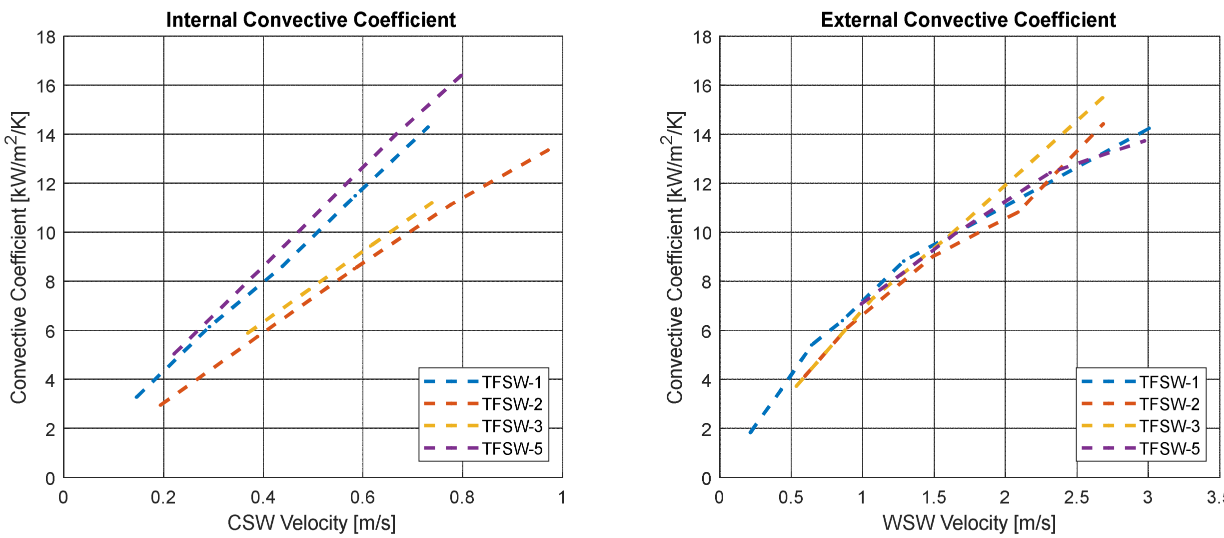

Figure 88. Singe plate test internal and external convective coefficients.

5.2.4. Discussion

Two factors made it difficult to draw conclusions from the test results. The internal passages were visually observed to change shape when the pressure difference between the warm and cold seawater side changed. The internal passage was smallest for points at high cold seawater velocities and low warm seawater velocities and largest for test points at low cold seawater velocities and high warm seawater velocities. This means each test point was conducted on a slightly different plate. The amount of deformation also varied from plate to plate; TFSW-1, with the largest internal passages likely experienced the most deformation whereas TFSW-3, with the smallest internal passages, experienced less extreme deformation.

In the single plate test, changing the internal passage also changed the external passage. Since the U-value was sensitive to changes in both warm and cold seawater flow rates, it was not possible to isolate performance changes due to changes in the internal effective spacing (because the external effective spacing changed too).

5.3. 12-PLATE TEST

The single-plate test data indicated TFSW-5 had the highest U values and cold seawater convective coefficients. For the 12-plate test, TFSW-6 utilized the same internal effective spacing of 1.5 mm. Since the plate spacing for the 3C-type heat exchangers is 3.89 mm (based on the manifold, foil, and pill spacer thicknesses), the external effective spacing was 2.252 mm. The internal pressure drop and convective coefficient should match TFSW-5. The external effective spacing was larger than any of the single-plate test configurations; TFSW-3 was the closest at 2.066 mm. TFSW-6 was tested at 24 points (Table 22).

Table 22. Test points for TFSW-6

		CSW GPM					
		10	20	30	40	50	60
WSW GPM	50	x	x	x	x	x	x
	75	x	x	x	x	x	x
	100	x	x	x	x	x	x
	125	x	x	x	x	x	x

5.3.1. <u>Pressure Drop</u>

Internal pressure drop was higher in the TFSW-6 compared to TFSW-5 (Figure 89). Although the designed internal channel spacing was the same, the actual internal channel spacing was likely smaller than intended in TFSW-6 due to higher warm seawater pressure. In TFSW-5, the warm seawater effective spacing was smaller and higher warm seawater velocities were tested; both factors contribute to a higher warm seawater side pressure drop and lower overall warm seawater pressure.

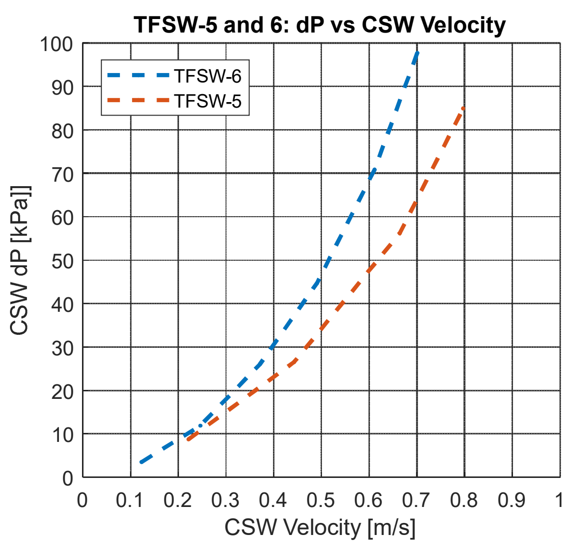

Figure 89. Internal pressure drop for TFSW-5 and TFSW-6.

5.3.2. Overall Heat Transfer Coefficient

The duty and overall heat transfer coefficient varied with both warm and cold seawater flow rates (Figure 90).

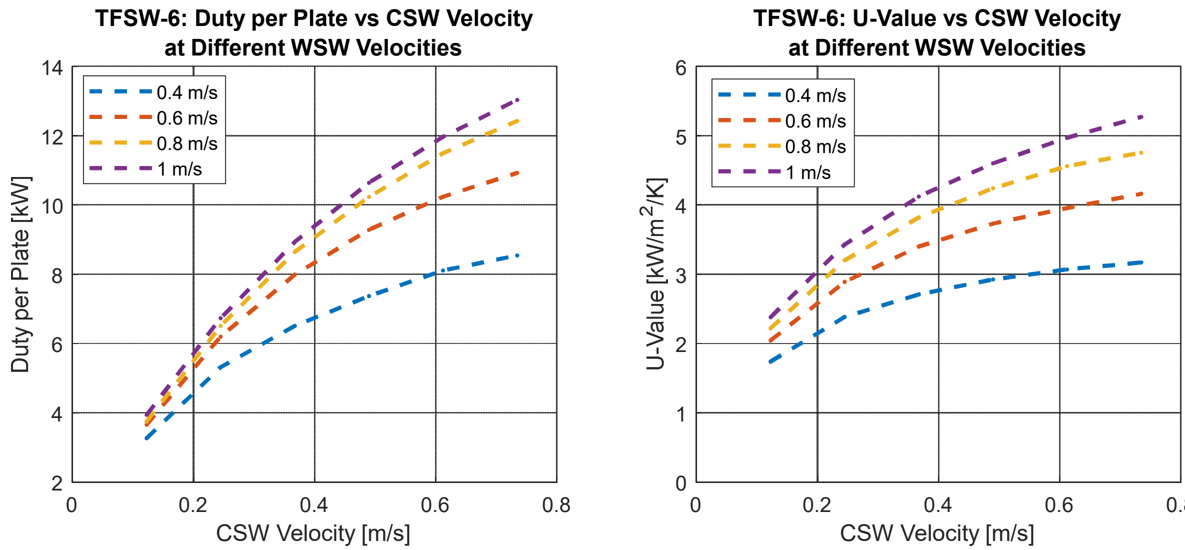

Figure 90. TFSW-6 Duty and U-value vs CSW velocity for different warm seawater velocities.

5.3.1. Convective Coefficients

The convective coefficients for TFSW-6 are in agreement with the coefficients obtained from the single-plate tests (Figure 91). Using the convective coefficients, the re-calculated U values were within 3.5% of the measured U values.

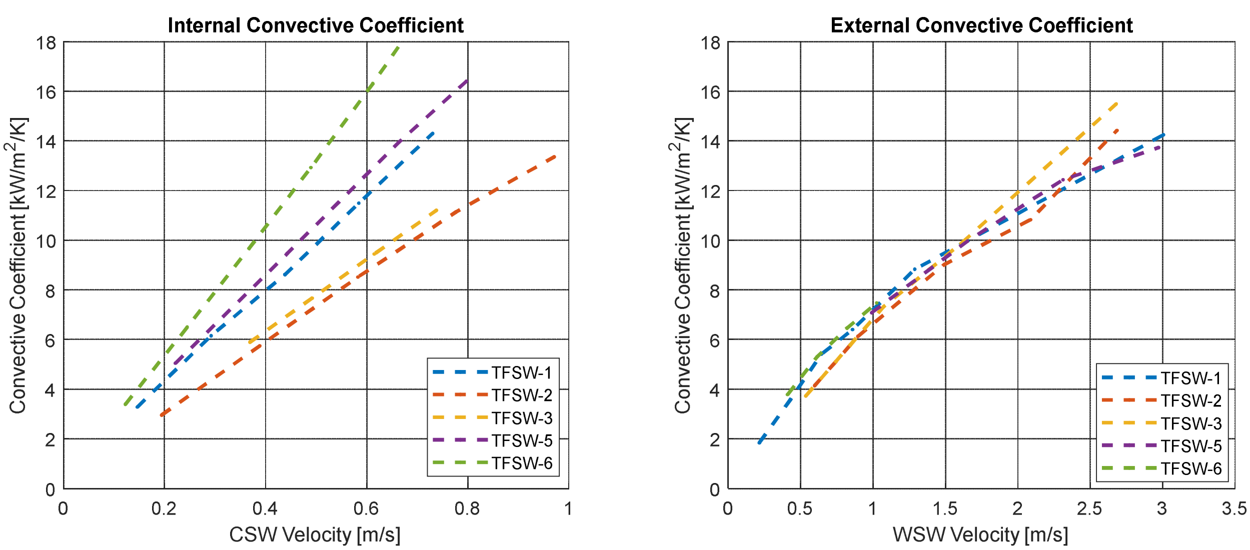

Figure 91. TFSW-6 convective coefficients compared to convective coefficients from single plate tests.

5.3.2. Approach Temperature

Another consideration in the design of seawater-seawater heat exchangers is the approach temperature (warm seawater inlet temperature – cold seawater outlet temperature). The most efficient design would meet both pressure drop and duty requirements while having cold seawater exit as close to the warm seawater temperature as possible, extracting as much cooling capacity from the cold seawater as possible. For a fixed heat exchanger, this can be accomplished by varying the water flow rates (Figure 92). Alternatively, in the design process, the cold seawater passages can be made smaller and/or longer.

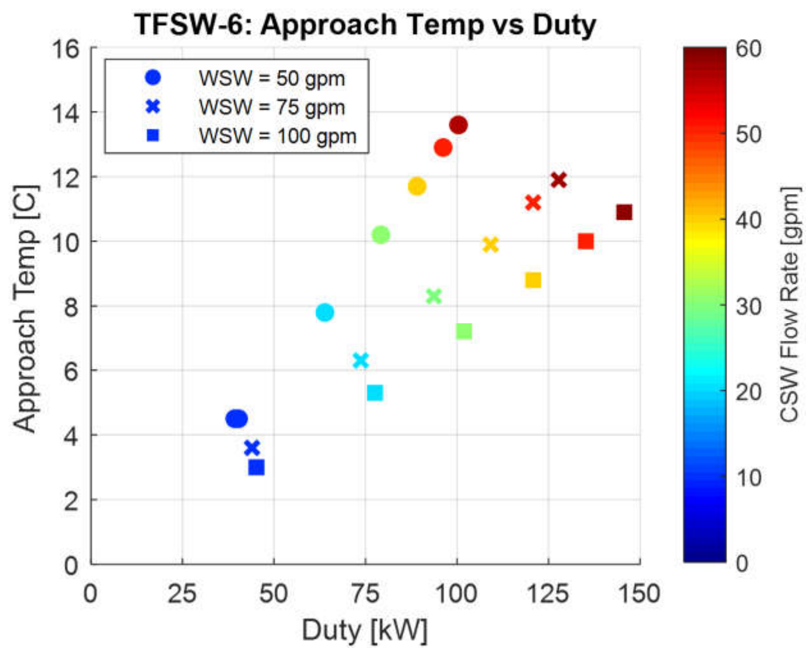

Figure 92. Approach temperature variation with duty and warm seawater flow rate.

5.3.3. Discussion

Direct comparison of U-values and convective coefficients with single plate test results is difficult because each internal/external flow rate combination would have to be scaled up to matching duties before comparing the U-value vs seawater pumping power.

However, since the internal channels of TFSW-5 and TFSW-6 are comparable, it is useful to compare the U-values vs cold seawater velocities for the same warm seawater velocity. Compared to TFSW-5, TFSW-6 had comparable duty but the U-value was up to 10% higher (Figure 93). The improvement in U-value may be an artifact of the uncertainty in the actual internal effective spacing. Since the pressure drop was higher in TFSW-6, this suggests a smaller internal effective spacing, which would result in higher velocities than calculated based on the intended effective spacing. If the channel spacing in TFSW-6 were 1.25 mm instead of 1.5 mm, the dP vs velocity and U vs velocity would match TFSW-5.

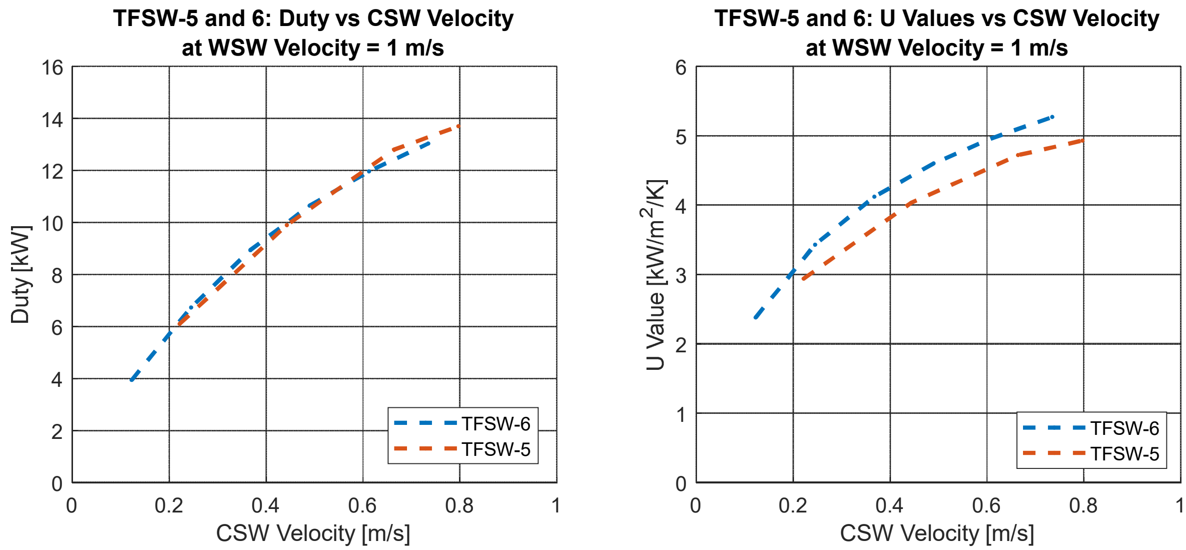

Figure 93. TFSW-5 and TFSW-6 Duty and U-value comparison.

5.4. SUMMARY

Seawater-seawater testing revealed for similar internal and external fluids, both internal and external fluid flow rates significantly affected duty and overall heat transfer performance. Four single-plate tests were used to identify the best internal channel spacing for use in the 12-plate test.

In all tests, the internal channel size was observed to deform depending on the pressure difference between the internal (cold seawater) side and external (warm seawater) side. The variability in the size of the internal channel contributed a significant degree of uncertainty in the test results. The degree of deformation was most clearly observed in the pressure drop vs cold seawater velocity results; at the same velocity, the largest channel had comparable pressure drop to the smallest channel.

For all tests, the internal convective coefficients varied linearly with velocity and the external convective coefficients increased logarithmically with velocity above 1.5 m/s. The trend of higher convective coefficients in larger channels was not observed, but this was most likely caused by uncertainty in the actual channel size tested.

The observed deformation is attributed to using large weld spacings and low forming parameters to achieve the desired effective internal channel spacings. Alternative designs which utilize smaller weld spacings and higher forming parameters can also be used to achieve comparable effective internal channel spacings. Makai intends to conduct more seawater-seawater counter flow testing with better designed plates to eliminate uncertainties caused by plate deformation.

6. COMMERCIAL APPLICATION FOR TFHX – CYANOTECH CASE STUDY

Cyanotech, Inc. is located adjacent to NELHA's research campus and grows algae in shallow, open freshwater ponds for commercial use. The pond water is constantly circulated using paddlewheels to provide mixing and aeration for the algae. The algae require temperature modulation; without cooling, temperatures rise above what the algae can tolerate and the algae begin to die off. Currently, Cyanotech runs cold seawater through 1" steel pipes resting on the bottom of the ponds to provide cooling. These pipes require constant maintenance (corrosion) and do not provide efficient cooling which means higher than necessary cold seawater usage (and higher operating costs).

The cooling system is required to remove heat from the pond water to maintain pond temperature below the algae threshold temperature. An efficient cooling system extracts as much cooling potential from the cold seawater as possible; i.e., the approach temperature (the difference between the cold seawater exit temperature and pond water temperature) is minimized. Although using a low cold seawater flow rate minimizes the approach temperature, the water flow rate must also be high enough to remove sufficient heat to maintain pond temperature.

Makai tested a TFHX cooling system a Cyanotech test pond. The test pond has a capacity of 67,000 liters. Cyanotech provided cooling data for a pond of the same size as the test pond; 86 gpm was required to maintain the pond temperature and the corresponding approach temperature was 9.8°C. Makai's goal is to provide the same duty at a lower cold seawater flow rate.

6.1. TFHX COOLING SYSTEM

The TFHX cooling system consists of three TFHX modules; a control valve; sensors to monitor pond temperatures; sensors to monitor cold seawater temperatures, pressures, and flow rates; a data acquisition module; and a laptop with custom control program to record sensor measurements, environmental data, and control cold seawater flow rate.

Makai installed three TFHX modules in the Cyanotech test pond in June – July 2019. Each TFHX module has 24 plates in which cold seawater flows on the inside of the plates (cold seawater effective spacing is 0.62 mm) and the pond water flows between the plates (pond water effective spacing is 24.4 mm). The modules utilize a pass-through design in which the modules are immersed in the pond and take advantage of the already circulating pond water; additional pumping is not required. The plates are separated by custom plastic spacers which also serve as a duct to deliver cold seawater to each plate. Aluminum end plates are used to interface the TFHX assembly and cold seawater piping. Threaded rods are used to compress gaskets and seal the plates and provide structural support for handling/installation.

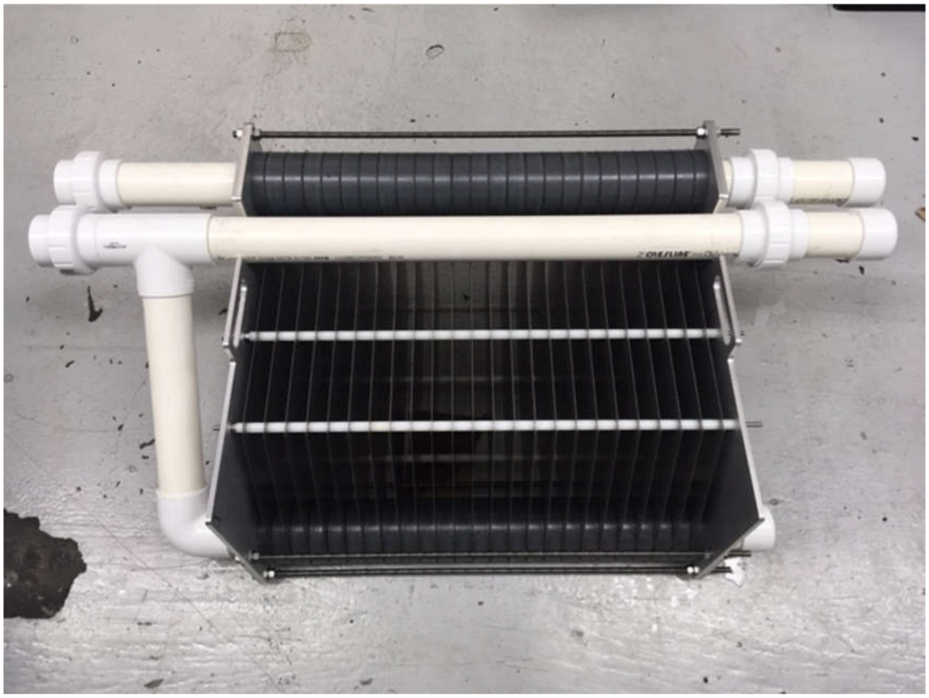

Figure 94. Single 24-plate TFHX module.

The TFHX modules were submerged directly in the pond, just after the paddlewheels. Initial designs considered pumping the pond water through an enclosed TFHX unit, but the submersible design is simpler, requires less equipment, is potentially easier to clean, and takes advantage of the flow already provided by the paddlewheels.

Figure 95. Single TFHX module installed in test pond.

Figure 96. Control valve and flow meter.

Temperature and pressure sensors are mounted on the cold seawater inlet and outlet piping. A flow meter is installed at the control valve to measure the cold seawater flow. For the pond water, temperature sensors are mounted before the paddlewheel and at the exit of each TFHX module.

The main contribution to increasing pond temperatures is solar insolation. Pond temperature can be decreased by evaporative cooling and the cooling system. For the test pond, the threshold temperature was set at 28°C. Cold seawater flow was controlled such that once the pond temperature rises above 27.8°C, cold seawater flow is started and continues to increase if the pond temperature continues to rise, reaching maximum flow if the pond temperature reaches 28.2°C. When pond temperatures start to decrease, cold seawater flow is also decreased.

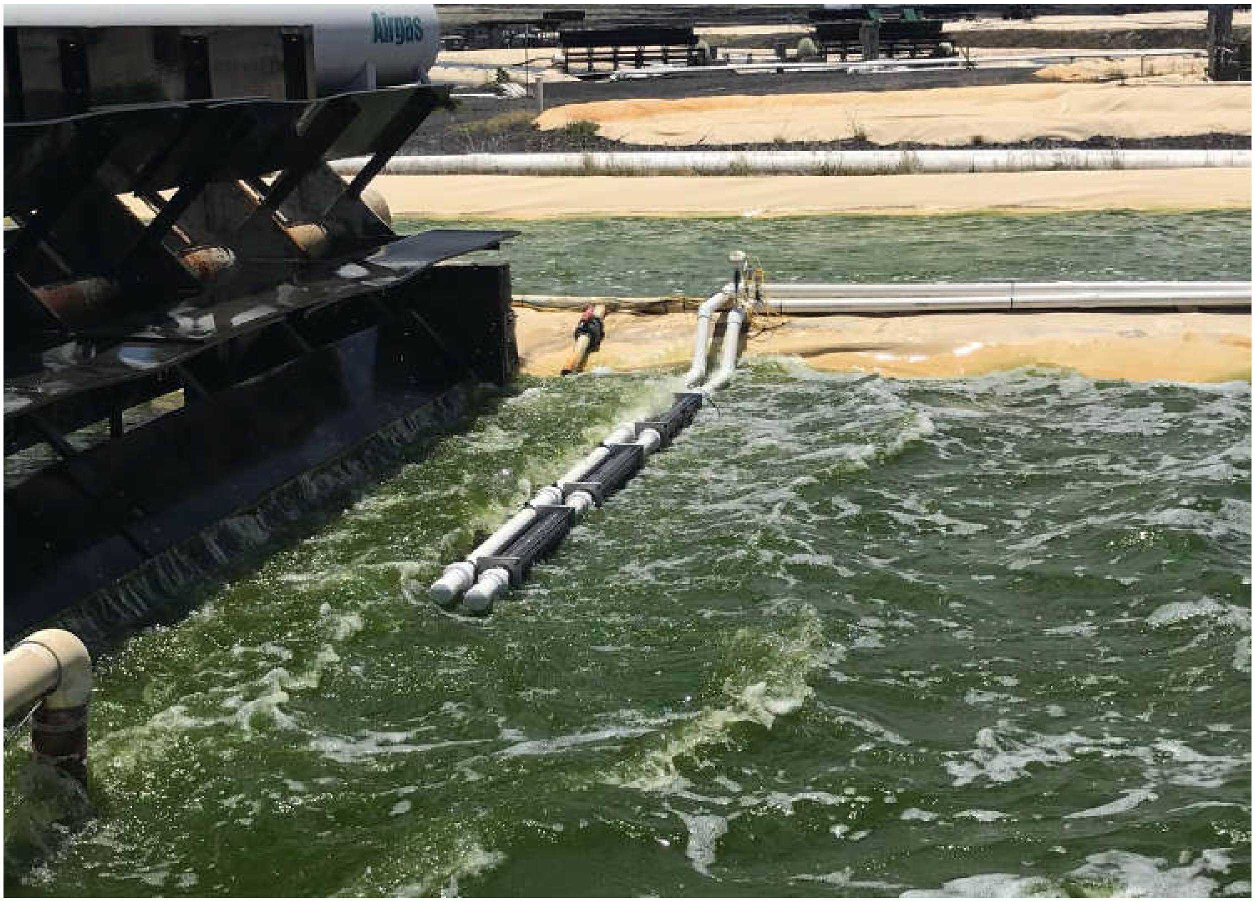

Figure 97. Three TFHX modules installed in the test pond.

6.2. TFHX PERFORMANCE

Initially, only one TFHX module was installed to conduct performance testing at different cold seawater flow rates in parallel flow and counter flow configurations. The counter flow configuration had U values ~ 10% higher and approach temperatures almost 1°C lower at the maximum flow rate.

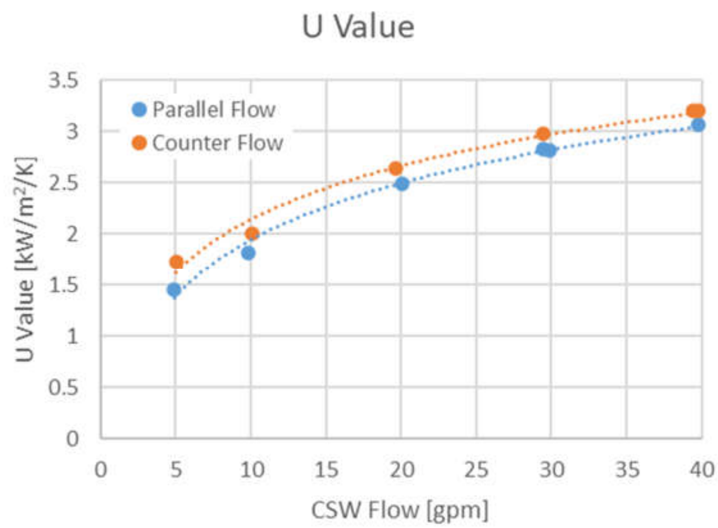

Figure 98. U value comparison between counter-flow and parallel-flow configurations

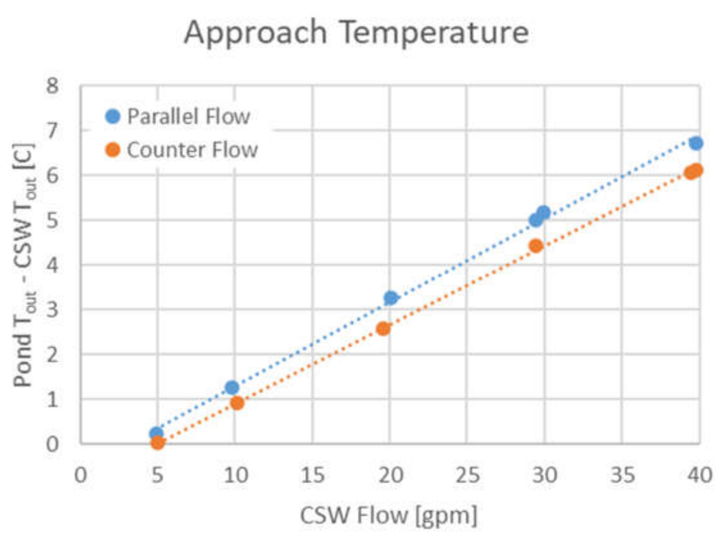

Figure 99. Approach temperature comparison between counter-flow and parallel-flow configurations

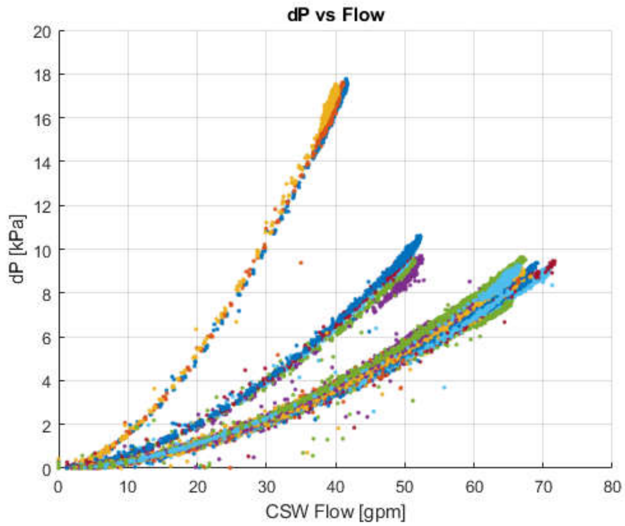

Figure 100. Cold seawater pressure drop vs flow for 1, 2, and 3 TFHX modules.

Based on the existing cold seawater distribution system, a maximum of 70 gpm of cold seawater was available at the test pond. Cold seawater is distributed to Cyanotech from the NELHA seawater distribution system and Cyanotech has its own distribution network within their facility, which includes booster pumps that are required to increase the cold seawater pressure to make up for pressure losses due to elevation gain, piping losses and heat exchanger losses. Having a lower heat exchanger pressure drop reduces the requires pumping power and can result in substantial operating expenses; pressure drop data was not available for the existing Cyanotech cooling system for comparison.

With all three TFHX modules installed, the TFHX cooling system was able to maintain pond temperature at or below 28°C. Typically, the cooling system was on between 9:30 AM and 5 PM.

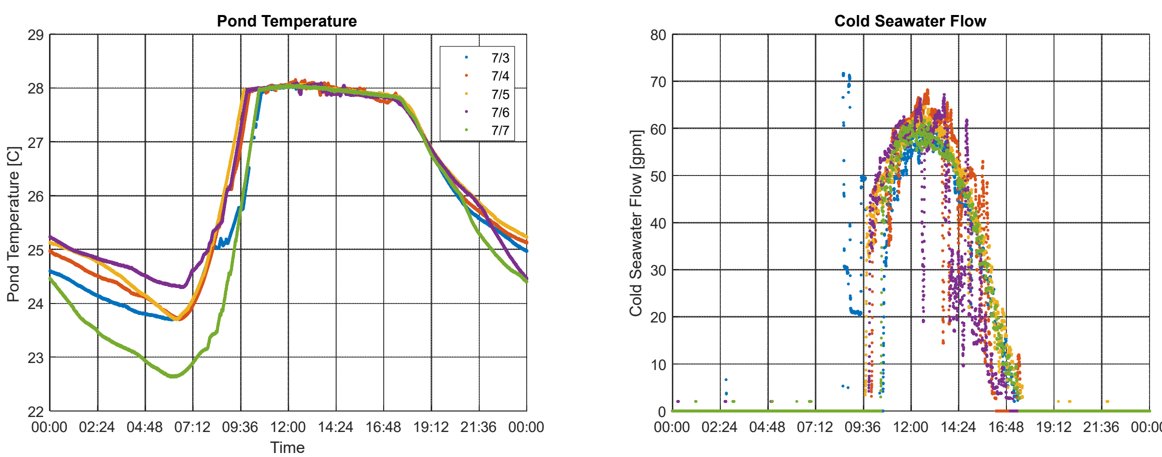

Figure 101. Pond temperature with TFHX cooling system.

The peak duty was 305 kW. At peak duty, the approach temperature was 3.65°C.

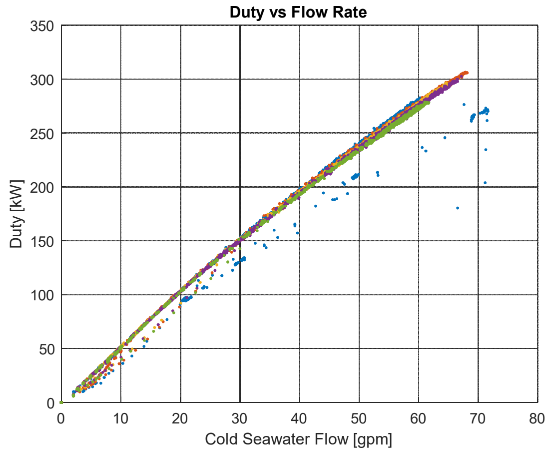

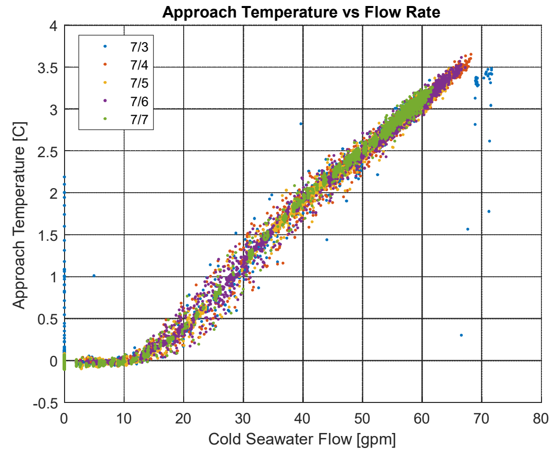

Prior to installing the TFHX cooling system, Makai also collected data on the existing cooling system in the test pond. The existing cooling system did not have a throttle valve; when the cooling system was on, the cold seawater flow rate was 70 gpm. The approach temperature was around 10°C. The TFHX approach temperature at 70 gpm can be extrapolated from the data to 3.75°C. This means, for the same flow rate, the TFHX is performing almost 3X the duty as the existing cooling system.

The TFHX, along with the control program and instrumentation, remained installed at Cyanotech until December 2019 (~ 5 months). Makai removed the control program and instrumentation but Cyanotech has kept the TFHX in operation to date.

6.3. SUMMARY

Makai successfully completed a case study for the first TFHX commercial application. The TFHX cooling system consisted of three TFHX modules, instrumentation, and a controls system. The TFHX modules utilized a pass-through design which took advantage of the circulation already required for algae growth and removed the complexity of adding pumps.

TFHX performance was substantially better than Cyanotech's existing cooling solution. The TFHX increase in efficiency over the existing cooling system translates to the ability to maintain the pond temperature below the threshold without pre-cooling the pond (as was required for the existing Cyanotech system) and provide the same cooling load at a lower cold seawater flow rate (enabled by the better approach temperature, 3.75°C vs 10°C.

In addition to a performance advantage, TFHX provides labor/maintenance savings for Cyanotech. The TFHX's modular design is also easy to handle and install. The wide plate spacing also enables pressure washing the plates in place for periodic cleaning and maintenance. Furthermore, the TFHX is constructed of corrosion resistant titanium foil, which will last the lifetime of the grow pond whereas the current cooling system requires replacement every three years.

7. CORROSION TESTING

Makai has completed the 10-year corrosion testing of aluminum alloys. The final corrosion sample was removed in January 2020. This section summarizes Makai's corrosion related findings.

7.1. BOX COUPONS

Box coupons have been tested since 2009. The previous removal and analysis of box coupons was performed in 2014, after 5 years of exposure in WSW, CSW, and DSW. Rack consolidation took place in 2015; a total of 5 columns of WSW samples, 2 columns of CSW samples, 1 column of WSW pre-treated samples, and 3 columns of DSW samples remain in testing. The final box coupon samples were removed in January 2020.

Alloys have generally performed well in WSW. Large pits were identified on some samples removed after 2 years of exposure and the last samples removed after 10 years of exposure (Figure 102), but not on samples removed in between. The pits were attributed to manufacturing defects or bias in testing conditions and are not believed to be indicative of alloy performance in WSW.

Alloys have performed unpredictably in CSW. Alloys 1100 and 3003 have the least scatter. Although some Alloy 3003 samples had pits > 0.5 mm, most have performed well. The Alloy 3003 ten-year samples had small, discrete accumulations of corrosion product but no severe pitting (Figure 103). Alloys 1100, LA83I, and LA83P had a few very poorly performing outlier samples, but in general, the weight loss results and pitting statistics followed a trend of increasing pits and pit depths with exposure time. Alloys 5052 and 6063 were all removed before 10 years. Both alloys had samples with highly variable performance; it is possible these alloys were subject to more manufacturing variability that affected performance.

Alloys performed poorly in DSW. In addition to pitting, crevice corrosion was also severe for the DSW samples.

Two samples of each alloy that underwent the WSW pre-treatment were tested for 10 years. Based on visual inspection, the WSW pre-treatment samples performed better than the CSW samples (e.g., Figure 104). There were small pits present on some of the samples, but no large catastrophic pits.

6063-98

5052-139

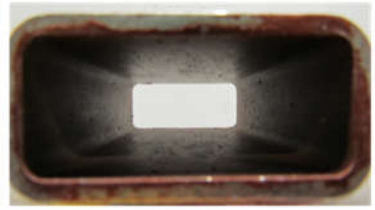

3003-3.19

6063-99

5052-141

3003-3.22

LA83P-43

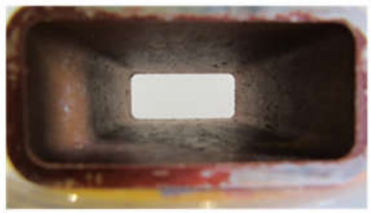

LA83I-80

LA83P-136

LA83I-142

Figure 102. Warm seawater samples after 10 years. Some samples were free of pits while other samples of the same alloy developed pits. Samples were subject to the same conditions and test disruptions.

Figure 103. Representative sample of Alloy 3003 in cold seawater after 10 years of exposure. Some small pits are present but no large catastrophic pits.

Figure 104. Alloy 1100 after 5 years in CSW on the left and after 10 years in CSW after receiving WSW-pretreatment on the right.

7.2. REPRESENATIVE HEAT EXCHANGER SAMPLES

Six FSW tubular mini-HX samples were reallocated to Makai from a previous testing contract. Testing began on the samples in 2014. Of the two CSW samples, one received the WSW pre-treatment (CSW-1) while the other was directly exposed to CSW (CSW-2). CSW-1 has corrosion and the FSW pull out points on both upstream and downstream tubesheets. Corrosion product was observed after ~2 years of exposure. There is also crevice corrosion at the gasket interface on the downstream tubesheet of CSW-1. Heat exchanger designs must carefully consider interior low-flow areas when using materials susceptible to corrosion. CSW-2 does not have visible corrosion product but is covered with black biofouling spots. The tube interior walls on both CSW samples are also rough; it is difficult to tell whether the attachments are biofouling or corrosion product. Flow was stopped to these samples in April 2019.

The four WSW mini-HX samples show no signs of corrosion product; however, biofouling is present on all samples. Biofouling has been worse on the upstream tubesheets compared with the downstream tubesheets. WSW-3 and -4 had a pattern on the interior tubewalls that was intended to enhance heat transfer; the pattern is no longer distinguishable; the tube walls appear to be covered with a fuzzy biofouling layer. Flow was stopped to these samples in December 2017.

One mini-CHART sample has been exposed in WSW since December 2013. After 4 years of exposure, no noticeable change has been observed. No corrosion product is visible, small flecks on the upstream face may be biofouling. The window on the upstream face has been obscured by biofouling film. Flow was stopped to this sample in September 2018.

Figure 105. Representative CHART sample after 5 years in WSW. Biofouling present on the face but the channels are smooth and corrosion free.

7.3. FFHX COUPONS

FFHX corrosion sample testing began in June 2015. The first three samples were removed after 2 months due to corrosion at weld defects and at the gasket interface. Three additional samples were tested starting in September 2015 and removed in February 2017. At the time of removal, all FFHX samples were severely corroded. Corrosion that initiated at a weld defect progressed on the back side of the sample, corroding the aluminum fins to the extent that the fins detached from the titanium foil. Along some weld lines, enough corrosion product built up to push and eventually tear the fins from the foil along the weld line.

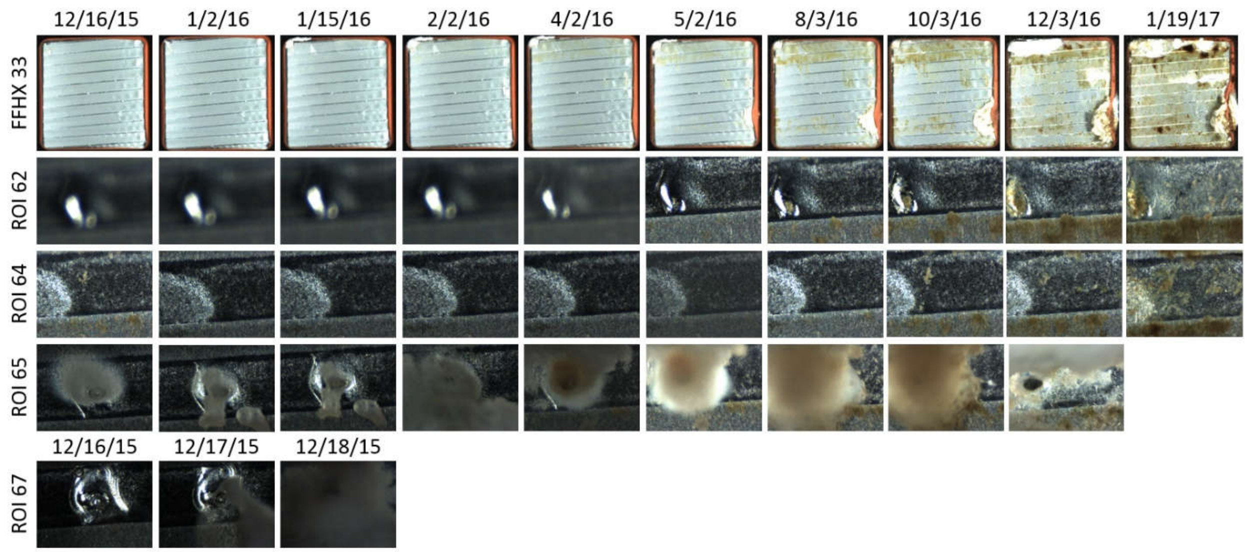

Figure 106. Sample was removed after 13 months. Three out of eleven weld lines had significant corrosion product and gasket corrosion was severe. Seawater was leaking out the back side due to gasket distortion from corrosion product.

FFHX corrosion testing emphasized the importance of reliable welds – defects most likely exposed the aluminum fins to seawater and began to corrode preferentially. For an OTEC heat exchanger, any breach from seawater to working fluid is considered a failure of the heat exchanger and must be avoided.

7.4. TFHX COUPONS

Five TFHX samples were installed in the CSW MCIR in July 2017. The TFHX samples utilize the same delrin frame as the ultrasonic testing samples; three samples fit in one MCIR column. Each sample has 2-mm radius circles that are spaced 8 mm apart, either using a triangular or rectangular grid. One column of samples will receive hypochlorination treatment (daily, 100 ppb dosage) and the other column will be the control. In each column, at least one sample will have the back side of the weld (vice the weld side) exposed to CSW. Each sample also has a small pinhole punched into the non-exposed side. If any holes develop on the exposed foil, it should leak into the expanded region and drip out the pin hole.

Because the TFHX is only fabricated from titanium, corrosion is not expected. However, biofouling testing can provide treatment options for OTEC heat exchangers. In addition, the long-term performance of the samples in flowing seawater – in terms of maintaining the bubble height and fatigue performance of the welds and foil – also provides important data. Upon flow initiation, the samples were observed bow outward due to exposure to pressurized seawater. The sample was also observed to vibrate (like a speaker diaphragm), with dominate frequencies of 15 Hz and 58 Hz; this can provide an unintentional, but useful, fatigue test. In an actual heat exchanger, the TFHX plates will be supported by the pressurized ammonia between the welded foil; however, ammonia pressure may fluctuate depending on the seawater temperatures, seawater flow rates, and ammonia duty.

Automated imaging will not be performed due to low image quality due to the highly reflective, uneven, and occasionally vibrating surface. Images will be taken periodically with a camera.

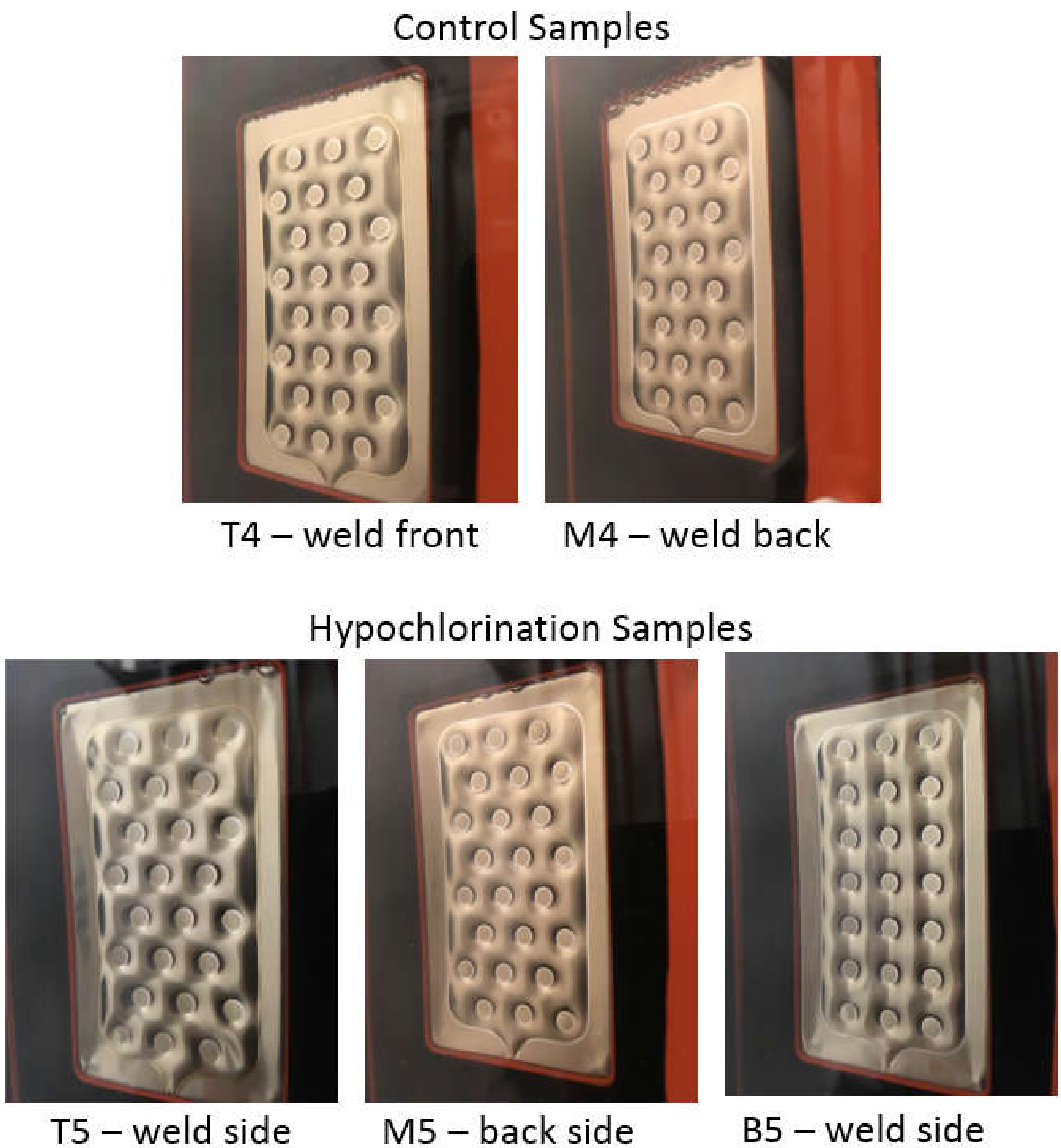

Figure 107. TFHX samples.

Flow was stopped to these samples in January 2020. No corrosion or biofouling was observed.

7.5. PIT MITIGATION TREATMENTS

Makai investigated acid treatments, ozone treatments, hypochlorite treatments, and WSW pre-treatments in the MCIR. Acid treatments performed based on OCP-based intervals delayed the onset of pitting by over a year compared to the control sample. Pits appeared on the acid-treated sample only after a dry-out vice acid treatment was performed. Acid treatments performed on a 2-month interval were ineffective. Acid treatments have been observed to remove corrosion product buildup and biofouling. WSW pre-treatment delayed the onset of pitting by ~ 2 years. Ozone treatment was tested but increased pitting in CSW samples. Hypochlorite treatments (provided to ultrasonic samples) in CSW have maintained shiny, like-new sample surfaces.

Acid treatments were tested in WSW but results have been inconclusive as neither the control nor any of the treated samples had pits.

7.6. BIOFOULING

Makai tested ozone, iodine, and chlorine dioxide treatments in addition to daily hypochlorite treatments for biofoulant control. Hypochlorite treatments are the most effective. As long as hypochlorite treatment is consistent, it is effective at preventing biofilm/biofouling; however, once biofilm begins to form (e.g., due to failure in the bleach delivery system), hypochlorination is does not remove the film and additional material can accumulate on the film. Although manual cleaning is effective at removing biofilm, it is time consuming and impractical for heat exchangers. Acid treatments and flow reversals remove most of the biofilm and can be implemented for a heat exchanger.

7.7. SUMMARY

Makai has performed over 10 years of aluminum alloy corrosion testing. Makai tested box and flat samples of various alloys, flat samples with different manufacturing methods, and representative heat exchanger samples. Electrochemical measurements, weight measurements, and visual observations were collected for the first 5 years of testing. Based on early observations of poor performance in cold and deep seawater, Makai also investigated pit mitigation treatments. The warm-seawater pre-treatment and acid treatments, when performed as needed, were successful in delaying the onset of pit development. However, by the fifth year of corrosion testing, Makai determined aluminum performance in cold seawater was unreliable and too risky to use in a large-scale OTEC environment. Samples of the same alloy had drastically different results; some 2-year samples had severe pitting but samples removed after 4.5 years only had minor pits. The acid treatments were time-consuming and had to be performed as dictated by electrochemical measurements; missed or delayed treatments led to loss of protection. The warm seawater pre-treatment was successful for box coupons (except some Alloy 6063 samples). Tests of the representative heat exchangers revealed severe crevice corrosion at sealing interfaces. Crevices could be eliminated to some extent in the design process, but could still pose a risk if any manufacturing anomalies or obstructions introduced unintentional crevices.

8. CONCLUSION

Between August 2018 and December 2019, Makai accomplished:

- Two design iterations of TFHX plates from 3B to 3C to 3E and initial testing of 3F
- Construction of over 300 plates for characterization studies
- Design of High Speed Welding Station (HSWS) to produce step reduction in TFHX labor and overheard fabrication costs
- Design, construction, and commissioning of new air convection testing, fatigue, and hydraulic testing apparatuses
- Performance testing of 4 cross-flow seawater-ammonia heat exchangers
- Performance testing of 5 counter-flow seawater-seawater heat exchangers
- Performance testing of 13 cross-flow air-water heat exchangers
- TFHX commercial case study at Cyanotech
- Completion of 10-year corrosion testing program

The TFHX has undergone two complete design revisions, from TFHX-3B to 3C to 3E. Each revision significantly reduced the materials cost for a TFHX plate, shortened fabrication time, and improved the performance and volumetric density by decreasing the plate-to-plate spacing. As a result, the time required to fabricate TFHX plates (and the associated cost of labor) became the limiting factor to commercialization of TFHX in different applications. Makai developed the HSWS to increase production rate by at least 5X and simultaneously reduce labor costs.

TFHX characterization remains an on-going task. Although over 300 plates were fabricated for characterization, plate construction for performance testing was given priority over plates constructed for characterization. With commissioning of the HSWS, Makai will have an additional platform for fabrication and can use the existing stage to continue to produce customized plates for characterization tests. From the existing characterization work, Makai is able to develop weld patterns to produce TFHX plates with a designated internal channel size. For the same weld patterns, the pressure rating was found to vary depending on the overall plate shape and weld design. Fatigue testing has produced inconsistent results, with most failures occurring at the seal or transition welds. Makai has redesigned portions of the seal and transition welds and will be re-testing multiple plates. These tests are intended to provide a baseline estimate on the expected TFHX lifetime under various loading conditions. For customized TFHX applications, particularly for asymmetrical, non-uniform overall plate shapes and/or manifold shapes, pressure and fatigue testing the final plate design plate is recommended.

In seawater-ammonia heat exchanger performance, TFHX had high ammonia-side convective coefficients while maintaining comparable seawater-side convective coefficients. With the 1-mm plate spacing enabled by interlocking TFHX-3E plates, the TFHX packs nearly 7X more heat transfer area in the same volume as conventional shell-and-tube and plate-frame heat exchangers. An analysis on replacing the heat exchangers previously selected for a 2.5 MW offshore OTEC plant with TFHXs showed for the same heat exchanger area, the same net power could be produced in 10% of the volume and 50% of the heat exchanger cost. Increasing TFHX area to match the cost of the previously selected heat exchangers can increase net power production by 28% (3.6 MW vs 2.8 MW) and requires only 20% of the volume. With strong performance testing results, improvements in fabrication time, and continued reduction in materials costs, the TFHX provides a viable solution for OTEC heat exchangers.

In air-water testing, the TFHX had strong air-side performance at higher air velocities. In applications with sufficient allowances in air pressure drop, the TFHX can take advantage of tight air-side channel spacings to enhance convection and increase performance.

Seawater-seawater testing results were used to design the first commercial TFHX application for Cyanotech®. The TFHXs were able to maintain the test pond temperature below the threshold temperature without precooling (i.e., intentionally dropping pond temperature to mitigate a midday temperature increase). For the same water flow rate, the TFHX had a smaller approach temperature than Cyanotech's existing heat exchangers and was able to provide the required cooling using less cold seawater. The TFHX was successfully tested and has remained installed and operational for 9 months.

Finally, Makai has concluded a 10-year aluminum alloy corrosion testing program. Aluminum alloys have performed poorly in cold seawater. In warm seawater, aluminum alloys performed well in general, but several samples had significant pitting. With unpredictable performance and an economically competitive titanium alternative in the TFHX, Makai sees no advantage in pursuing aluminum heat exchanges in seawater applications.

9. APPENDIX A – SEAWATER-AMMONIA HEAT EXCHANGER TESTING

9.1. DATA ACQUISITION AND INSTRUMENTATION

Data was sampled every 0.1 seconds and the average of the last ten samples was recorded every second. Only steady-state data was used for analysis. Each point was held as long as necessary to obtain a solid steady-state data set. Steady-state was determined manually during data review by evaluating:

Measurement	Criteria
Ammonia vapor flow rate	+/- 0.002 kg/s
Quality	+/- 2%
Seawater flow rate	+/- 2 gpm
LMTD	+/- 2% and not trending
Evaporator pressure vs seawater inlet temperature	Slope matches saturation curve and pressure fluctuations within +/- 2 kPa
Degree of subcooling	No trend

Sensors used to characterize heat exchanger performance are listed in Table 2. Calibrations were performed during commissioning. Sensor performance was checked periodically during testing by comparing measurements at times when all sensors should be reading the same value. For example, with seawater flowing but no ammonia flow, the seawater inlet and outlet temperatures were verified to be the same, within error. Ammonia pressure sensors were checked in a similar manner; overnight periods of no ammonia flow and some cold seawater flow condensed all the liquid ammonia into the buffer tank, leaving ammonia vapor (at saturation conditions) in the rest of the system. All pressure sensors were verified to read within 1 kPa.

9.2. CALCULATED VALUES

Several values are calculated by the 100 kW control software in real time. These values are used in determining steady state operation and characterizing heat exchanger performance.

9.2.1. LMTD

LMTD is a measure of the average temperature difference across the heat exchanger. It is used in the calculation of overall heat transfer coefficient, U. LMTD is calculated according to:

$$LMTD = \frac{(T_{water\ in} - T_{ammonia\ in}) - (T_{water\ out} - T_{ammonia\ out})}{\ln \frac{T_{water\ in} - T_{ammonia\ in}}{T_{water\ out} - T_{ammonia\ out}}}$$

The ammonia temperatures used to calculate LMTD are the saturation temperatures of ammonia at the inlet and outlet pressures, not the temperatures measured by the ammonia temperature sensors. LMTD assumes a linear change in temperature from inlet conditions to outlet conditions, which is not the case when ammonia is changing state (boiling) in the heat exchanger. Typically, evaporators increase the temperature of incoming liquid to the saturation point very quickly. As such, the majority of the heat exchanger is operating between the saturation temperatures of the incoming liquid and the outgoing saturated liquid/vapor mixture. As seen in Table 24, the change in enthalpy when heating ammonia liquid from 18°C to 20°C (blue highlight to green highlight) is 9.5 KJ/kg, while it takes 1186.4 KJ/kg to vaporize ammonia at 20°C (green highlight to yellow highlight). Using the saturation temperatures (based on the inlet and outlet pressures) in the LMTD equation is more accurate than using the temperature sensors. Saturation temperatures are calculated in real-time using a set of equations of state within the program *Refprop* published by National Institute of Standards and Technology (NIST).

Table 23. Sensors Used in Heat Exchanger Performance Testing

Name	Measurement/Description	Accuracy	Range
CIFS	Ammonia Vapor Flow Rate	0.25% of rate	0-3.47 kg/s
EIFS	Ammonia Liquid Flow Rate	0.1% of rate	0-3.47 kg/s
COPS/EIPS	Condenser Outlet / Evaporator Inlet Pressure	0.04% FS*	400-1100 kPa gauge
COTS/EITS	Condenser Outlet / Evaporator Inlet Temperature	0.1 C + 0.1% FS	0-30 C
CIPS/EOPS	Condenser Inlet / Evaporator Outlet Pressure	0.04% FS	400-1100 kPa gauge
CITS/EOTS	Condenser Inlet / Evaporator Outlet Temperature	0.1 C + 0.1% FS	0-30 C
dT A/B	Seawater Inlet/Outlet Temperature	0.005% of measurement	0-30 C
HXWPS1	Seawater Pressure before Plates	0.25% FS*	0-15 psia
HXWPS2	Seawater Pressure after Plates	0.25% FS*	0-15 psia
HXFS	TFHX Seawater Flow	0.25% of rate	0-30 ft/s

* Another +/- 0.5% FS due to temperature error band needs to be added to the stated static accuracy. In practice, the pressure sensors are accurate to +/- 1 kPa.

Table 24. Ammonia Saturation Properties

Saturated Properties					
Temperature	Pressure	Liquid Enthalpy	Vapor Enthalpy	Liquid Entropy	Vapor Entropy
[C]	[kPa]	[kJ/kg]	[kJ/kg]	[kJ/kg/C]	[kJ/kg/C]
14	704.63	216.60	1426.80	0.82	5.03
16	753.03	226.05	1428.41	0.85	5.01
18	803.95	235.52	1429.94	0.89	4.99
20	857.48	245.02	1431.39	0.92	4.96

Ammonia exits the evaporator in a saturated liquid-vapor mixture. The specific enthalpy at the evaporator exit also depends on quality. At 20°C, 40% quality ammonia vapor exits with a specific enthalpy of 719.57 kJ/kg. Pre-heating (raising ammonia liquid temperature to saturated temperature) 2°C adds an additional 1.3% to the required duty. For comparison, in a condenser, 2°C of superheating only adds 0.1% to the required duty.

9.2.2. Duty

Duty is a measure of the heat transferred between seawater and ammonia and is used in the calculation of overall heat transfer coefficient. Duty can be calculated based on the seawater or based on the ammonia. The equations used to calculate the duty are:

$$Duty_{water} = \dot{m} * C * (T_{in} - T_{out})$$

$$Duty_{ammonia} = \dot{m} * (h_{out} - h_{in})$$

$\dot{m}$ = mass flow rate [kg/s],

C = specific heat capacity of seawater [kJ/kg],

T = seawater temperature [C], and

h = ammonia specific enthalpy [kJ/kg]

Ammonia enthalpies are calculated based on inlet and outlet pressures and temperatures using Refprop. Ammonia outlet enthalpy also uses quality, which is calculated from Coriolis flow meters measuring vapor flow after the separator tank and liquid flowing into the evaporator. Theoretically, the ammonia duty should be equal to the seawater duty as both are a measure of the heat transferred between the two fluids. However, in practice, external heat input and any error in the sensors can cause the calculated duties to be slightly different.

9.2.3. Overall Heat Transfer Coefficient

The overall heat transfer coefficient, U, is a measure of the overall efficiency of a heat exchanger. It is calculated according to:

$$U = \frac{Duty}{LMTD * Area}$$

LMTD = log mean temperature difference [C]

Area = heat transfer area of the heat exchanger [m^2]

Both duty and LMTD directly impact the calculation of overall heat transfer coefficient. The duty used to calculate the heat transfer coefficient is the ammonia duty.

9.2.4. Convective Heat Transfer Coefficients

The overall heat transfer coefficient is a function of the convective and conductive heat transfer coefficients:

$$\frac{1}{UA_{total}} = \frac{1}{h_{SW}A_{SW}} + \frac{t}{k_{foil}A_{foil}} + \frac{1}{h_{NH3}A_{NH3}} \qquad \textit{Equation 9-1}$$

where

A_{total} = the effective heat transfer area [m^2],

h_{sw} = seawater convective coefficient [kW/m^2C],

A_{sw} = seawater heat transfer area [m^2],

t = foil thickness [m],

k_{foil} = thermal conductivity of titanium foil [kW/mC],

A_{foil} = foil heat transfer area [m^2],

h_{NH3} = ammonia convective coefficient [kW/m^2C], and

A_{NH3} = ammonia heat transfer area [m^2].

The heat transfer area for each component in Equation 3-1 is the same; Equation 3-1 reduces to:

$$\frac{1}{U} = \frac{1}{h_{SW}} + \frac{t}{k_{foil}} + \frac{1}{h_{NH3}} \qquad \textit{Equation 9-2}$$

1/U is calculated from the data as described in Section 9.2.3. t/k_{foil} is a constant based on the physical and thermodynamic properties of the foil.

In order to determine h_{SW} and h_{NH3}, the seawater-side heat transfer coefficient was assumed to be constant for a fixed seawater flow rate and the ammonia-side heat transfer coefficient was assumed to be constant for a fixed ammonia flow rate. By holding seawater flow rate constant and changing the ammonia flow rate and vice versa, a matrix of U-values for each combination of seawater flow rates and ammonia flow rates can be generated. The entire set of equations was solved simultaneously using the method of constrained least squares.

9.3. DATA PROCESSING

Data were first graphed in the 100 kW control program. Large sections of data could be quickly reviewed and steady-state data was averaged and added to a summary file. Sections of steady-state data were added to a separate file.

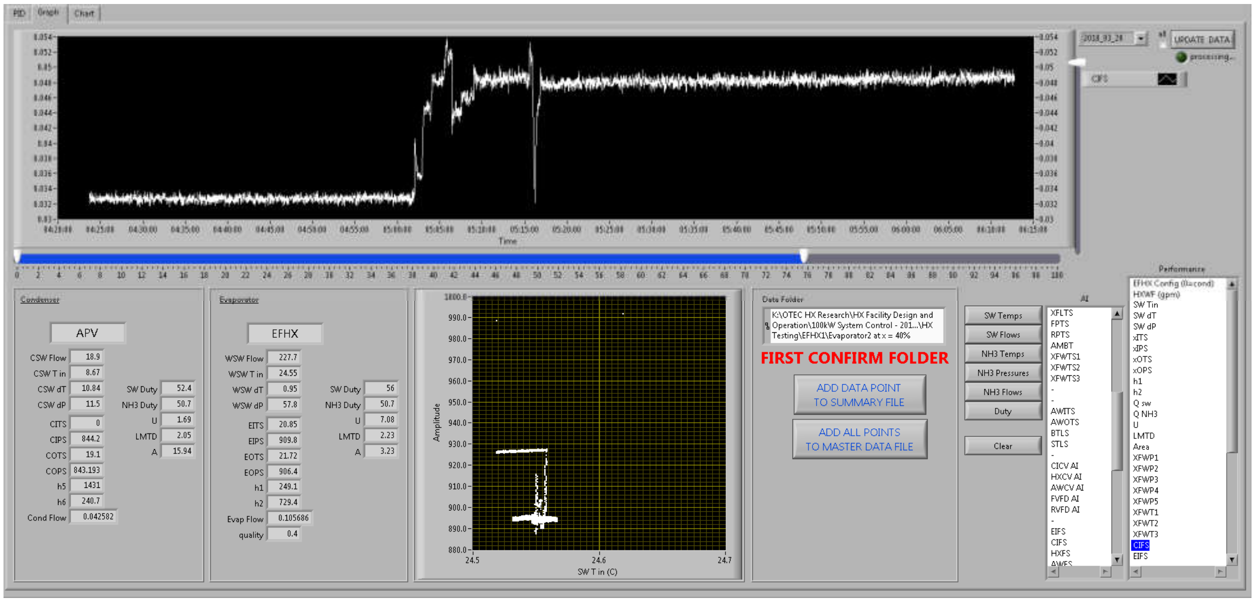

Figure 108. Data review program is first used to identify sections of steady-state data. For each section, an averaged set of values is saved in a summary file and all points in the section are saved in a master data file.

Data were then sorted into the targeted test points (Table 3). Only data sets with less than 2°C subcooling at the inlet were used to determine U-values for comparison and to calculate convective coefficients. Due to difficulties in seawater and ammonia flow control, evaporator pressure fluctuations up to 2 kPa were observed. In addition, linear regression of U-values versus ammonia vapor flow rate was used to normalize U-values to the target ammonia vapor flow rate. There was not enough ammonia in the system to test ammonia vapor flow rates of 0.096 kg/s at 40% quality.

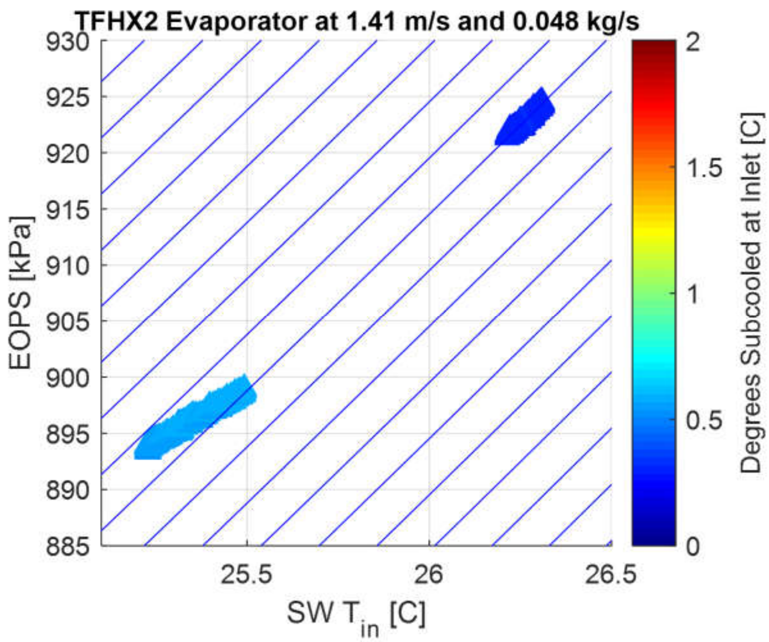

Figure 109. An example of data from a test point. Subcooling was not explicitly tested but some test points had sets with different degrees of subcooling.

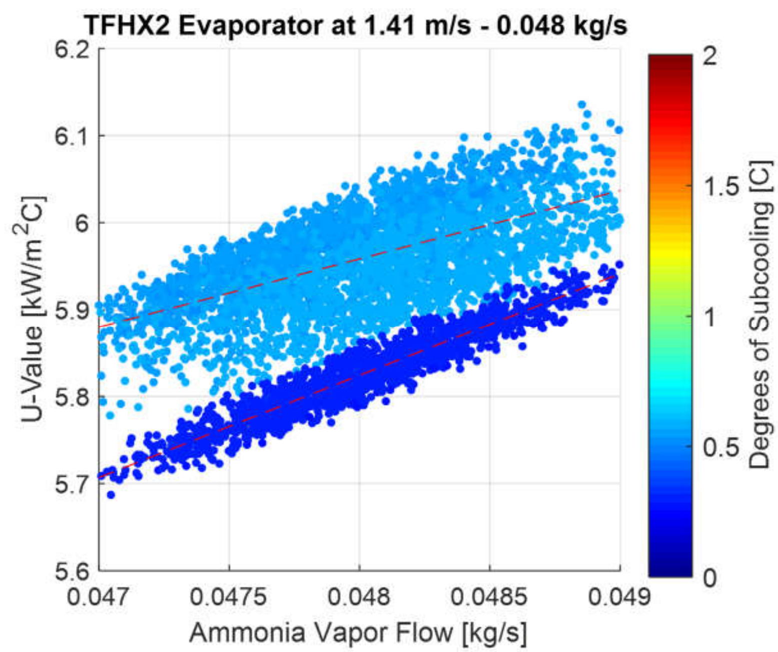

Figure 110. Only data taken with <2°C superheat were used to determine U-values. U-values are strongly dependent on ammonia vapor flow rate; U-values were first normalized to the target ammonia flow rate using linear regression before being used for comparison between test points and in calculations to determine convective coefficients.

10. Appendix B - Air Convection Testing

10.1. DATA ACQUISITION AND INSTRUMENTATION

A custom developed Labview-based program was used to collect data. The instruments (Table 25) output a 4-20 mA signal, proportional to the measurement, which was read using National Instruments' NI 9208 Analog Input modules. Measurements were sampled 10X a second, averaged, and recorded every second. RefProp 10 was used obtain density and specific heat capacity for dry air and water at the testing temperatures and pressures, and used in calculating velocity/mass flow rate and duty.

Table 25. Instrumentation used in air convection testing

Instrument	Model	Range	Accuracy
Air Velocity	Kanomax 6812 w/ AP100	0.3 – 35 m/s	±1% of reading ± 1 digit
Air Velocity	Kanomax 6036	0.01-30 m/s	±3% of reading
Air Velocity	Dwyer	0-30 m/s	±3% of reading in 4-32°C range
Air Mass Flow Rate	Coriolis CMFS150M		±0.25% of reading
Air Inlet/Outlet Temperature	Intempco MIST 55	0-50°C	±0.15°C
Air Inlet/Outlet Pressure	GE Druck Unik 5000	0-5 psig	±0.04% FS
Water Flow	N/A	0.2-2 gpm	±2%
Water Inlet/Outlet Temperature	Intempco MIST 55	0-50°C	±0.15°C
Water Inlet/Outlet Pressure	GE Unik 5000	0-50 psia	±0.2% FS

10.2. CALCULATIONS

10.2.1. Air Velocity

When using the anemometer to measure air velocity (TFAC-3C tests), the in-channel air velocity is calculated by multiplying the measured air velocity by the ratio of the cross-sectional areas between the measurement section and the test section. Air velocity was measured 2 ft downstream from the exit of the test section in a 2" Schedule 40 PVC pipe which has a cross sectional area of 0.002164 m^2. The cross-sectional flow area in the test section is determined by the height and width of the test section (50 mm x 6 mm) and the area occupied by the plates (# of plates x water-side spacing + 2 x # of plates x foil thickness):

	Air cross-sectional flow area	Ratio
TFAC-3C-1: 4-plate test	0.000150 m^2	14.478
TFAC-3C-2: 5-plate test	0.000112 m^2	19.345
TFAC-3C-3: 6-plate test	0.000164 m^2	13.173
TFAC-3C-4: 5-plate test	0.000187 m^2	11.578
TFAC-3C-5: 4-plate test	0.000210 m^2	10.328

When the air mass flow rate was measured with the Coriolis (TFAC-3E tests), the in-channel air velocity was calculated by dividing the mass flow rate by the outlet air density and the air cross-sectional flow area.

	Air cross-sectional flow area
TFAC-3E-1: 8-plate test	0.000152 m^2
TFAC-3E-2 & TFAC-3E-9: 6-plate test	0.000189 m^2
TFAC-3E-3 & TFAC-3E-6: 4-plate test	0.000226 m^2
TFAC-3E-4 & TFAC-3E-7: 7-plate test	0.000170 m^2
TFAC-3E-5: 5-plate test	0.000207 m^2

10.2.2. Duty

Air and water duties are calculated using $Q = \dot{m}\, c_p\, (T_{in} - T_{out})$ where $\dot{m}$ = measured mass flow rate (Coriolis) or volumetric flow rate x density (anemometer):

	volumetric flow rate [m^3/s]	density [kg/m^3]	c_p [kJ/kg]
air	measured velocity in 2” pipe x 2” pipe cross section	Determined using Refprop at the averaged outlet temperatures and outlet pressure	Determined using Refprop at the averaged the inlet and outlet temperatures and outlet pressure
	measured mass flow rate		
water	$\frac{measured\ gpm}{15850.3\ \frac{gpm}{m^3/s}}$	Determined using Refprop at water inlet temperature and pressure.	Determined using Refprop at water inlet temperature and pressure.

10.2.3. LMTD

The log mean temperature difference is calculated from the measured inlet and outlet water temperatures, the measured inlet air temperature, and the averaged outlet air temperature.

$$LMTD = \frac{\left(T_{water,in} - T_{air,out}\right) - \left(T_{water,out} - T_{air,in}\right)}{\ln \frac{\left(T_{water,in} - T_{air,out}\right)}{\left(T_{water,out} - T_{air,in}\right)}}$$

Typically, a correction factor is applied to LMTD to account for the cross-flow configuration, but for the tested conditions, the correction factor is ~1.

10.2.4. Overall Heat Transfer Coefficient

The overall heat transfer coefficient, U-value, is calculated by Q = U A LMTD where the area for each configuration is listed in Table 20.

10.2.5. Determination of Air-Side Heat Transfer Coefficients

Air-side heat transfer coefficients were calculated using $\frac{1}{U} = \frac{1}{h_{water}} + \frac{t}{k} + \frac{1}{h_{air}}$ and assuming a constant water-side heat transfer coefficient of 20 kW/m^2/K, regardless of the water-side internal channel spacing and flow rate.

Previous analysis compared four methods of calculating the air-side heat transfer coefficient: using a constant water-side Nusselt number, functional Wilson plot, two-coefficient Wilson plot, and a weighted least-squares solution simultaneous equation solver. The resulting water-side heat transfer coefficient ranged from 1 - 15 kW/m^2/K (Figure 111). The functional Wilson plot produced conflicting water-side convective coefficients for the same water flow rate. The 2-coefficient Wilson plot produced a range of air and water convective coefficients depending on the chosen correlation. Additionally, the linear fit to the Wilson plot x and y coordinates was poor which lowers the confidence in the results.

Using correlations developed for pillow-plate heat exchangers, the water-side heat transfer coefficients are more likely in the range of 10-30 kW/m^2/K. There is < 10% increase in air-side convective coefficients for a decrease in water-side heat transfer coefficient from 30 kW/m^2/K to 5 kW/m^2/K. Therefore, Makai has chosen a constant water-side heat transfer coefficient of 20 kW/m^2/K to calculate air-side convective coefficients.

10.2.6. Description of Wilson Plot methods

In the functional form of the Wilson plot method, a function representing the air-side heat transfer coefficient, F_{air}, is assumed to follow the form of the Gnielinski correlation. No assumptions are made of the water-side heat transfer correlation except that the water-side heat transfer coefficient depends only on the water flow rate. Additionally, the heat transfer coefficients are assumed independent of each other. For the same water flow rate but varying air flow rates, 1/U is plotted versus $1/F_{air}$ and fitted with a line. The intercept of the line is the average water-side heat transfer coefficient. The slope of the line is a correction factor such that $h_{air} = \frac{1}{slope} \times F_{air}$.

In the two-coefficient Wilson plot method, the air-side heat transfer coefficient is again assumed to follow the form of the Gnielinski correlation but a correlation is also applied to the water side. Several correlations and a constant Nusselt number of 7.54 were individually substituted as the form for the water-side heat transfer coefficient. For each correlation, $\left(\frac{1}{U} - \frac{t}{k}\right) F_{air}$ is plotted versus ${F_{air}}/{F_{water}}$ and fitted with a line. The slope and intercept of the fitted line are correction factors applied to h_{air} and h_{water} calculated using the correlations such that $h_{air} = \frac{1}{intercept} \times F_{air}$ and $h_{water} = \frac{1}{slope} \times F_{water}$.

The calculation of the friction factor used in the Gnielinski correlation requires further explanation. For smooth tubes, the friction factor can be found using $f = (0.79 * \ln(Re)-1.64)^{-2}$ and for rough tubes, the Swamee-Jain approximation to the Colebrook equation provides $f = 0.25 \cdot \left[\log\left(\frac{\varepsilon/D}{3.7} + \frac{5.74}{Re^{0.9}}\right)\right]^{-2}$. However, when used to calculate the dP, the Swamee-Jain approximation overpredicted pressure drop by 2-4 times and the smooth tube approximation underpredicted pressure drop by 50%. Alternatively, the friction factor could be calculated from the measured dP, $f = \frac{dP}{\rho}\frac{d}{L}\frac{2}{v^2}$, with some assumptions: 1) fully developed flow, 2) negligible entrance/exit or expansion/contraction losses, 3) negligible pressure drop outside the test section. This calculated friction factor was used in the Gnielinski correlation.

In the two-coefficient Wilson plot method, data from plates with the same water-side channel spacings were analyzed collectively. Regardless of the air channel spacing or air flow rates, for the same water channel, the water-side heat transfer coefficient should be the same at the same water flow rate (velocity).

Figure 111 shows the variation in the calculated water-side heat transfer coefficient depending on the method used and the applied correlation. For Pattern B configurations (TFAC-3C-3-5), for the same water flow rate of 0.1 gpm per plate, the water-side heat transfer coefficient calculated using the two-coefficient Wilson plot method varied from 1,000 W/m^2/K to 16,000 W/m^2/K depending on the correlation used (Figure 111). The functional Wilson plot resulted in a water-side heat transfer coefficient ~1,000 W/m^2/K at 0.1 gpm whereas the constant Nu = 7.54 assumption resulted in a water-side heat transfer coefficient of 10,300 W/m^2/K.

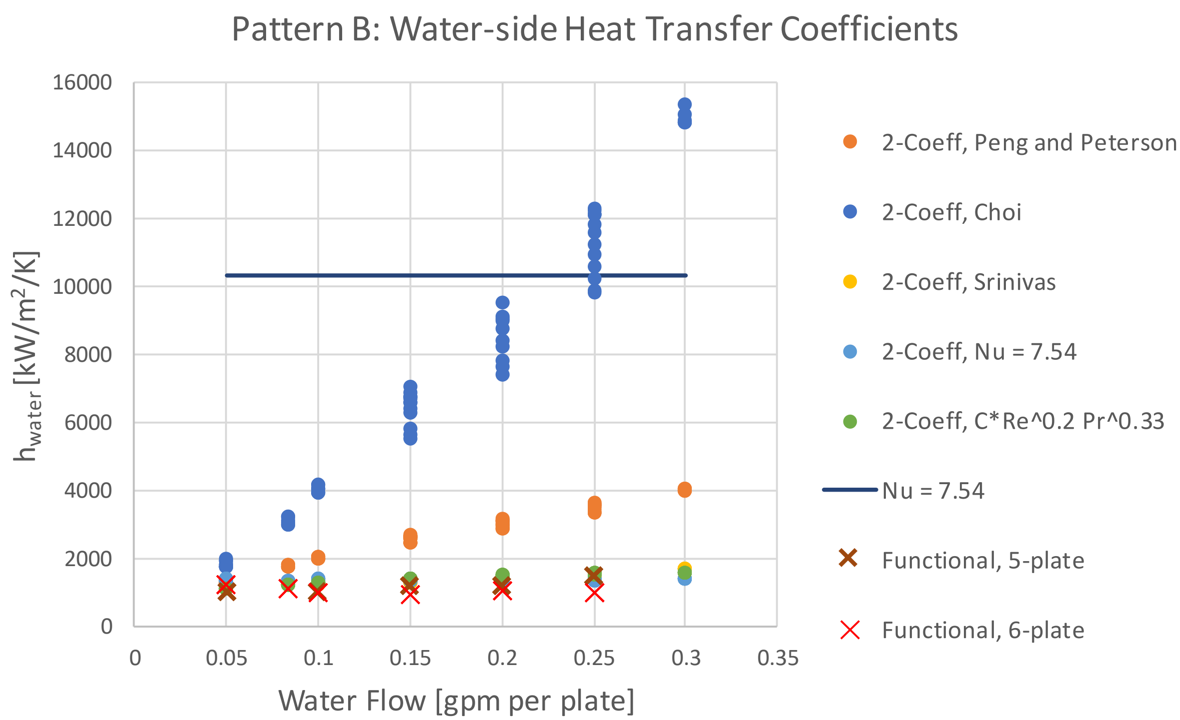

Figure 111. Water-side heat transfer coefficient varies based on the calculation method (constant Nu, functional Wilson, or two-coefficient Wilson plot method) and the correlation used (in the two-coefficient Wilson plot method).

The air-side heat transfer coefficients resulting from the functional Wilson plot, two-coefficient Wilson plot using the Peng and Peterson correlation, and from assuming a constant water-side Nu = 7.54 are shown in Figure 112.

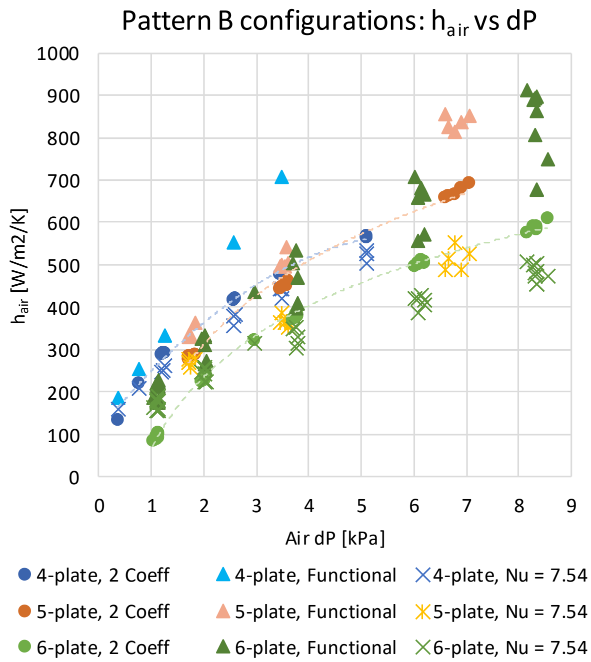

Figure 112. Air-side heat transfer coefficients vs air dP for TFAC-3E-3-5 (Pattern B) calculated using the two-coefficient Wilson plot method, functional Wilson plot method, and constant water-side Nu assumption.